Photocathodes for high brightness, high average current photoelectron injectors

DISSERTATION

zur Erlangung des akademischen Grades
doctor rerum naturalium (Dr. rer. nat.)

im Fach: Physik
Spezialisierung: Experimentalphysik

eingereicht an der
Mathematisch-Naturwissenschaftlichen Fakultät
der Humboldt-Universität zu Berlin

von

Martin Schmeißer

Präsidentin der Humboldt-Universität zu Berlin:
Prof. Dr.-Ing. Dr. Sabine Kunst

Dekan der Mathematisch-Naturwissenschaftlichen Fakultät:
Prof. Dr. Elmar Kulke

Gutachter:

1. Prof. Dr. Andreas Jankowiak
2. Prof. Dr. Simone Raoux
3. Prof. Dr. Kurt Aulenbacher

Tag der mündlichen Prüfung: 26.08.2019

Abstract

For many disciplines in basic and applied research, medicine and industrial development accelerators are an important driving force. Especially electron accelerators as synchrotron sources are among the brightest sources of radiation from the infrared to the X-ray regime and thus fundamental to a broad range of analytical techniques. Photoinjectors as electron sources for accelerator applications are a key component for the development of light sources such as free electron lasers as well as new accelerator concepts like energy-recovery linacs (ERLs). The photocathode and drive laser define the quantum efficiency and intrinsic emittance of the photoemission process and thus central figures of merit of the photoinjector.

This work focuses on the development of alkali antimonide photocathodes for the application in a superconducting radio frequency photoinjector. Alkali antimonides generally exhibit a high quantum efficiency and cesium potassium antimonide (Cs-K-Sb) specifically is expected to release electrons with a low intrinsic emittance as the photoemission threshold is close to the photon energy of common, green, drive laser wavelengths.

A preparation and analysis system has been commissioned for the deposition of Cs-K-Sb thin film photocathodes and their analysis regarding quantum efficiency and chemical composition. A new deposition technique, the alkali metal co-deposition, was established and compared to the sequential deposition in terms of process reliability and quality of the produced samples. For our setup, the co-evaporation procedure was found to yield samples with higher QE in a reproducible manner. The correlation of quantum efficiency with the stoichiometry as determined by X-ray photoemission spectroscopy was investigated and the Cs_2KSb composition yields higher QE than CsK_2Sb. In view of the operation of photocathodes in the cryogenic environment of the photoinjector, the influence of cooling on the spectral response was measured and no strong influence at the relevant photon energies was found. The intrinsic emittance of a cesium antimonide (Cs-Sb) photocathode was measured in a static accelerating setup and is discussed with reference to recent photoemission models. The expected decrease of the intrinsic emittance with photon energy was observed and a lower limit of the mean transverse energy manifests at the photoemission threshold.

The work concludes with a report of the commissioning of a prototype of the photoinjector and successful cathode transfers in ultra-high vacuum, which represents an important technological advancement towards the operation of an accelerator with the combination of Cs-K-Sb photocathodes and an SRF injector. This combination makes the generation of an electron beam with low emittance and high average current possible which is necessary, e.g. for the operation of an ERL like bERLinPro.

Zusammenfassung

Für viele Anwendungen in der Grundlagenforschung, Medizin und industriellen Entwicklung sind Beschleuniger der entscheidende Antrieb. Vor allem Elektronenbeschleuniger sind als Synchrotronquellen unter den brillantesten Quellen für Strahlung im Infrarot- bis Röntgenbereich und damit unerlässlich für eine Vielzahl von Anwendungen und analytischen Methoden. Photoinjektoren stellen als Elektronenquellen für Beschleuniger eine wichtige Komponente für die Entwicklung von Lichtquellen wie Freie-Elektronen-Laser, sowie für neue Beschleunigerkonzepte wie Linearbeschleuniger mit Energierückgewinnung dar. Die Photokathode und der Anregungslaser definieren dabei mit der Quantenausbeute und der intrinsischen Emittanz zentrale Kenngrößen des Photoinjektors.

Diese Arbeit beschreibt die Entwicklung von Alkali-Antimonid Photokathoden für die Anwendung in einem Photoinjektor mit supraleitendem Hochfrequenz-Resonator. Alkali Antimonide zeigen generell eine hohe Quantenausbeute und Cäsium Kalium Antimonid (Cs-K-Sb) im speziellen verspricht eine geringe intrinsische Emittanz aufgrund der Ionisierungsenergie, die nur knapp unter der Photonenenergie der grünen Anregungslaser liegt.

Mit der Inbetriebnahme eines Präparations- und Analysesystems konnte die Abscheidung dünner Schichten von Cs-K-Sb sowie die Messung der Quantenausbeute und chemischen Zusammensetzung erzielt werden. Dabei wurde mit der Ko-evaporation der Alkalimetalle eine neue Wachstumsmethode etabliert und hinsichtlich der Prozessstabilität und Qualität der erzeugten Proben mit der sequenziellen Methode verglichen. In unserer Anlage erzeugt der neue Prozess zuverlässig Proben mit höherer Quantenausbeute. Die chemische Zusammensetzung der Proben wurde mittels Röntgen-Photoemissions-Spektroskopie bestimmt und die Korrelation zur Quantenausbeute bestimmt. Dabei zeigt die Stöchiometrie Cs_2KSb eine höhere QE als CsK_2Sb. Mit Hinblick auf den Einsatz der Photokathoden in der kryogenen Umgebung des Photoinjektors wurde auch der Einfluss kalter Temperaturen auf die QE bestimmt. Es wurde kein starker Einfluss der Temperatur auf die QE bei den vorgesehenen Wellenlängen gefunden. Außerdem wurde die intrinsische Emittanz einer Cäsium Antimonid (Cs-Sb) Photokathode in einem statischen Beschleuniger gemessen und mit entsprechenden Modellen verglichen. Die erwartete Verringerung der intrinsischen Emittanz mit der Anregungsenergie wurde beobachtet, dabei zeigt sich eine untere Grenze an der Schwelle zur Photoemission.

Schließlich beschreiben die Inbetriebnahme eines Prototyps des Photoinjektors und erste erfolgreiche Kathodentransfers im Ultrahochvakuum einen wichtigen Schritt hin zum Betrieb eines Beschleunigers mit einer (Cs-K-Sb) Photokathode im supraleitenden Hochfrequenz-Injektor. Diese Kombination erlaubt die Erzeugung eines Elektronenstrahls mit niedriger Emittanz und hohem mittleren Strom wie es z.B. für den Betrieb eines Linearbeschleunigers mit Energierückgewinnung wie bERLinPro notwendig ist.

Contents

1. Motivation

Electron beams are useful to probe the structure, dynamics, and properties of materials. For decades, either the beam itself or emitted synchrotron radiation has been used to gain insight into the scientific problem at hand. Photoinjectors use the photoelectric effect to liberate electrons from a solid material, the photocathode, and accelerate the electrons in a strong electric field to relativistic energies. The immense progress in electron photoinjectors of the past few decades [1, 2] has enabled a range of new accelerator concepts like X-ray free electron lasers (XFELs, [3, 4]) and energy recovery linacs (ERLs) as well as unique experiments from ultrafast electron scattering [5] to wakefield accelerators [6]. These applications have the common request of a high brightness of the electron beam, which is defined as the electron current density per phase space volume occupied. In simple terms, considering a synchrotron source, higher charge density can lead to higher photon flux while the phase space volume defines the source spot and pulse length of emitted radiation. Thus, light sources also define their photon beam quality in a quantity called photon beam brightness, which is defined as photon flux per area source spot, opening angle and bandwidth. Likewise a high density of electrons can increase the signal one obtains, while a lower trace space volume improves the resolution of, e.g., a scattering experiment.

The development of future light sources and electron accelerators for high energy physics depends on electron sources that deliver high average currents with extremely high brightness. For example, ERLs require continuous wave (cw) operation at high average currents, and possible upgrades of cw FELs for the X-ray regime could be operated at a moderate average current but call for extremely low emittance. Among the sources for high brightness electron beams are cold field emitter tips [7], laser cooled atomic sources [8] and photoinjectors, but only photoinjectors combine high brightness and high average current. The properties of the electron distribution emitted from a photoinjector depend on the cathode material, the exciting wavelength and pulse distribution, as well as external factors like the applied electric field. In radio-frequency (RF) photoinjectors the accelerating field is the electric component of a standing RF wave that is confined in the boundary conditions of a metallic cavity. Especially when the cavity walls are superconducting (SRF), the combination of high electric fields of 20 - 30 MV/m with the possibility of cw operation at high repetition rates presents a unique parameter combination that includes excellent vacuum conditions due to the cryogenic environment and reduced ion-backstreaming when compared to a static (DC) accelerating gap.

Photocathodes are often discussed in terms of their respective figures of merit: quantum efficiency, intrinsic emittance and lifetime. The quantum efficiency (QE) is the unitless fraction of liberated electrons per incident photon. The intrinsic emittance, like the QE, depends on the excitation wavelength and quantifies the emittance contribution due to the initial kinetic energy distribution of the emitted electrons. The lifetime is usually given as the time constant of an exponential decay observed in the QE over time. The actual operational lifetime depends then on the specification of minimal QE required to operate the photoinjector. Often, it is also reported that the QE settles at a certain, lower level after the initial exponential reduction.

The average current in photoinjectors is limited, among other factors, by the QE of the photocathode. Typical values for metals are several orders of magnitude lower than the values obtained for semiconducting cathodes which implies that a drive laser with high average power at an ultraviolet (UV) wavelength is required. Especially for short pulse operation, the peak power of the laser pulse required at the cathode becomes close to the damage threshold of the optical elements in the laser path and the cathode surface. A photocathode with high QE at visible wavelengths mitigates these limitations in several ways. With QEs above 1%, the required photon flux is reduced by several orders of magnitude. Further, since drive lasers are typically higher harmonics of infrared Nd or Yb lasers, the conversion efficiency is much higher towards the second harmonic (green, 532 or 515 nm) in one frequency-doubling crystal than towards the fourth harmonic in two conversion elements. The peak laser power per area on the photocathode is reduced, thus allowing more freedom in the manipulation of the transverse laser profile without risking damage or local overheating of the surface.

At the same time, a typical tradeoff between QE and intrinsic emittance results from the increase in electron thermal energy with rising photon energy. A higher QE can thus be attained when a shorter excitation wavelength is used, but at the price of increased intrinsic emittance. Photocathodes with a high nominal QE can thus be employed to gain some headroom in the design of the photoinjector. For example, a Cs-K-Sb photocathode can be operated at 515 nm where the QE can be up to 10% and the intrinsic emittance is comparable to the one obtained from current metal cathodes. When ultra-cold electron beams are required, e.g. for diffraction experiments, the intrinsic emittance can be reduced by shifting the excitation wavelength towards the emission threshold. Low values of 20 meV for the mean transverse energy have been measured while the, albeit reduced, QE is still comparable to the nominal QE of metal cathodes.

The application of such cathodes presents challenges, however. Most prominently, the high reactivity of the alkali metals and the sensitivity of surface properties like the work function and emission barrier height to surface adsorption requires that preparation, transfer, and operation take place in pure vacuum environments of 10^{-10} mbar or lower total pressure. The lifetime of the cathode sample is otherwise reduced drastically. Furthermore, the lifetime depends on the purity of the cathode material and

substrate, as well as on operation conditions such as temperature, the suppression of back-streaming of ions and the composition of residual gas molecules. Compatibility with the high gradients in DC, and, especially, SRF photoinjectors require that the cathode is grown on a specialized substrate which can be cooled during operation and must be polished and cleaned to be free of field-emitting protrusions or particles.

This work focuses on the development of the Cs-K-Sb photocathode material as an electron source for SRF photoinjectors in the context of the bERLinPro energy recovery linac [9]. A dedicated preparation and analysis system was designed and commissioned and served as the experimental platform for the optimization of the deposition procedure for the photocathode samples. Within the scope of this work, an alkali metal co-evaporation procedure was developed and qualified. Methods for the chemical analysis and assessment of the performance of photocathode samples needed to be developed, as such, an X-Ray photoemission spectroscopy system was commissioned and calibrated which now serves to analyze the purity of substrates and deposited materials as well as the stoichiometry by quantitaive analysis. The data obtained from such measurements can be correlated to the QE and spectral response by means of an optical setup that is used to quantify the temperature and wavelength dependence of the QE. Such measurements are sidelined by a study of the intrinsic emittance of a similar photocathode material Cs-Sb. The engineering challenges imposed by the stringent purity requirements in terms of vacuum residual gas and particulates are covered throughout the chapters.

Following this introduction, the theoretical background involved in the discussion of photocathodes and SRF photoinjectors for high-brightness beams is covered in chapter 2 and in chapter 3 the methods are introduced which were employed to prepare and characterize the photocathode samples. The remainder of this thesis is organized as follows. In chapter 4 the preparation of Cs-K-Sb photocathodes is discussed, both by the sequential and alkali co-evaporation schemes. Chapter 5 addresses the comparison of the two deposition procedures in terms of stoichiometry of the samples and the temperature dependency of the spectral response. The measurement of the intrinsic emittance is covered in chapter 6. The results from commissioning of an SRF photoinjector with an exchangeable cathode interface are presented in chapter 7, before, the presented work is summarized in chapter 8.

The sections 5.1 and 5.3 have been published previously in [10].

2. High Brightness Electron Beams

Common to the applications of photoinjectors mentioned in the previous chapter is that they exhibit a high brightness of the electron beam produced. Brightness is defined as charge per spatial and temporal extensions of a portion (bunch) of the beam. Intuitively, the term beam brightness triggers the analogy to a light bulb. When connected to mains voltage, one may say it is "bright" enough to light a room. When the power of the bulb is reduced, one may say it is "too dim" or has not enough brightness. The light bulb is a tool to probe (by photons) and sense (see) the environment. Similarly the scientific definition of beam brightness B for photon and electron beams gives a measure of how effective the beam is to probe a sample or to interact with fields or targets. During a measurement, the signal will be increased when the number of electrons that participate is higher. Thus, brightness increases linearly with the charge or number of electrons, $B \propto Q$. Because measurements often require spatial selectivity, divide the charge by the area of the source point (in the same analogy, a halogen lamp is brighter than a fluorescent tube because it has a smaller emission area at similar photon output), $B \propto Q/\sigma_x\sigma_y$, where $\sigma_{x,y}$ are the r.m.s. dimensions of the source in the two planes transverse to the propagation direction. Similar to light rays, the ability to focus electron beams depends on the product of size and divergence of the source, $B \propto Q/\sigma_x\sigma_y\sigma_{x'}\sigma_{y'}$. Finally, one will be interested in what amount of time the charge passes, thus the brightness is divided by the bunch length and energy spread (longitudinal extensions) of a portion (bunch) of the beam.

For electron beams, the 6 dimensional brightness is thus defined as the beam current I divided by the r.m.s. size it occupies in the six-dimensional phase space [11]:

$$B = \frac{I}{\sigma_x\sigma_y\sigma_{x'}\sigma_{y'}\sigma_\gamma}. \tag{2.1}$$

where σ_γ is the energy spread.

A high peak brightness is required for applications where the electron beam generates light for pulsed, time-resolved experiments, such as X-ray diffraction at an FEL. In this case, the peak current can be increased by generating a high bunch charge or compressing the bunch length and a figure for comparison would be the 5D brightness as defined above, where the common definition of the peak current I_{peak} is bunch charge per rms bunch length

$$I_{\mathrm{peak}} = \frac{Q_{\mathrm{bunch}}}{\beta c \sigma_z} \,. \tag{2.2}$$

Applications that request a high average brightness integrate over a high number of pulses. The average brightness is maximum when the accelerator can be operated at high repetition rates and a high duty cycle. Ideally, quasi-cw operation is desired, where every bucket of the RF period is filled. Here, one may define the average brightness by using

$$I_{\mathrm{avg}} = f\, t\, Q_{\mathrm{bunch}} \tag{2.3}$$

where f is the repetition rate of the injector and t is the duty cycle ($t = 1$ for c.w. operation). At the same time, the average current is also limited by the available QE of the photocathode and drive laser power

$$I = QE * P_{\mathrm{laser}}/h\nu \,. \tag{2.4}$$

A limit to the achievable brightness can be derived from the condition that photoemission ceases when the electric field of the extracted charge equals the external accelerating field [12]. For the case of short bunches, which can be approximated as a thin, extended disk the maximum brightness is

$$B_{\mathrm{n,4D}} = \frac{m_0 c^2 \epsilon_0 E_{\mathrm{cath}}}{2\pi \ \mathrm{MTE}} \,. \tag{2.5}$$

where $m_0 c^2$ is the rest energy of an electron, ϵ_0 is the dielectric constant, and E_{cath} is the electric field present at the cathode surface. The mean transverse energy (MTE) here connects characteristics of the photoemission process and cathode material directly to the beam emittance and is thus of considerable interest in the discussion of photocathodes and photoinjectors.

As the full 6D characterization of the charge density distribution is not accessible by an experiment, it is common to consider the two-dimensional projections of the phase space into, e.g., the $x - x'$, $y - y'$ or the $t - \Delta E$ plane.

In each plane the area occupied by the particle distribution is defined in a statistical sense as the second moment of the distribution of particles in the u, u' plane:

$$\varepsilon_{\mathrm{g,u}} = \sqrt{< u^2 >< u'^2 > - < u\, u' >^2} \tag{2.6}$$

this definition is robust in that it captures the deterioration due to effects like filamentation and it lends to numerical evaluation in particle tracking codes or photoemission

models. The subscript g denotes the geometric emittance in contrast to the normalized emittance $\varepsilon_{\mathrm{n,u}}$ which is constant during acceleration and scaled by the relativistic factors $\beta\gamma$

$$\varepsilon_{\mathrm{n,u}} = \beta\gamma\varepsilon_{\mathrm{g,u}}\,. \tag{2.7}$$

The two-dimensional emittance as defined here is conserved during beam propagation only if no off-diagonal blocks are present in the transport matrices of the beam-line elements. Truly conserved under action of conservative forces as stated in Liouville's theorem is only the six-dimensional emittance, a fact that is readily used in emittance-exchange schemes where compression in one plane can be achieved at the cost of expansion in another.

For the discussion of photocathode physics, it is common to consider the normalized intrinsic emittance in terms of emitting spot size and momentum of the electrons as

$$\varepsilon_{\mathrm{n,u}} = \sigma_{\mathrm{u}}\frac{\sqrt{\langle p_{\mathrm{u}}^2\rangle}}{m_{\mathrm{e}}c} = \sigma_{\mathrm{u}}\sqrt{\frac{MTE}{m_{\mathrm{e}}c^2}}. \tag{2.8}$$

Close to the surface one may assume zero correlation between position and momentum. Here σ_{u} is the emission spot size (i.e. rms laser spot size), $\langle p_{\mathrm{u}}^2\rangle$ is the variance of the transverse momentum. Additionally, assuming isotropic emission, the mean transverse energy is the sum of the two transverse components, thus

$$MTE = \langle E_{\mathrm{x}}\rangle + \langle E_{\mathrm{y}}\rangle \tag{2.9}$$

$$MTE = 2\langle E_{\mathrm{x}}\rangle = \frac{\langle p_{\mathrm{x}}^2\rangle}{m}\,. \tag{2.10}$$

The following section provides a review of the current photoemission models that can be used to predict the figures of QE and MTE which are relevant to the design and operation of electron accelerators.

The Three-Step Model of Photoemission

Spicer's three step model (modified Fowler-DuBridge) was first proposed in [13] for the discussion of photoemission from alkali antimonides. The central assumption is that the photoemission process can be treated as three independent steps

1. Excitation: Incident light of energy hν excites an electron from the initial state to an excited state.

2. Transport: The excited electron moves through the crystal towards the surface. Different levels of sophistication have been applied to the treatment of scattering effects during that process.

3. Emission: Electrons close to the surface may escape. The condition that the momentum component normal to the surface must be high enough to overcome the surface barrier leads to a critical angle of the momentum vector of the excited electron.

The initial model by Spicer assumes parabolic shapes for both the valence and conduction band, as illustrated in Fig. 2.1a. Further, the model uses two components of the light absorption $\alpha_T = \alpha_c + \alpha_p$, where α is the absorption coefficient, α_p refers to the absorption that leads to excitation above the vacuum level, and α_c relates to unproductive absorption into states below the vacuum level.

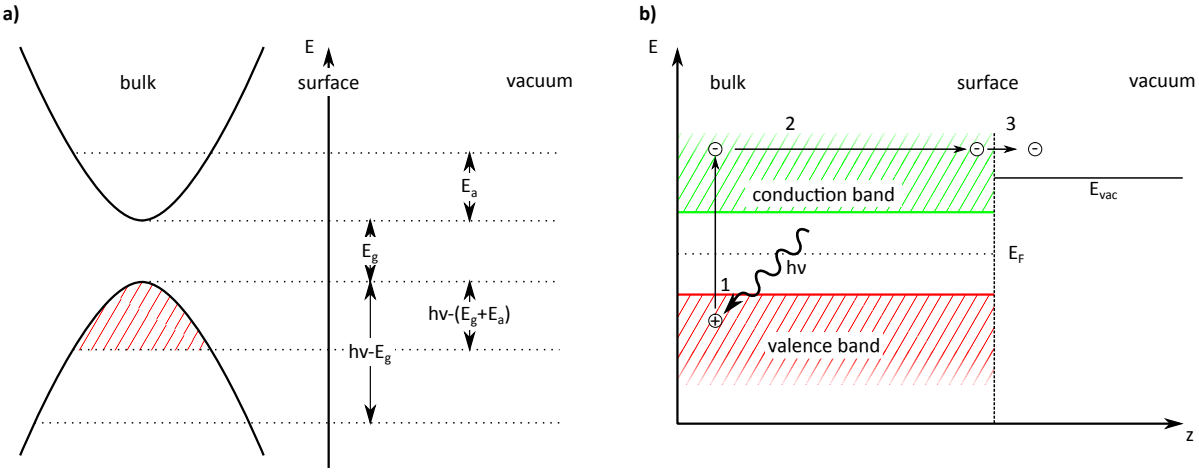

Figure 2.1.: (a) Energy levels assumed in Spicer's 1958 treatment of the three-step-model. The states that contribute to photoemission are patterned. [13] (b) Illustration of the three processes. 1 - Excitation, 2 - Transport, 3 - Emission [14].

The original work assumes a step function for the transmission probability at the surface potential (Richardson approximation) and leads to a semi-empirical relation that

$$QE = A(h\nu - E_G - E_A) \tag{2.11}$$

where E_G is the band gap and E_A is the electron affinity. Note that for metals, the threshold photon energy above which photoemission occurs is equal to the work function $\phi = E_{vac} - E_F$. For semiconductors, however, while the work function retains the same definition, no photoemission occurs when $h\nu = \phi$ as there are no states that could be occupied at E_F. The photoemission threshold occurs at $h\nu = E_G + E_A$. Refer to Fig. 2.2 for an illustration of the energy levels. The form of equation 2.11 is especially suited for fitting to experimental data close to the threshold and widely employed for the extraction of values for $(E_G + E_A)$ but it often fails to reproduce the form of the spectral response over a range wider than 1 eV.

Note that empirically eq. 2.11 often yields a good representation of the QE for values of $h\nu > E_G + E_A + 0.5\,\text{eV}$ but close to the threshold the curve can be approximated with higher accuracy by the quadratic form

$$QE = A(h\nu - E_G - E_A)^2 \,. \tag{2.12}$$

Compared to the simple empirical forms presented above, for metallic emitters and disordered (i.e. polycristalline or no ordered surface) semiconductors the model proposed by Spicer and Herrera-Gómez [15] is more successful in reproducing the experimental data. A complete review of the model can be found in [14]. In the excitation step, the model takes into account the ratio of electrons excited over the vacuum level (α_{PE}) versus all excited electrons (α) which is in the simplest case the fraction of the energy differences. A strong influence on the QE can be shown for the ratio of optical absorption length l_a over the mean free path, or scattering length, L of the excited electrons. The optical absorption length governs at which depth into the surface electrons are excited through Beer-Lambert's law. Likewise, the probability of emission depends strongly on the distance an electron has to overcome before reaching the surface. In metals, due to strong electron-electron scattering, an excited electron may quickly loose the energy required to overcome the surface barrier before reaching it.

Follow the derivation provided in [14] to arrive at the expression for QE

$$QE(h\nu) = (1 - R)\frac{\frac{\alpha_{PE}}{\alpha}P_{dir}}{1 + \frac{l_a}{L}} \,. \tag{2.13}$$

where α_{PE}, α, l_a, and L are as defined above, R is the optical reflectivity, and P_{dir} is the probability that the momentum vector of an electron after excitation points towards the surface, that is, has a component normal to the surface that is large enough to overcome the surface barrier.

The ratio α_{PE}/α is the ratio of electrons that get excited above the vacuum level. Clearly, it rises with the excitation energy $\hbar\omega$ and with lower electron affinity. Materials that

exhibit a high QE have a α_{PE}/α value between 0.1 and 1.0 where emitters with negative electron affinity may have values close to 1.0.

In the denominator, the ratio of absorption length to scattering length, l_a/L, defines the spatial region, from which photoexcited electrons may contribute to the yield. The optical absorption length at photon energies where photoemission takes place is in the range of a few 100 Å. For metals, the electron scattering length can be as low as 10 Å due to pronounced electron-electron scattering. It is approximately 40 Å for copper when $h\nu$ is 1 eV above the threshold [15]. Considering equation 2.13, this means that the quantum yield for copper is reduced by about one order of magnitude by scattering of excited electrons.

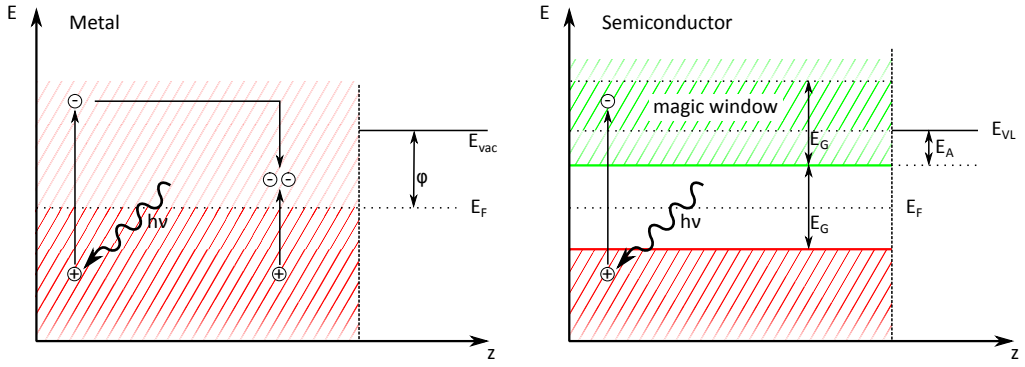

Figure 2.2.: Electron-electron scattering in metals and semiconductors. Scattering into unproductive states in metals allows electrons to loose the energy needed to escape while in semiconductors a "magic window" can be present where electrons cannot scatter into the band gap but have enough energy to escape.

In semiconductors electron-electron scattering is suppressed in a "magic" energy window E_{MW} above the vacuum level where $E_{VL} < E_{MW} < E_{VBM} + 2E_G$ if the electron affinity is less than the band gap (thus, $E_{VL} < E_{VBM} + 2E_G$). This is because there are no final states in the band gap available and the energy of the electrons is too low to raise a scattering partner from the valence band to the conduction band. The various energy levels are illustrated in Fig. 2.2. In efficient emitters, the scattering length of electrons with energy just above the vacuum level can be in the order of the optical absorption length, so the fraction $\frac{l_a}{L}$ is close to unity.

The direction of the momentum vector of the excited electron plays an important role when electron-electron scattering is pronounced. Because a single scattering event will reduce the energy of an excited electron below the vacuum level only those electrons that reach the surface without scattering can be considered for emission. Thus, a narrow escape cone is defined by the maximum angle ϑ_{max} between the electron's momentum vector and the surface normal that will allow the electron to escape. Assuming clean and even surfaces, ϑ_{max} is defined by the conservation law

of transverse momentum p_x at the crystal-vacuum interface and the requirement, that the longitudinal component p_z be larger than the surface barrier. The evaluation of this requirement in [16] allows to express the QE for metals in terms of the energy levels as

$$QE_{\text{metal}} = \frac{1 - R(\nu)}{1 + \frac{l_a}{L}} \frac{E_F + h\nu}{2h\nu} \left[1 - \sqrt{\frac{E_F + \phi}{E_F + h\nu}}\right]^2 \tag{2.14}$$

In contrast, due to the supression of electron-electron scattering in the magic window of a semiconducting cathode, electron-phonon scattering may dramatically increase P_{dir}. Consider electron-phonon scattering as a random-walk process with a sink at the crystal surface [15]. The scattering process is nearly elastic, so the direction of the electron is randomized but it looses only a small fraction of its energy. Several scattering events are possible before an electron looses too much energy to overcome the surface barrier and in materials with low or negative effective electron affinity all excited electrons will eventually escape. Thus, P_{dir} may be approximated by a step function for efficient semiconducting emitters. In that case, the QE should be written as

$$QE_{\text{semi}} = \frac{1 - R(\nu)}{1 + \frac{l_a}{L}} \frac{h\nu - E_G - E_A}{h\nu} \,. \tag{2.15}$$

Intrinsic Emittance

Both the Fowler-DuBridge theory and the three-step-model are inherently one dimensional in the direction normal to the surface and thus cannot be used to derive an expression for the intrinsic emittance or brightness of the cathode. One often applied model for the emittance is mostly independent of the emission process [17, 18] and posits that the emitted electrons have an isotropic momentum distribution and their kinetic energy in vacuum distributed uniformly between $E \in (0, h\nu - E_G - E_A]$. The mean transverse energy is the average value of the two transverse components where $< E_x > = < E_y > = < E_z >$. Thus, the mean transverse energy MTE and intrinsic emittance become

$$< E > = \frac{1}{2}(h\nu - E_G - E_A) \tag{2.16}$$

$$\text{MTE} = \frac{2}{3} < E > = \frac{1}{3}(h\nu - E_G - E_A) \tag{2.17}$$

$$= \frac{1}{3}(h\nu - E_{\text{exc}}) \tag{2.18}$$

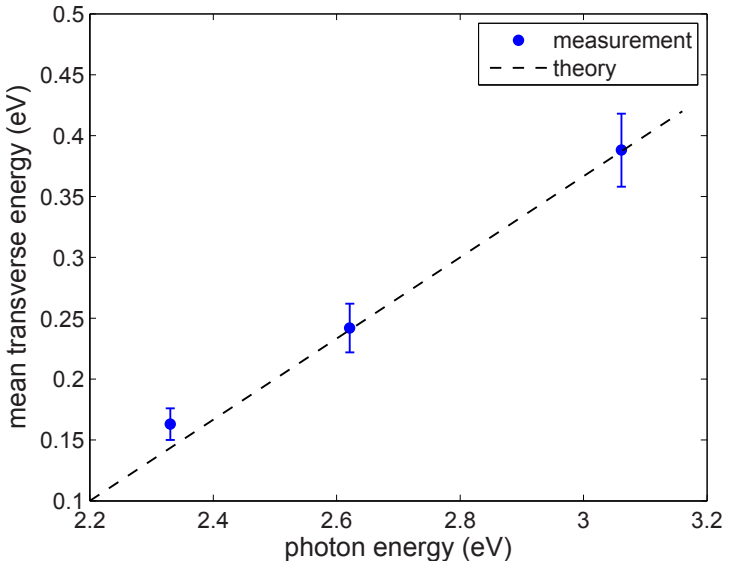

Figure 2.3.: Mean transverse energy of the Cs_2KSb photocathode measured at different excitation energies. The MTE rises as predicted by equation 2.18. Reprinted from [18], with permission.

Here, $E_{exc} = E_G - E_A$ is the excess energy, that excited electrons receive over the photoemission threshold. This model has been shown to correctly describe one set of measured data of intrinsic emittance measured from a Cs_2KSb cathode, as shown in Fig. 2.3.

The MTE measurements presented in Chapter 6 and the values presented in Fig. 2.4 show a rise of MTE with the excess energy at a slope similar to the prediction of 2.18, but the model does not capture the plateau that is observed near the photoemission threshold.

The virtue of the three step model, however, is that it may be extended to include more details of the photoemission process and electronic structure of the cathode than it would be the case in Fowler-DuBridge theory. An ambiguity arises at this point as the term three-step-model is used both for the model developed by Spicer as well as to discriminate a general way of treating the photoemission process in three steps as opposed to a quantum-mechanical one-step model.

The theoretical description of the photoemission process, and the dependence of the resulting beam parameters on materials properties and operation parameters like excitation wavelength and temperature is an active field of research. For the description of emission from semiconductor photocathodes, models of varying detail have been proposed, and the most successful ones in the description of QE and intrinsic emittance are numeric (Monte-Carlo) time-propagation of an electron ensemble through the three steps of excitation, transport, and emission [19–21]. Typically, the excitation step is modeled by populating a reduced model of the valence band structure by

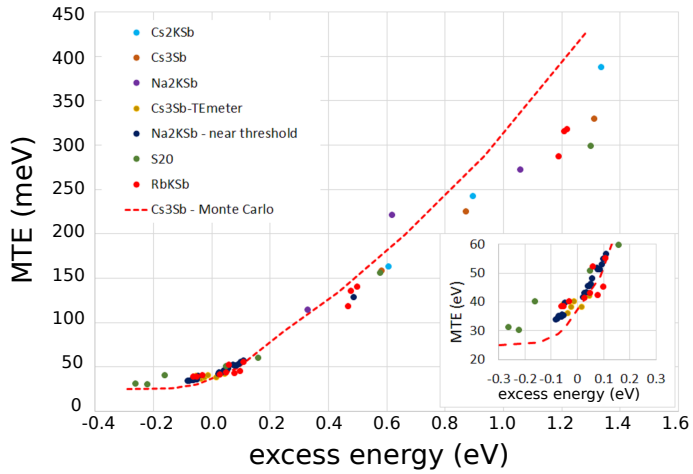

Figure 2.4.: MTE measurements of disordered materials for excess energies close to the photoemission threshold. Reprinted from [2], with permission. The MTE can be greatly reduced by excitation close to the threshold but a lower limit is imposed by the thermalization of scattered low-energy electrons.

a number of electrons, following the spatial exponential decay of the incident light inside the material. The transport and scattering step is treated in a semi-classical approach to solve the equations of motion according to the kinetic energies associated with the occupied wave-vectors of the electrons. Different mechanisms for scattering of the electrons with carriers, phonons and impurities are considered and evaluated in the Monte-Carlo integration. Such simulations allow the extraction of total yield, momentum distributions, and time delay by observing the electrons which leave the cathode, i.e. have sufficient longitudinal momentum when they impinge on the surface, while electrons with total energy less than the vacuum level, due to scattering, are removed from the simulation.

These treatments are not ab-initio and rely on a good description of the band structure and materials properties, which are well documented for the case of metals and GaAs, but not for CsTe or the alkali antimonides. Due to the heterogeneous nature and differing growth procedures, significant ambiguity is found in the relevant literature on the band gap, electron affinity, scattering lengths, effective electron mass and optical constants of these materials. A successful application thus relies on the selection of parameters present in literature from experiments [22] and electronic structure calculations [23–27].

2.1. Photocathode Materials

A variety of materials have been employed as electron sources in existing accelerators or are under development for future machines. In the following section a review is presented of successful applications of different materials and the performance of such cathodes is discussed in terms of the figures defined above: QE, intrinsic emittance and lifetime. One can categorize the current cathode materials into three groups: metals, semiconductors with positive electron affinity (PEA), and semiconductors with negative electron affinity. A few common materials are shown in Fig. 2.5 with measured QE values along parametrizations of equations 2.14 and 2.15. The experimental values are compiled from [13, 16, 28, 29] for Cs-K-Sb, Cs-Sb, CsTe and copper. Values for the optical constants, work functions, and scattering lengths have been obtained from [13, 16, 26, 30, 31]. For CsTe, no data was found to calculate Eq. 2.15 in the relevant energy range.

Metals have the advantage that high purity samples are readily available and can be polished to few nanometers of surface roughness. Once the surface has been prepared in vacuum to remove surface oxides and other contaminants, e.g. by laser cleaning or ion irradiation, the surface remains fairly unreactive and retains its QE over extended operation periods (months) even at vacuum pressures above 10^{-9} mbar. The drawbacks of metallic cathodes are clearly that photoionization is possible only with a UV laser and even 1 eV above the work function the QE is orders of magnitude lower when compared to semiconducting cathodes. Nevertheless, successful examples of use are the operation of the LCLS X-ray FEL with photoemission from copper cathodes [32], the runs of the ELBE radiation source with the first SRF photoinjector to drive a user facility, using laser-cleaned magnesium cathodes [33, 34], as well as the superconducting lead cathode used in the first photoinjector prototype for bERLinPro [35–37].

The group of semiconductors with positive electron affinity has received much attention lately as they hold the promise of drastically improving the performance of X-Ray FELs or enable high-average-current applications like ERLs [2, 17, 38]. CsTe is the only species of this group that has been used to drive user facilities [39–41], and while it exhibits a high QE and well defined emittance [42], still a UV drive laser of $h\nu > 4\,\mathrm{eV}$ is required. The lifetime of this material has been shown to be sufficient as it has been operated for many months in a normal-conducting RF gun at vacuum pressures around 10^{-9} mbar at the FLASH facility [40]. More flexibility in the emission parameters and a reduced burden on the drive laser by using visible light can be achieved with alkali antimonide photocathodes. These materials have the general stoichiometry M_3Sb where M can be one, or multiple elements from the alkali group, and they are well known for their very high QEs due to the application in television vacuum tubes and photomultipliers [43–47]. Their biggest advantage is certainly that high QEs > 10% can be achieved for common laser wavelengths of $\lambda/2 = 515$ or 532 nm. For applications that require control over the intrinsic emittance, one can

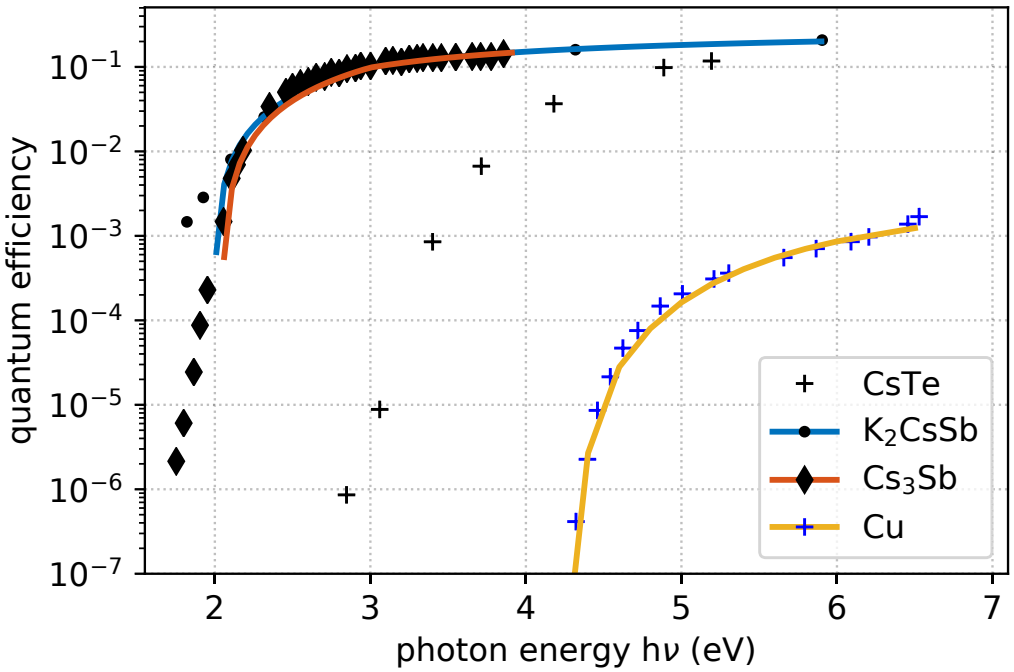

Figure 2.5.: The spectral response functions of common photocathode materials close to the threshold.

achieve near room-temperature MTEs while retaining a useful QE of 1% by operating 0.1 eV above the threshold.

While the highest QEs measured in such systems are recorded with the CsSb:NaKSb, or "S20", photocathode [47] the focus of this work is the application of the more systematically understood Cs-K-Sb system for photoinjector applications. As the work function and photoemission threshold of the alkali antimonide surfaces is often lower than 2.0 eV and these two quantities depend very sensitively on the adsorption of contaminants on the surface, the lifetime of the alkali antimonide photocathodes in terms of residual gas exposure is certainly lower than, e.g. a metal or CsTe cathode. However with the advent of non-evaporable getter (NEG) pumps with high pumping speed and the cryogenic environment in an SRF photoinjector it is expected that the total vacuum pressure during operation is well below 10^{-10} mbar and thus suitable to operate such cathodes. Still, the high reactivity necessitates a cathode exchange mechanism and UHV transport of such cathodes from the deposition system to the photoinjector.

One field of electron beam production is left to the last group which is a semiconducting photocathode with negative electron affinity. Here GaAs is the single material commonly employed. Its high band-gap requires that the surface is activated by a sub-monolayer coating of cesium and oxygen which forms a surface dipole layer and lowers the electron affinity to negative values, thus enabling emission with infrared excitation. However, the extreme sensitivity of the Cs-O layer makes these cathodes

hard to handle and the reduced lifetime prohibits use in applications that require high average current. Unique to GaAs is that it has the ability to produce polarized electron beams where one spin direction is emitted preferentially due to splitting of the spin degeneracy of the highest occupied band in strained lattice configurations.

In conclusion from this section, the strategy for the development of photocathodes for the bERLinPro photoinjector was set as follows. The ambitious goals of up to 100 mA average current production in continuous wave mode are only possible when a high QE of several percent is achieved at $\lambda/2 = 515$ or 532 nm which are the wavelengths of specially developed laser systems that generate picosecond long pulses at the full RF repetition rate and can be phase locked to the 1.3 GHz system of the accelerator. Currently, sufficient average power can be generated at the visible wavelengths but not in the UV due to the conversion efficiency of the frequency doubling crystals. From Fig. 2.5 it is evident that these requirements are met by the alkali antimonide photocathodes. Of this family, the Cs-K-Sb system was selected, as it seemed the most well studied among the possible candidates with respect to growth procedures, properties and electronic structure, contamination behavior, lifetime, and behavior in photoinjector environments. The goals are thus to develop and optimize a deposition procedure for such Cs-K-Sb cathodes that assures reproducibility on metallic substrates. The substrate design was developed to define processing steps and mechanical tolerances in order to employ copper or molybdenum plugs, which were chosen for their good thermal conductivity, that can be exchanged from the photocathode insert and to set up and commission the entire cathode transfer chain from the preparation system into the cavity.

The models discussed above predict that the intrinsic emittance obtained from Cs-K-Sb is dominated by the excitation photon energy at 515 nm and it will thus become a significant fraction of the emittance in the injector. It is therefore important to obtain smooth photocathode films with good uniformity of the work function in order to mitigate emittance dilution due to physical and chemical roughness.

2.2. Beam Properties in a Photoinjector

After the initial properties of an electron beam have been discussed in the previous section, consider now the evolution of an electron bunch as is propagates through the photoinjector. The electrons are accelerated by an electric field, either static as in DC guns or the electric component of a standing electromagnetic wave in an RF cavity.

An illustration of the electric an magnetic fields present in the case of an SRF photoinjector is shown in Fig. 2.6 together with their influences on the beam emittance. The evolution of bunch size and emittance together with the field profiles in the photoinjector is shown in Fig. 2.7

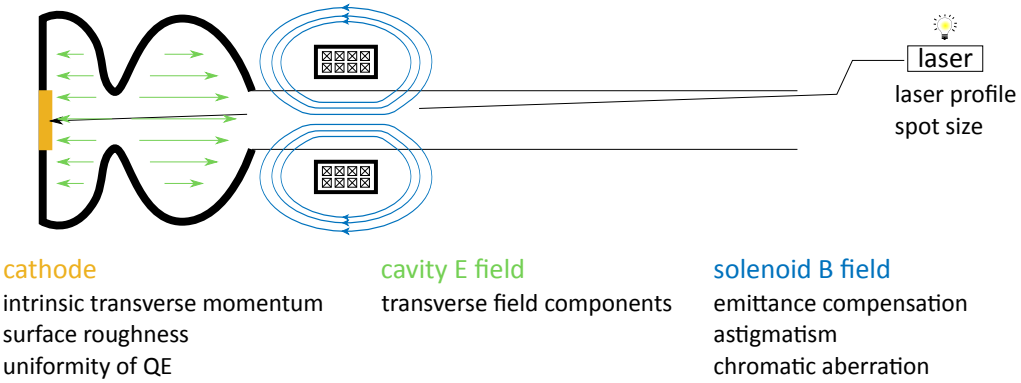

Figure 2.6.: Schematic illustration of an SRF photoinjector setup showing the components that contribute to the final beam properties.

Considering the beam emitted from an ideal photoemission cathode, the emittance is set by the intrinsic emittance of the photoemission process as discussed above, and scaling laws can be derived for the maximum achievable beam brightness at emission. Realizing that the electric field due to the extracted charge can approach the magnitude of the externally applied field and thus prevent further emission leads to the steady state condition in the well known Child-Langmuir law that describes the maximum current density j_{CL} obtained in an infinite parallel-plate diode of gap distance d and applied voltage V_0

$$j_{\mathrm{CL}} = \frac{4\epsilon_0}{9}\sqrt{\frac{2e}{m_{\mathrm{e}}}}\frac{V_0^{3/2}}{d^2}\,. \tag{2.19}$$

however, the emission radius in photoinjectors is typically small, i.e. ~1 mm, an thus far from the conditions assumed in the derivation of Child and Langmuir. In such cases one can obtain laws for the maximum brightness, which is again, limited by the charge density that can be extracted before emission ceases due to the counteracting space charge, in two cases of different beam aspect ratios. In the case of a short, "pancake" shaped bunch which expands much farther in the transverse directions than the longitudinal, the brightness is independent of the emission radius and bunch charge [12]

$$B_{\mathrm{max}} = \frac{mc^2\epsilon_0 E_{\mathrm{cath}}}{2\pi MTE}\,. \tag{2.20}$$

In comparison, an increase in brightness can be achieved in the case of long bunches with small transverse extensions (the "cigar" regime) by allowing longer bunch lengths, however at the expense of total extracted charge due to smaller emission spot sizes. In that case the maximum brightness scales as [48]

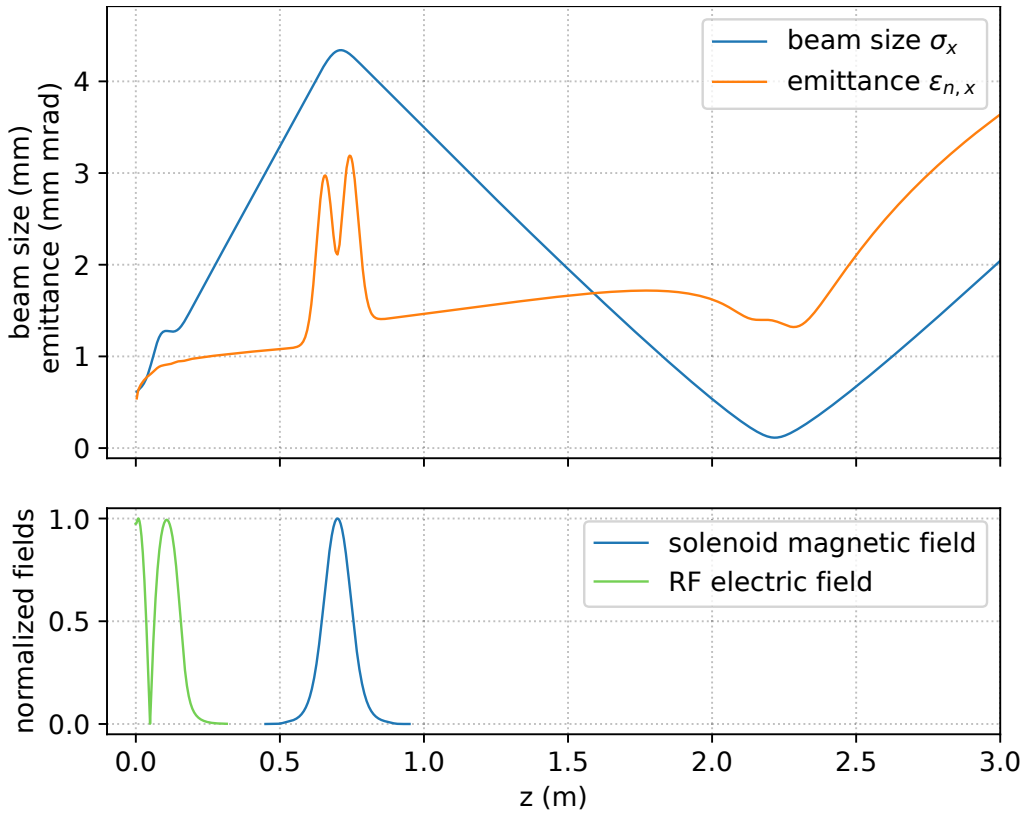

Figure 2.7.: Evolution of the properties of a bunch of 50 pC through the injector (top) as obtained from a tracking simulation in Astra. The normalized magnitudes of the electric RF and magnetic solenoid fields are indicated (bottom). The bunch size initially rises due to the intrinsic divergence and space charge forces, it reaches a maximum at the solenoid where it is focused to a waist location further downstream.

$$B_{\max} \propto \frac{E_{\text{cath}}^{3/2} \Delta t}{\sigma_{\text{r}} MTE} \ . \tag{2.21}$$

In the two definitions above, E_{cath} is the launch field, i.e. the electric field present at the cathode during emission; Δt is the time duration of the emission, σ_{r} is the transverse bunch radius, ϵ_0 is the vacuum dielectric constant, and mc^2 is the rest energy of an electron.

It is evident from Eq. 2.8 and Fig. 2.8 that the intrinsic emittance scales linearly with the emission spot size. The straightforward strategy to reduce the emittance would thus be to reduce the initial beam size (laser spot size) while keeping the bunch charge (laser pulse energy) constant. There is however a minimum spot size and thus minimal emittance that can be achieved before the increasing space charge

force dramatically increases the emittance with lower spot sizes. As the bunch travels through the injector it is subject to further linear and non-linear forces. The magnetic field of the solenoid introduces an emittance contribution $\varepsilon_{\mathrm{sol}}$ due to the chromatic and spherical aberrations inherent to the magnetic field distribution.

Details of the influence of the solenoid can be found in [49]. The magnitude of $\varepsilon_{\mathrm{sol}}$ depends strongly on the beam size at the position of the solenoid, which manifests as the strong increase of $\varepsilon_{\mathrm{sol}}$ between the two charges represented in Fig. 2.8.

Further contributions due to the effect of space-charge forces $\varepsilon_{\mathrm{SC}}$ and due to the RF field of the RF cavity $\varepsilon_{\mathrm{RF}}$ are also shown in Fig. 2.8. It becomes evident that the total projected emittance is dominated by the intrinsic emittance of the cathode and the RF contribution at large emission radii. When the emission radius is reduced, and assuming a constant bunch charge, the emittance becomes dominated by the space-charge effect. A certain spot size will thus minimize the projected emittance that can be achieved at a given bunch charge. As this radius is well below 1 mm for charges up to 100 pC and bunch lengths below 5 ps, the average intensity of the drive laser impinging on the cathode can be estimated.

In addition to the intrinsic emittance defined by the photoemission process, also the homogeneity of the QE and work function and the surface roughness will contribute to the emittance. Hot spots in the QE will locally increase space charge effects and areas of low efficiency will dilute the charge density [50, 51], and the surface roughness of the substrate and the active photocathode film impacts the homogeneity of the accelerating field [52, 53].

Throughout this work, the *intrinsic* emittance $\varepsilon_{\mathrm{intr}}$ is defined as the contribution due to the photoemission effect and depends solely on the emission spot size and the modeled energy distribution of the emitted electrons as defined in equation 2.8. In an experiment only the sum of the intrinsic emittance with the contributions due to non-homogeneity and surface roughness is accessible and is defined in this work as the *thermal* or *cathode* emittance $\varepsilon_{\mathrm{cath}}$

The emittance contributions shown in Fig. 2.8 are defined such that the total emittance can be obtained as the sum

$$\varepsilon_{\mathrm{n,tot}} = \sqrt{\varepsilon_{\mathrm{cath}}^2 + \varepsilon_{\mathrm{RF}}^2 + \varepsilon_{\mathrm{SC}}^2 + \varepsilon_{\mathrm{sol}}^2} \tag{2.22}$$

Note that the derivation of the scaling laws in Eq. 2.20 and 2.21 assumes space-charge limited emission and thus departs from the linear regime where the emitted current is defined by the QE as in $I = QE * P_{\mathrm{laser}}/h\nu$. A high QE is required to reach this regime while keeping the laser intensity at a feasible value, which is often defined by the cooling budget of the photocathode interface. For example, it has been shown that the local temperature increases by 100 K above the coolant temperature when a stainless steel substrate absorbs 1 W of laser power over the area of a 0.5 mm emission

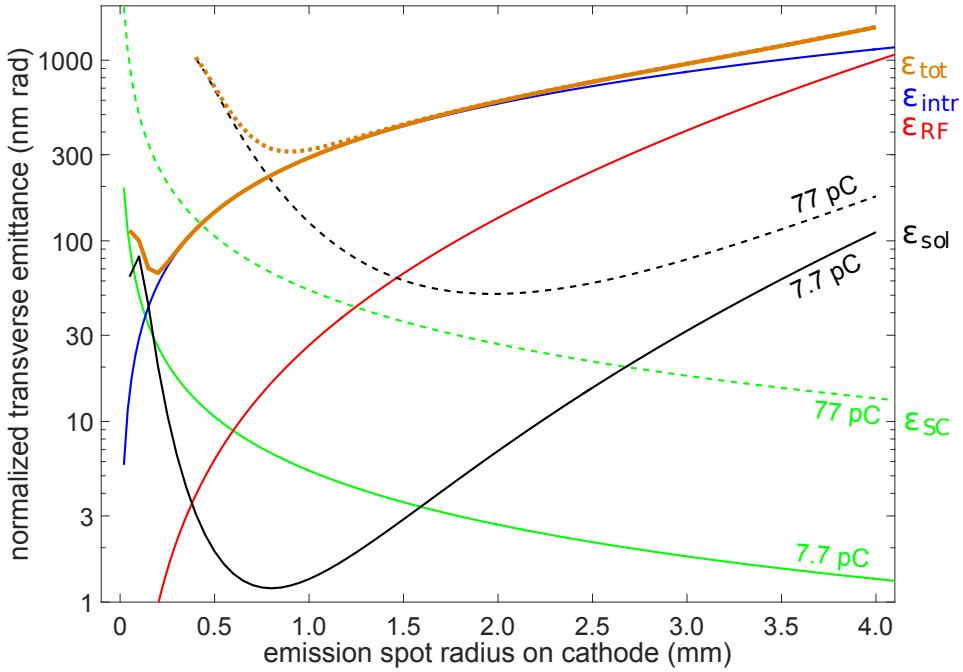

Figure 2.8.: The components of the projected emittance from an RF photoinjector. Two cases of 77 pC and 7.7 pC bunch charge are considered in the dashed and solid lines, respectively. Reprinted from [49]. The calculation assumes a constant gradient, laser pulse length and emission phase.

spot radius [54]. Clearly, high QE photocathodes are thus necessary to enable the emission from the optimized and small spot sizes at high average current.

3. Methods

Purposefully for the development, analysis, and systematic study of photocathode materials, as well as for the production of photocathodes for the bERLinPro photoinjector, the photocathode preparation and analysis system ("PAS") was designed and commissioned as a vacuum deposition chamber with an attached analysis chamber. The system has, by now, acquired its own history which started in 2012 when the core chamber was designed and purchased by Dr. Susanne Schubert. The original system allowed the deposition of Sb from PtSb beads and alkali metals from Alvatec sources, and it featured the X-ray source and electron analyzer which are discussed in section 3.3. As part of the groups collaboration with the team of John Smedley, the entire system was shipped to Brookhaven National Lab and it was one of the author's first tasks as a master student to take part in the comissioning of the system at BNL and grow the first cathodes in the system [14].

After it was returned to HZB in 2014, various amendments and additional analysis methods were set up and now make it a versatile system that allows both the development of the deposition process as well as production of cathodes for bERLinPro. The addition of a transfer system with load-locks for the introduction of new samples and transfer of samples to the vacuum suitcase connects the chamber to the photocathode transfer chain - the transfer mechanism is covered in chapter 7. Photographs of the PAS and transfer system are shown in Fig. 3.1.

This chapter covers the general setup of the vacuum systems, the generation of ultra-high vacuum, and the arrangement of the evaporation sources in the first part. In section 3.3, the characterization of photocathodes with respect to chemical composition and stoichiometry as well as purity of the substrates and deposited material via X-ray photoemission spectroscopy is covered. The primary performance parameters of the photocathodes, QE(λ, T) and MTE(λ, T) are addressed in the sections 3.2 and 3.4.

3.1. The Photocathode Preparation and Analysis System

The photocathode system consists of two main vacuum vessels, which are stacked horizontally and separated by a gate valve. Sample substrates are introduced via a load-lock and, once mounted on the sample stage, can be moved between the two

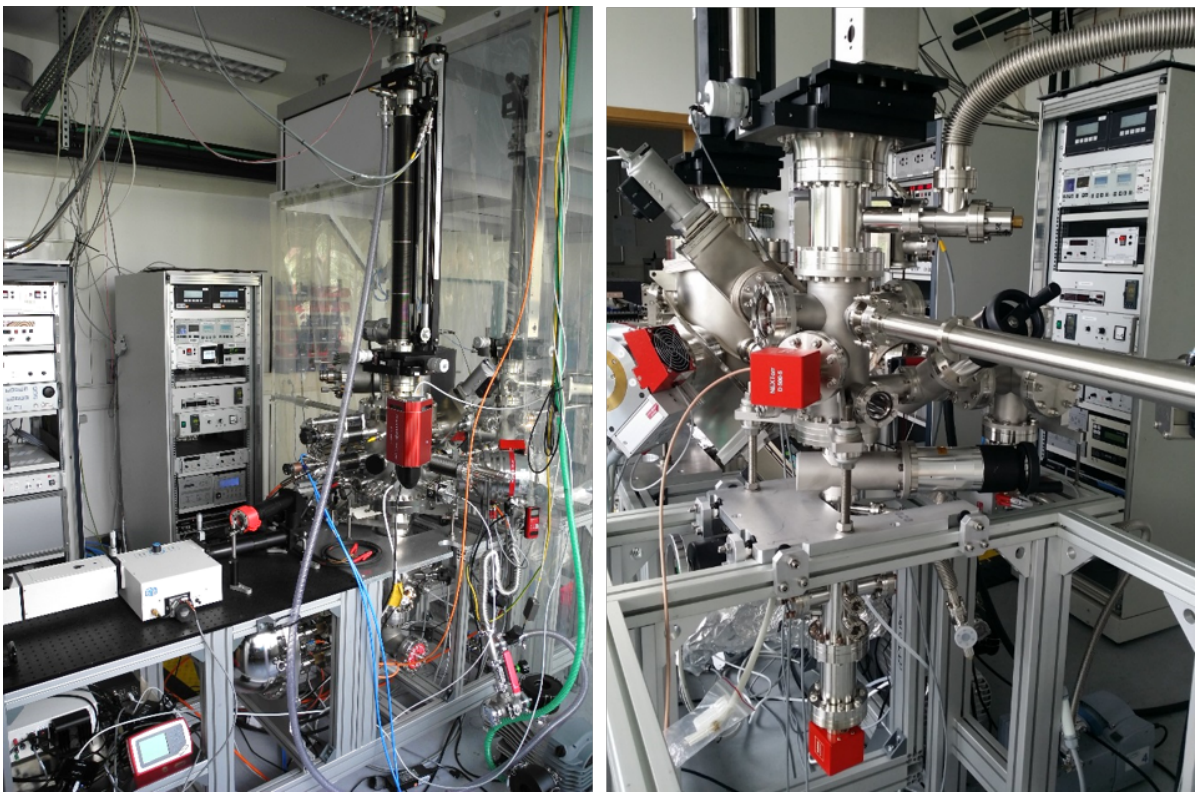

Figure 3.1.: View of the preparation and analysis system (left) and the transfer system (right) with load-lock in the cathode lab. Reprinted from [55].

chambers by extending the z shift of the manipulator through the opened gate valve. Positioning of the sample is possible in five degrees of freedom which are the cartesian axes x, y (horizontal), and z (vertical) as well as the rotation around the z-axis and the sample normal. By means of a radiative heater the sample can be heated up to 600°C and by conductive cooling through a copper braid that connects to a liquid nitrogen reservoir it can be cooled to -150°C.

Figure 3.2 shows the sample stage with a Mo plug substrate, alkali dispenser sources mounted on current feedthroughs and the Sb effusion cell facing a quartz crystal microbalance that can be retracted to give way for the sample stage. The aperture is mounted on isolating ceramic bushes and connected to a BNC feedthrough in order to use it as a biased pickup anode. It is made from a tantalum sheet with conical recesses where the actual aperture holes of 6 mm diameter are drilled.

3.1.1. Ultra-high Vacuum

The deposition of thin films of nanometer thickness is typically a process that takes place in vacuum and the demands on purity of the films and the reactivity of the alkali

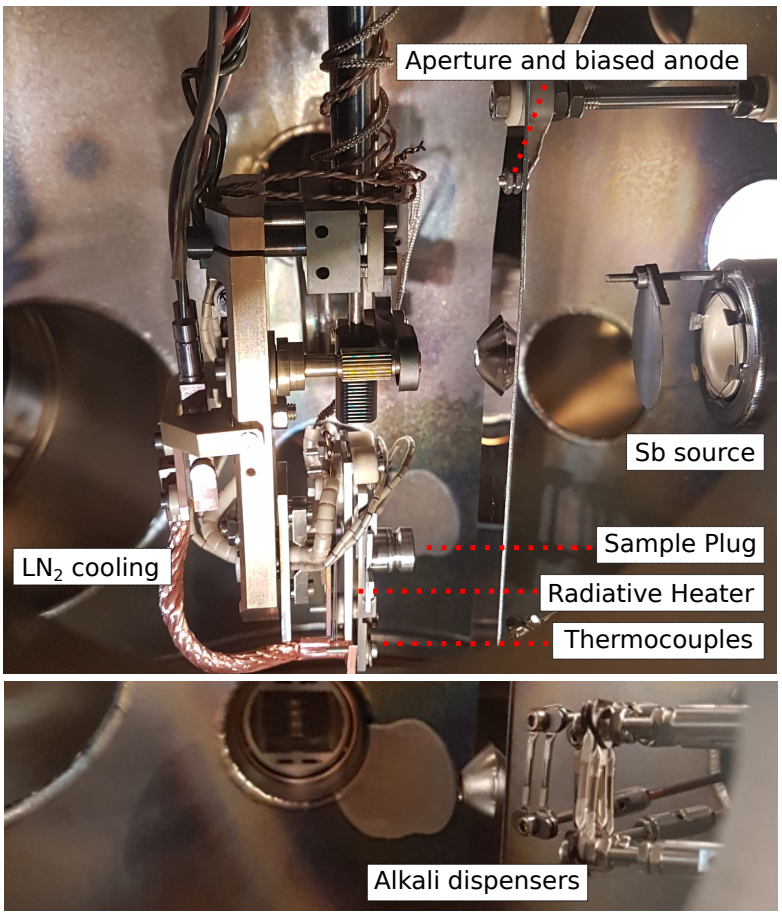

Figure 3.2.: View into the preparation chamber. The sample holder mechanism with heater and cooling as well as the aperture and Sb source are annotated. Reprinted from [10]

metals require that it be an ultra high vacuum (UHV) process. UHV is commonly considered as the absolute pressure regime below 10^{-9} mbar. The vacuum vessels are made from 1.4429 stainless steel and sealed by copper gaskets that are compressed between the knife edges on each side of a flange (compatible to the CF standard). Starting from a system that is vented, i.e. at atmospheric pressure with air or nitrogen, a series of pumping concepts is required to lower the total pressure by up to 14 orders of magnitude. Initially, the chamber is evacuated by means of a scroll pump which supports high mass flows and can be operated at high (atmospheric) pressures on the inlet and outlet side. A final pressure of 10^{-2} mbar can be reached using this pump, which is sufficient to start a turbomolecular pump (turbo). The turbomolecular pump consists of rotating turbine blades alternated with static blades. It operates at pressures below 1 mbar where gas molecules are separated and weakly interacting, and can have high compression ratios of 10^9 when a Holweck stage is included on the high-pressure side. Gas can flow through the stopped pump and typically the chamber is evacuated through the turbo which can be started once the scroll pump has reached its final

pressure. A final pressure of 10^{-8} mbar can be reached in the preparation chamber by means of this pump, which is an equilibrium situation between desorption of gas molecules from the inner surfaces and pumping speed.

The turbomolecular pump is also the main pump during a bakeout of the system. Baking is necessary to attain lower pressures in the chamber and especially to reduce the water vapor partial pressure. The entire system is heated by heating strips to 120°C over several days (typically over a weekend). The increased temperature leads to a higher desorption rate of molecules that are adsorbed to the chamber wall. The temporarily higher pressure allows a higher mass flow through the turbo pump, effectively removing a large portion of the volatile molecules from the chamber. The desorption rate of a baked stainless steel surface can be 2-3 orders of magnitude lower than an unbaked surface, thus allowing to reach correspondingly lower final pressures. The baking procedure also involves a short heating (degassing) of all filaments, evaporation sources and chemical pumps in the system. The detailed procedures to vent, evacuate and bake the system are documented in the standard operating procedures which were developed and documented within the scope of this work.

Ultimate final pressures $< 5 \cdot 10^{-10}$ mbar can only be reached by means of chemical pumps like ion getter pumps (IGP) and non-evaporable getter (NEG) pumps. IGPs use Titanium plates at a high potential which attract ions and chemically bond them or bury noble gas ions within the Ti bulk. Surrounding molecules are ionized on impact with an ion in the pump and thus sustain the ionization of residual gas species within the pump. NEG pumps are porous surfaces of a Zirconium-Aluminum alloy with a very high surface that physically bond (adsorb) inert gas species and chemically bond reactive gas species. The nominal pumping speed for NEGs is typically given for Hydrogen and can be up to 2000 l/s per module but the pumping speed for other gases is much lower. NEGs do not pump noble gases, thus, they are used in combination with ion getter pumps. In the preparation chamber, an IGP with a pumping speed of 150 l/s and a NEG pump with a nominal pumping speed of 1500 l/s are used to hold a base pressure of $3 \cdot 10^{-10}$ mbar.

During the preparation of a photocathode it is desirable to know the composition of the residual gas in the preparation chamber. A relatively high partial pressure of inert species such as argon or hydrogen might not influence the quality of the sample while the presence of reactive species such as H_2O or oxygen will definitely reduce the quality of the sample or even prohibit the growth of a photosensitive surface.

Once the preparation of a sample has started, nothing can be done about the release of gas species from the evaporation sources. The pumping speed is finite and the only way to reduce gas production is to lower the temperature of the sources which would essentially stop the growth. It is therefore key to maintain purity during the assembly, to degas all sources and instruments prior to the preparation, and to measure the relative gas production of each component by residual gas mass spectrometry. The difference of the rest-spectrum at a base pressure of $3{\cdot}10^{-10}$ mbar and the spectrum

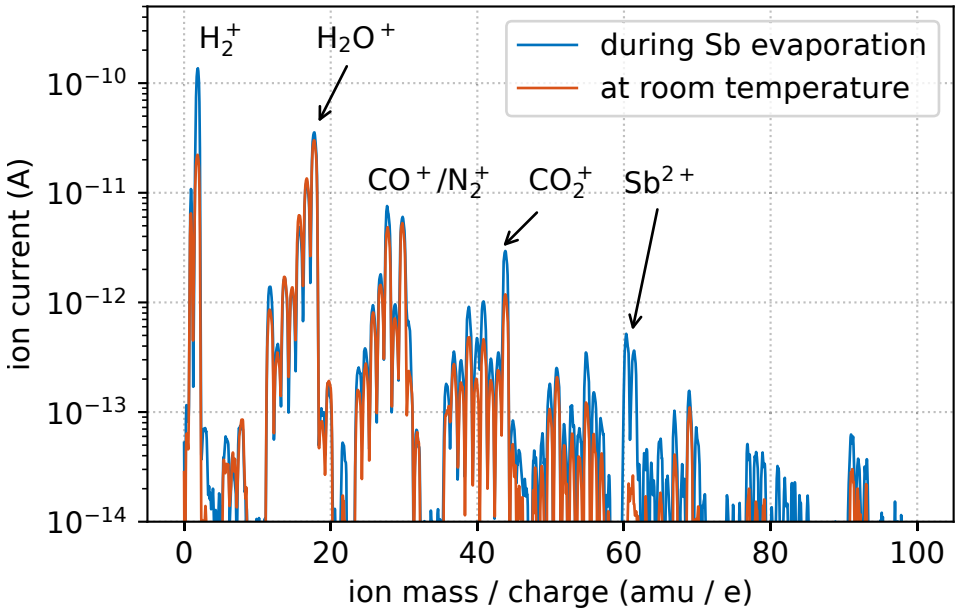

Figure 3.3.: Residual gas mass spectrum of the preparation chamber at room temperature and during antimony evaporation. Prominent peaks are labeled with their respective gas species.

during evaporation of antimony is shown in Fig. 3.3. Note that the main contributions to the elevated pressure of $1{\cdot}10^{-9}$ mbar during evaporation are due to H_2, N_2, CO_2, and Sb itself. The signals due to H_2O and O_2 remain constant.

3.1.2. Elementary Antimony and Alkali Vapour Sources

Elementary antimony is evaporated by thermal sublimation from high purity beads (99.999% purity, Alfa Aesar) which are heated to 420°C in an effusion cell. The boron nitride (pBN) crucible is heated by a tungsten filament and the heating current is controlled in a PID control loop which stabilizes the temperature to ±0.1 K - tight control of the target temperature is necessary to reach a constant deposition rate as shown in Fig. 3.4. The whole evaporator setup is enclosed in a water cooled shroud to reduce the heat load on the vacuum system.

Elemental alkali metal vapor is generated from dispenser sources. These devices are industrially available and provide few mg quantities per piece by decomposition of alkali chromates with a reducing agent. The chromate salts of alkalis have the general formula A_2CrO_4, where A is the alkali ion. The reaction with Zr produces volatile elementary alkali atoms and solid products as described in [56, 57]:

$$2\,Cs_2CrO_4 + Zr \longrightarrow 4\,Cs + ZrO_2 + 2\,Cr_2O_3 \tag{3.1}$$

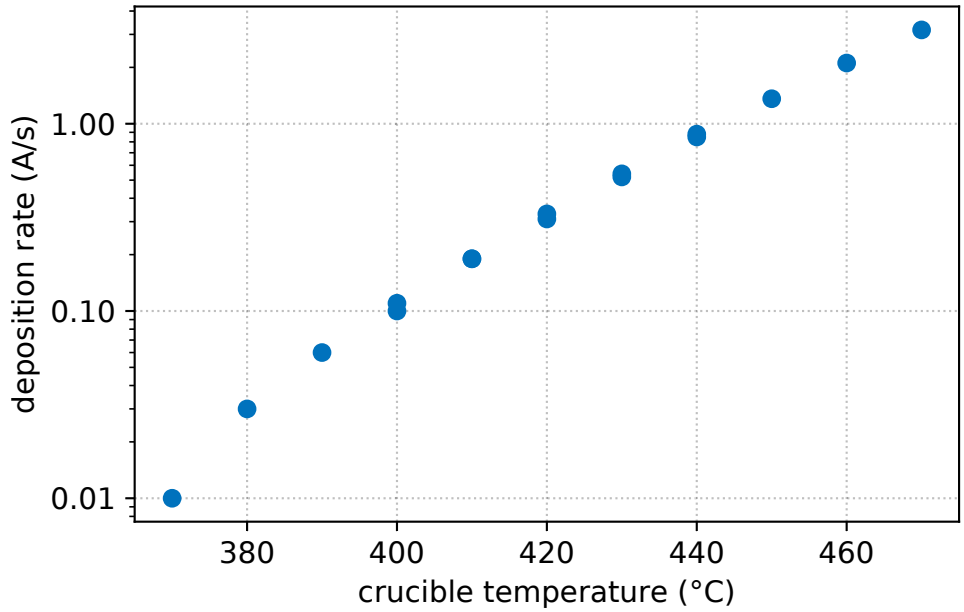

Figure 3.4.: Deposition rate of Antimony from the effusion cell and its dependence on the crucible temperature.

The oxygen atom released during the reaction is nascent and thus readily reacts with the reducing agent before it may be released to the vacuum. The Zr alloy used in the dispensers (Zr with 16% Al) is commonly used as a getter material in vacuum pumps and in this case also acts to reduce the gas evolution from the dispenser. At high temperatures the material reacts with reactive gas species and allows the gas molecules to diffuse into the bulk so that the surface does not saturate. The manufacturer (SAES) quotes a gas production below 4 mbar l/s hydrogen and below 1 mbar l/s CO at operation temperature (700°C) [58]. The actual gas load for degassed dispensers is much lower, considering that the hydrogen partial pressure does not exceed $5{\cdot}10^{-10}$ mbar during deposition while the pumping speed for hydrogen is constant at 1500 l/s.

The dichromates are not favorable for this application because they decompose at high temperatures above 400°C, releasing oxygen:

$$4\,Cs_2Cr_2O_7 \longrightarrow 3\,O_2 + 2\,Cr_2O_3 + 4\,Cs_2CrO_4 \tag{3.2}$$

All chromate salts are toxic and carcinogenic. The lethal doses are around 150 mg/kg (LD50, mouse or rat, [59–61]). The dispensers used in this work are closed devices where small quantities of about 30 mg of the alkali chromate powder is enclosed in a nichrome boat and the opening slit is sealed with a nichrome wire. Therefore, no direct handling of the material is necessary, but standard safety precautions are employed.

3.2. Spectral Response

The spectral response of a photocathode is defined as the wavelength (or photon energy) dependent quantum efficiency QE(λ), and the QE is the unitless fraction of electrons liberated per incident photon. The spectral response is an important quantity to consider when discussing different materials because it allows to judge the trade-off between QE and intrinsic emittance within the boundary conditions of available drive laser wavelengths. Further, one may deduce the work function of a material from the onset of photoemission in the QE curve (see below) as well as learn about the behavior of a sample as it ages due to surface contamination, segregation or oxidation. The spectral response is determined from the measurements of spectral flux (light power) P_{ph} of the light source, photocurrent I_{ph}, and dark current I_{dark}, which are recorded while the wavelength of the monochromator is scanned.

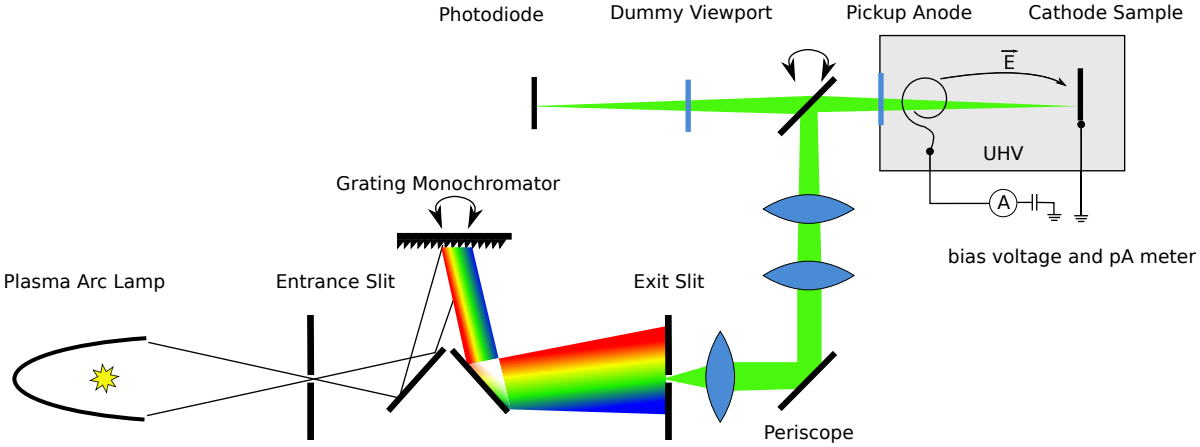

Figure 3.5.: Sketch of the spectral response setup. A pivoted periscope allows to switch between the measurement of photocurrent and calibration of the spectral flux.

In practical units, the QE is expressed as

$$QE = \frac{1240\,\mathrm{eV\,nm}\,(I_{\mathrm{ph}}(\lambda) - I_{\mathrm{dark}})}{\lambda\, P_{\mathrm{ph}}(\lambda)} \tag{3.3}$$

and its uncertainty as

$$\Delta QE = QE\sqrt{\left(\frac{\Delta I}{I}\right)^2 + \left(\frac{\Delta P}{P}\right)^2 + \left(\frac{\Delta\lambda}{\lambda}\right)^2}\,. \tag{3.4}$$

In the present setup all values are digitized in the specified wavelength range by a Python program. The commissioning and programming of the system was part of Hans Kirschner's Master thesis [62] under supervision of the author.

The setup to measure the spectral response is an integral part of the photocathode development system and is sketched in Fig. 3.5. It comprises a tunable light source (Horiba PowerArc), beam routing optics, a calibrated photodiode power meter (ThorLabs PM100D and S130VC) and the photocurrent pickup anode and picoampere meter (Keithley model 6487). The white light generated from a Xe arc lamp source is focused by the ellipsoidal mirror housing onto the entrance slit of a grating monochromator. A reflecting long wave pass filter blocks light below 345 nm to avoid passage of the second order reflection of the grating monochromator. The monochromator is in Czerny-Turner geometry and its grating is optimized for operation in first order with a blaze for 500 nm (Littrow configuration). In order to perform the two necessary measurements of photocurrent and optical power at each wavelength, the beam routing section can be rotated around the periscope to illuminate either the sample behind a UHV viewport or the photodiode behind a dummy viewport.

The components were selected to obtain a usable wavelength range in the visible spectrum from 370 to 700 nm which is the relevant range for spectral response measurements on semiconductor photocathodes. The spectral flux is determined using a calibrated photodiode power meter and is displayed in Fig. 3.6. At the default measurements settings it is on the order of a few μW and results from the wavelength dependent transmission efficiency of the diffractive grating and the spectrum of the radiant power from the white light source that is focused through the entrance and exit slits of the monochromator.

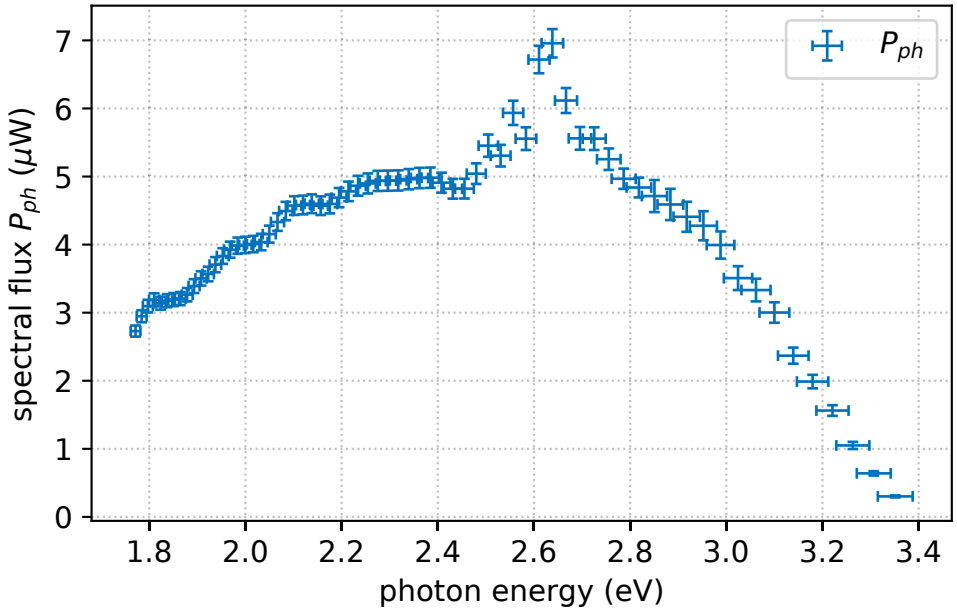

Figure 3.6.: Available spectral flux of the illuminating setup. The spectral flux is calibrated regularly to compensate for drifts of the lamp radiant power.

The uncertainty is dominated by the calibration of the photodiode (ΔP) which results in a 3-5% uncertainty of the total QE measurement. The jump in the photodiode

accuracy at 2.8 eV is due to a discontinuity in the calibration certificate supplied by the manufacturer. Statistical errors are typically below 0.5% for the sets of 20 data points taken at each wavelength, but can be up to 10% at the long wavelength limit where the measured photocurrent approaches the noise level of 0.1 nA. The constant bandwidth of the monochromated light of 4 nm introduces an additional systematic uncertainty of 1%. Errors due to realignment of the apertures in the beam routing section and long-term drift of the lamp electrodes are avoided by taking calibration the spectral flux for each measurement. In Fig. 3.7 the contributions to the uncertainty are shown for a typical measurement.

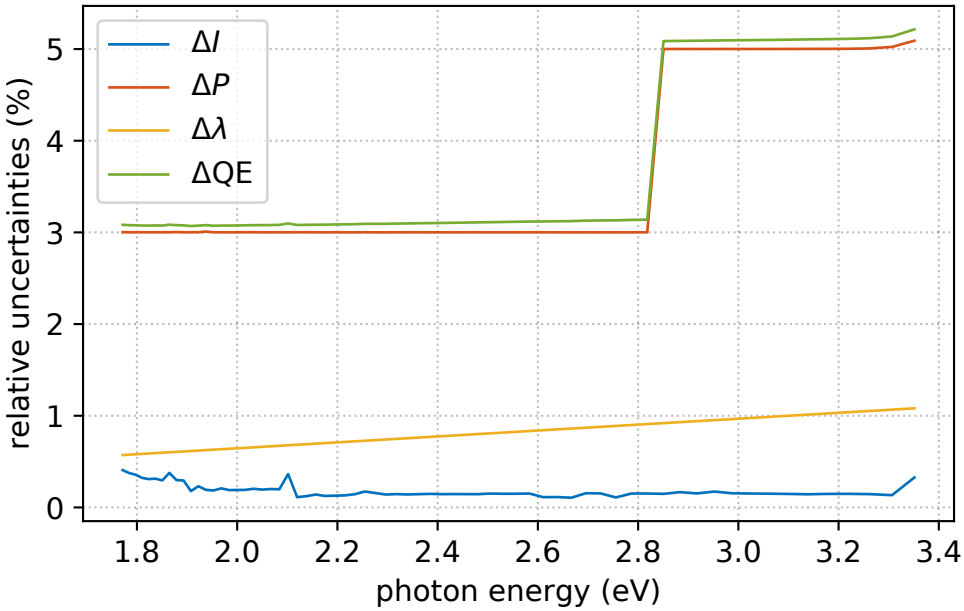

Figure 3.7.: Individual components of the uncertainty in the QE measurement.

As an example, the spectral response curve as obtained from sample P014 is displayed in Fig. 3.8. The excitation energy is given in eV. One can note from this curve the high quantum efficiency above 0.1 (10%) in the region above 2.4 eV (515 nm) as well as the steep onset of photoemission in the region above 1.8 eV.

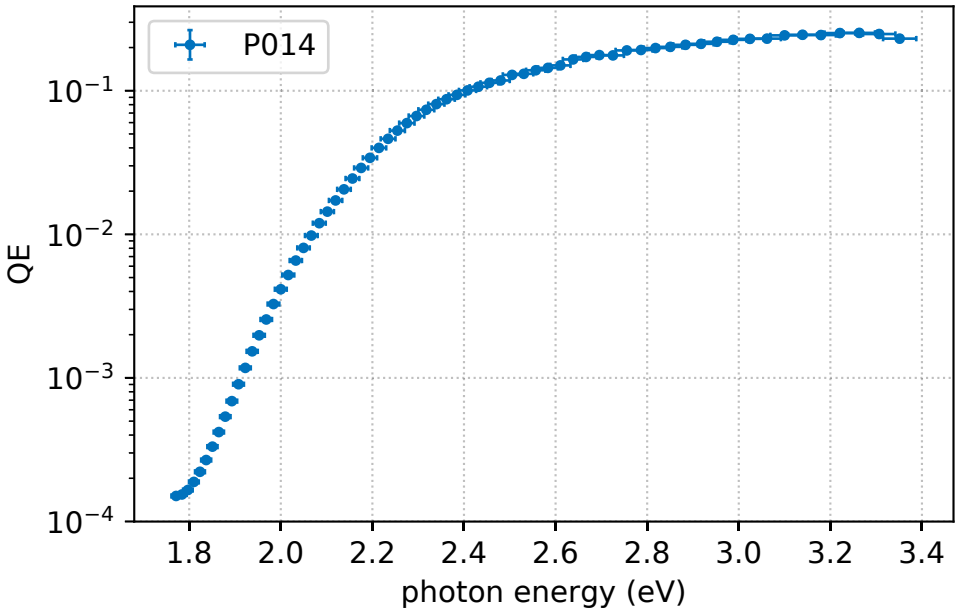

Figure 3.8.: Typical spectral response curve of a Cs-K-Sb sample.

3.3. X-ray Photoelectron Spectroscopy

Among the surface science analytical methods, X-ray photoelectron spectroscopy (XPS) is well established and is commonly employed to gain insight to the chemical composition and electronic structure of surfaces, thin films, and interfaces. XPS is a quantitative method in the sense that it allows to determine absolute concentrations of chemical elements and their respective oxidation state [63]. The information depth is determined by the mean free path of the photoelectrons leaving the sample and is typically a few nanometers, thus, XPS is a surface sensitive method. The detection limit for trace quantities is governed by the cross section of the elements with the exciting X-ray radiation and is limited to a few percent for light elements and about 0.1 percent for heavy elements [64].

In an XPS experiment the sample is exposed to a beam of X-ray photons and the electrons liberated from the sample by the photoelectric effect are recorded using an electron spectrometer. A spectrum is then compiled as intensity (e.g. electron counts per second) versus kinetic energy of the electrons.

Conservation of energy dictates the basic equation of XPS, which describes the energy of the main peak, assuming no interaction of the ejected electron with the remaining sample (sudden approximation).

$$E_{\mathrm{K}}^{\mathrm{meas}} = h\nu - E_{\mathrm{B}}^{\mathrm{F}} - e\Phi_{\mathrm{sp}} \tag{3.5}$$

In this notation, it holds for metallic and semiconducting samples in electrical contact with the spectrometer. Here $E_{\mathrm{K}}^{\mathrm{meas}}$ is the kinetic energy of the emitted electron, $h\nu$ is the excitation photon energy, $E_{\mathrm{B}}^{\mathrm{F}}$ is the binding energy of the core state with respect to the Fermi level and Φ_{sp} is the work function of the spectrometer. E_{K} is the quantity determined during the measurement but spectra are typically analyzed in terms of E_{B}. Thus, the energy scale of the spectrometer must be accurately linear and have its work function calibrated. The derivation of equation 3.5 is considered in some detail in appendix A because the definitions used are of some relevance to the work function and energy spectrum measurements described below. Also in appendix A is the discussion of the energy calibration of the instrument which was done in the commissioning phase of this work.

Figure 3.9 shows an example of one such XPS spectrum where the intensity is recorded versus electron binding energy. One can clearly discriminate electronic core states which manifest as intense peaks in the spectrum. Reference libraries allow for identification of the peaks as annotated in the Figure [65, 66].

Further features found in the spectrum are the lines originating from Auger processes which can be attributed to the Mo MNV and O KLM transitions. The high intensity background on the high binding energy side (low kinetic energy) originates from

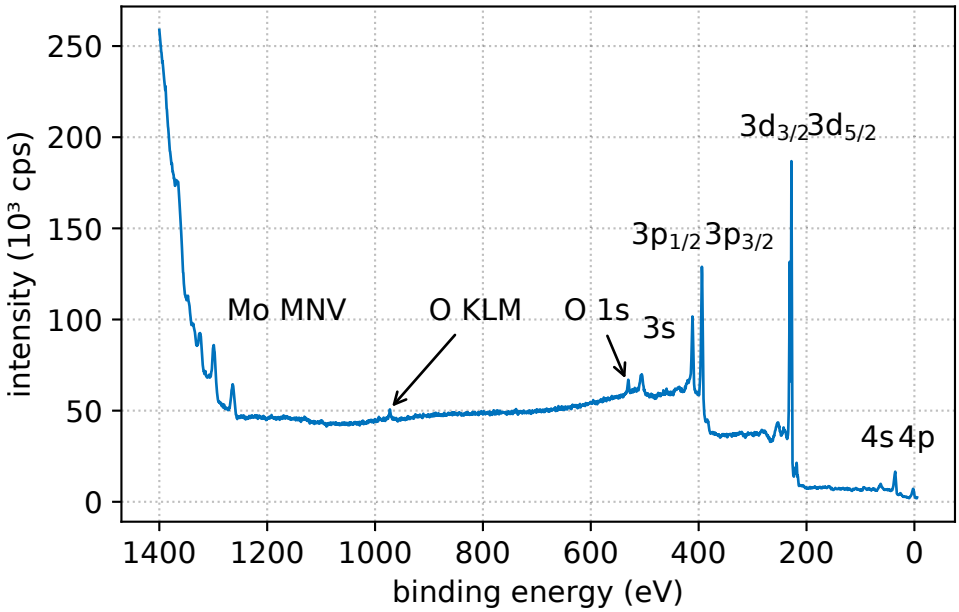

Figure 3.9.: X-ray photoelectron survey spectrum of Molybdenum excited by Al Kα radiation (non-monochromatic).

secondary electrons and is usually not recorded up to the cut-off in order to protect the electron multiplier in the spectrometer from too high count rates.

The step-like background, that increases with each peak towards higher binding energies is a result of inelastic scattering events. Only a fraction of the excited electrons will escape the sample without scattering and give rise to the distinct peaks for which the energy relation in equation 3.5 holds. The scattered electrons loose a part of their energy and contribute to the background at higher binding energy (lower kinetic energy). Figure 3.10 displays a compilation of the electron's inelastic mean free path (IMFP) versus energy inside various materials. The general form of the IMFP function is universal and depends only lightly on the material. It has a minimum of about 5 Å at kinetic energies between 50 and 70 eV and stays below 30 Å for the energies < 2000 eV encountered in XPS experiments.

These short free path lengths bring about the surface sensitivity of XPS: as described by Beer-Lambert's Law $I = I_0 e^{-\mathrm{d}/\lambda}$, with 68% probability an electron will have scattered after traveling a distance of $1\,\lambda$, and with 95% after traveling $3\,\lambda$. Thus, the signal obtained in an XPS experiment originates from the few nm thick surface slab that lies within the overlap of X-ray irradiation and analyzer acceptance area [64]. The fact that the average path length traveled depends on the analyzer angle can be used to obtain e.g. the thickness of an overlayer by altering the analyzer angle [63].

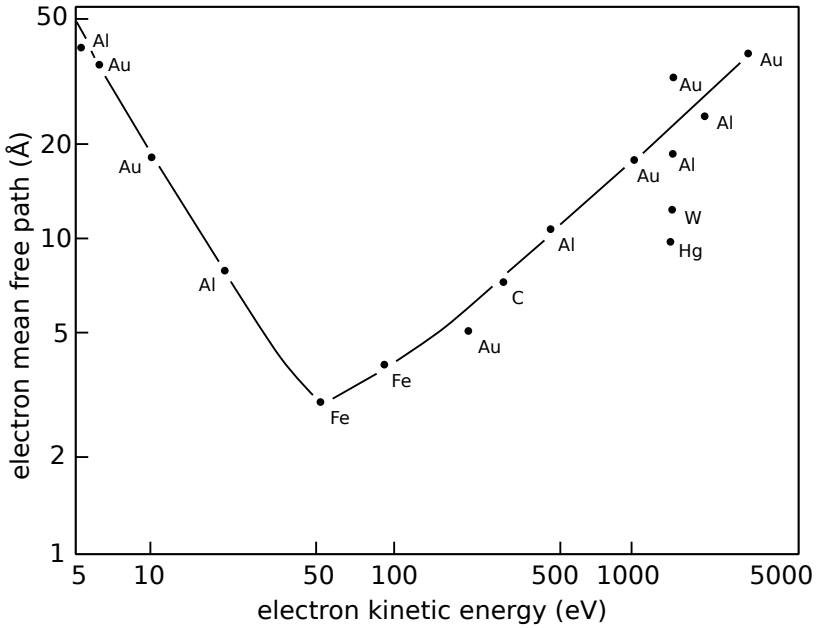

Figure 3.10.: Electron mean free path as a function of their kinetic energy for various metals, with a sketch of the universal IMFP relation. Data from [67].

3.3.1. Experimental Setup

The analysis section of the photocathode system is mounted below the preparation chamber. The sample can be introduced to the analysis chamber by extending the z drive of the sample manipulator through the opened valve between the two chambers. In total, five degrees of freedom allow the adjustment of the sample position. The sample can be moved in three perpendicular directions, where z is vertical, x is the analyzer axis (normal to the sample surface) and y is the horizontal axis, parallel to the sample surface. Additionally the sample can be rotated around the z and x axes.

A hemispherical spectrometer (SPECS Phoibos 100 CCD) is mounted with it's lens system along the x axis. The X-ray source (SPECS XR-50) is mounted at an angle of 54° w.r.t the analyzer in the x-y plane, and provides a Mg and Al dual anode but is not monochromatic. Generally, despite its larger line width, the Al anode is employed due its more common use and the higher availability of reference data for this excitation energy. In order to achieve maximum acceptance of the analyzer lens system, the sample should be positioned at a nominal distance of 40 mm from the analyzer. While the position and angle of emission of photoelectrons must be within narrow constraints in order to pass the analyzer, the excitation area illuminated by the X-ray source is rather broad. The X-ray source was mounted on a tip-tilt bellow and can be aligned to compensate for tolerances in the vacuum flange geometry.

The energy resolution of the instrument can be determined from the line width of measured Ag 3d peaks and the procedure is outlined in appendix A. The measured width (FWHM) is a convolution of the energy width of the exciting radiation ΔE_x, the energy resolution of the electron analyzer ΔE_A which depends on the energy window or pass energy, and the physical line width ΔE_2 of the electronic state in the sample

$$\Delta E = \left(\Delta E_x^2 + \Delta E_A^2 + \Delta E_2^2\right)^{1/2} \tag{3.6}$$

From the data one may conclude that only a moderate additional uncertainty of 0.37 eV is introduced by taking survey spectra at 20 eV pass energy and 0.19 eV by taking fine spectra of individual transition at 10 eV pass energy.

In summary the standard operating mode for the XPS instruments is to run the X-ray source at 12.5 kV accelerating voltage and 20 mA emission current on the Al anode and setting the analyzer to medium magnification mode with a 7x20 mm entrance slit, 15 mm iris and 20 or 10 eV pass energy, depending on the resolution required. The selected settings are a reasonable compromise between resolution and electron count rate. Typical peak heights over background are $7.5 \cdot 10^4$ cps for prominent peaks. Further restriction of the apertures would not lead to drastic improvement of the resolution which is limited by the line width of the non-monochromatized source. Survey spectra in this work are taken at 1 eV steps with 0.1 s exposure time and fine spectra are taken at 0.1 eV steps with 1 s exposure time. These lens settings result in a 1.4 mm diameter of the analyzed area and an angular acceptance of ±5°.

3.3.2. Chemical Shifts

Different oxidation states of an element will lead to a shift of the binding energy of core states versus the pure element and can thus be differentiated, which is called the chemical shift of a peak. If one valence electron is transferred to another atom, the electrons of the ionized atom and its neighbors will relax to a new state, which can be illustrated within the charge-potential model. Consider each atom as a hollow sphere of radius r_V, with the charge q_i of the valence electrons distributed on the surface. Inside the sphere, the potential is constant at q_i/r_V, thus all binding energies of the different core-states are equally affected.

For example, the Mo 3d signal is very sensitive to oxidation [68] and corresponding data is shown in Fig. 3.11. The individual contributions are shown after a deconvolution using a peak fitting routine with three 3d components. Chemical shifts of 3.01 eV for the MoO_2 components and 3.95 eV for the MoO_3 components to higher binding energies are clearly visible. One can also observe a significant broadening of the oxide peaks with respect to the metallic one which is consistent with previous measurements [69].

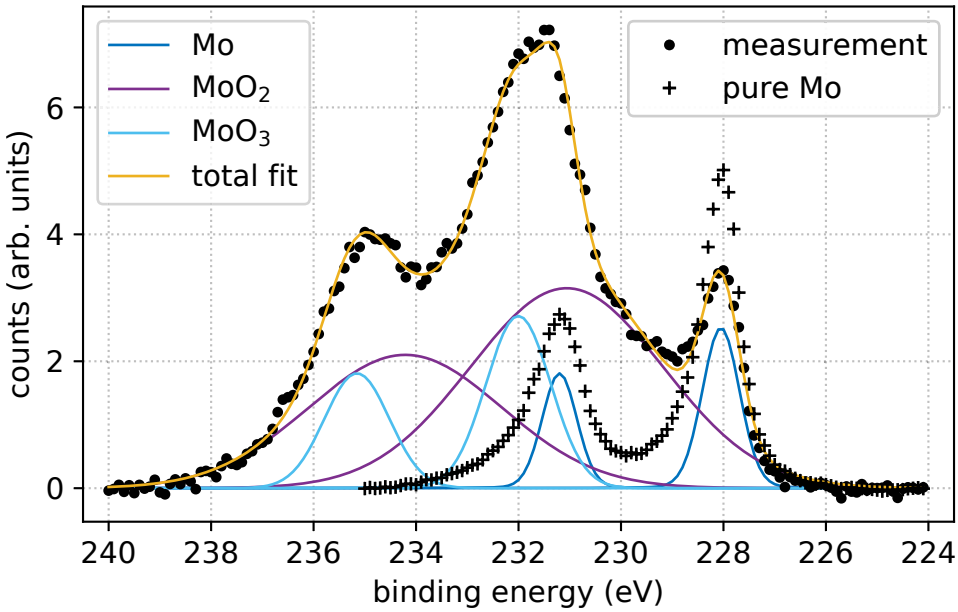

Figure 3.11.: Exemplary data of an oxidized Mo surface displaying chemical shifts of the oxidized states. For reference, also the metallic 3d signal of a pure (sputter etched) Mo surface is shown (black + signs). Colored lines are the individual components of 3d peaks used to fit the oxidized signal.

3.3.3. Quantification

The intensity of a transition in an XPS spectrum depends on the concentration of the atomic species in the sample as well as instrumental parameters:

$$I_{\mathrm{XPS}}(\mu) = F\,T\,D\,A\,\Delta\Omega\,\sigma_{\mathrm{ex}} \int_0^\infty \Phi_0(z',\mu) c_{\mathrm{A}}(z')\mathrm{d}z' \tag{3.7}$$

where the instrumental parameters are determined by the primary flux (X-ray photons) F, analyzer transmission T, detector efficiency D, analyzed area A, and the solid angle of the analyzer acceptance $\Delta\Omega$. Each atomic species contributes to the spectrum relative to its concentration $c_{\mathrm{A}}(z')$ and the excitation cross-section σ_{ex} of its electronic states. The effect of electron transport is contained in the depth-distribution function Φ_0, where here, it is assumed to consist of only the effect of inelastic electron scattering:

$$\Phi_0(z',\mu) \approx e^{-z'/\mu\lambda_{\mathrm{IMFP}}} \tag{3.8}$$

i.e. the signal originating from atoms in the bulk of a sample is strongly attenuated by electron scattering. This is the primary reason for the surface sensitivity of XPS.

During analysis of the composition of a sample, the instrumental conditions are kept constant. Thus, if a constant depth distribution of the concentration $c_0(z) \equiv c_0$ is assumed one obtains

$$\int_0^\infty c_\mathrm{A} e^{-z'/\mu\lambda_\mathrm{IMFP}} \mathrm{d}z' = \lambda_\mathrm{IMFP} c_\mathrm{A}\,, \tag{3.9}$$

and for the ratio of two concentrations

$$\frac{c_\mathrm{A}}{c_\mathrm{B}} = \frac{I_\mathrm{A}}{I_\mathrm{B}} \frac{\sigma_\mathrm{ax,B}\lambda_\mathrm{IMFP,B}}{\sigma_\mathrm{ax,A}\lambda_\mathrm{IMFP,A}}\,. \tag{3.10}$$

For the purpose of this work, cross-sections from Scofield are used [70] and IMFPs are obtained from the program SESSA using the TPP-2M formula [71, 72]. A set of scripts has been developed in Python to quickly quantify the composition of a sample from the relative peak intensities as described above. The utility functions and scripts for the peak fitting and quantification are published on GitHub [73]. The spectra are read directly from SpecsLab data files using a routine adopted from the PyExpLabSys project [74]. After a Shirley background subtraction, the peak intensity is integrated using a trapezoid sum from the discrete data points. The model was validated against the built-in quantification in CasaXPS and has the advantage that identical parameters are used automatically for each sample and spectrum while the process of selecting parameters in a graphical application like CasaXPS is tedious and error prone.

A direct integration of measured intensity is not feasible when peaks from different species overlap. In this case a deconvolution of the measured signal is necessary by fitting synthetic peak shapes to the individual components. In the example of Sb 3d and O 1s peaks one typically finds contributions from Sb 3d 3/2 and 5/2 in the elemental and reduced configuration which are taken into account e.g. in the discussion of stoichiometry in section 5.2.

3.4. Transverse Emittance Measurement

The intrinsic transverse emittance is the contribution to the total emittance originating from the photoemission mechanism. It is a property of the photocathode material that depends on operation parameters like temperature and excitation wavelength. The total emittance always includes additional contributions from electric and magnetic fields, their aberrations, and space charge effects which can be in the same order of magnitude. An accurate description of the additional contributions is thus essential for the measurement of the intrinsic emittance.

Efforts to measure the energy and angle distribution of photoemitted electrons traditionally follow three different paths [75]. The most prominent way are hemispherical and cylindrical electron analyzers as employed in XPS and UPS experiments. Usually the analyzers are optimized for medium to high kinetic energies between 10 and 1000 eV and no, or few Volts of bias are applied between the sample and the detector. These devices are well characterized and accurate but inefficient for the detection of low energy electrons as the transmission becomes very low with lower energies and stray fields from work function variations and the geometry of the metallic experimental setup will distort the measured spectra.

Two similar approaches analyze the electron beam after acceleration in a short gap between cathode and anode. The gap is either designed in a parallel plate geometry, thus aiming to achieve a mostly flat field geometry in the volume passed by the electrons - this is the design followed by the Momentatron [76, 77] and TESS experiments [78–80]. Or, the gap is between a flat cathode and circular anode, which is a typical DC gun design. In this case, one aims to have an accurate description of the electric field distribution and its effect on the beam properties. One may then conclude the beam emittance from a reconstruction of the beam evolution in the static electric field or from a waist scan using a well characterized solenoid lens. This is the design employed by the TE meter experiment which was developed at Cornell University [81].

3.4.1. The TE meter

The name TE meter of the experimental setup refers to a compact DC photoemission gun enclosed in an UHV chamber that is connected to the sample transfer system in Cornell's photocathode laboratory [75]. This device was used to measure the data presented in chapter 6. The electron beam propagates through a short beamline which is enclosed by a solenoid and two pairs of corrector coils. Photocathodes are carried on plug substrate holders as shown in Fig. 3.12, where a polished Mo, Si, or GaAs wafer can be clamped to the front side of a plug. The measurement setup is displayed in Fig. 3.12 (a) and comprises a copper thermal reservoir with a plug holder on the top surface where a cathode sample rests (green), a ring anode (blue) which is held

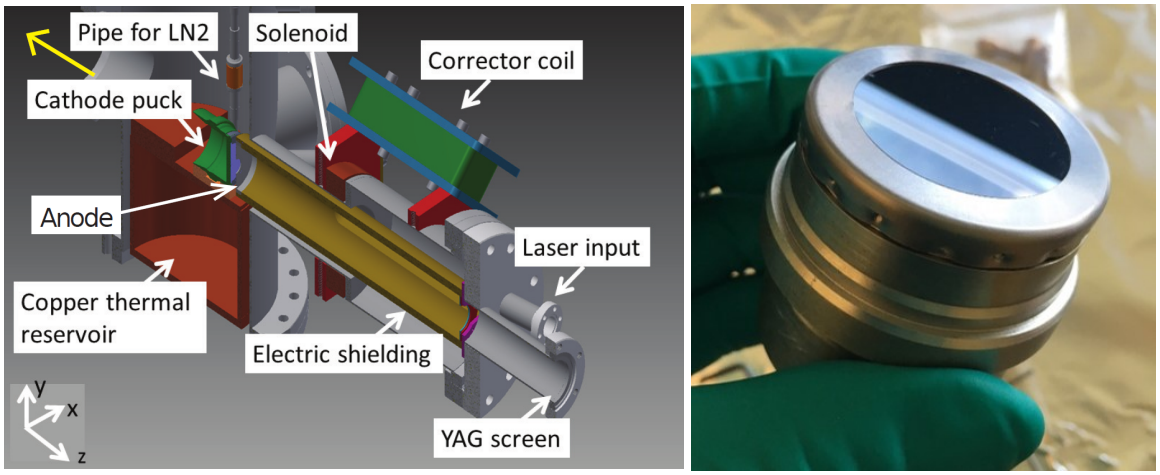

Figure 3.12.: Drawing of the TEmeter and photograph of the substrate geometry used in the experiments.

by the electric shielding pipe (brown) and a YAG screen which is not shown. The reservoir can be filled with liquid nitrogen in order to cool the sample.

A bias of up to 10 kV can be applied to the reservoir and sample while the anode, shielding and chamber are at ground potential. The static electric field geometry is obtained from a 2D solution of the Poisson equation as illustrated in Fig. 3.13. The transverse intensity distribution at the screen is captured using a lens-coupled CCD camera which is mounted outside of the vacuum chamber behind a viewport.

A measurement of the beam emittance can be performed either by variation of the electric bias (voltage scan) and solution of equation 3.14 with the corresponding electric field maps or by variation of the solenoid current and moving the beam waist through the screen position. A solution of equation 3.14 then requires the removal of the Larmor rotation from the screen images and knowledge of the transfer matrices in a combined electric and magnetic field distribution.

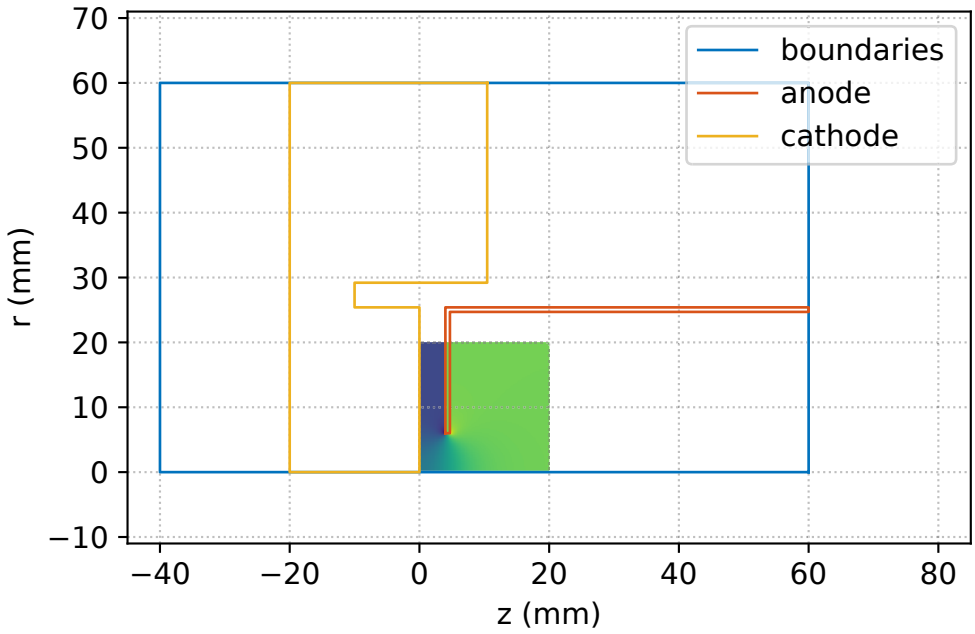

Figure 3.13.: Geometry for the 2D simulation of the electric field distribution inside the TE meter. The field map shows the magnitude of the z-component of the resulting field as computed by Superfish.

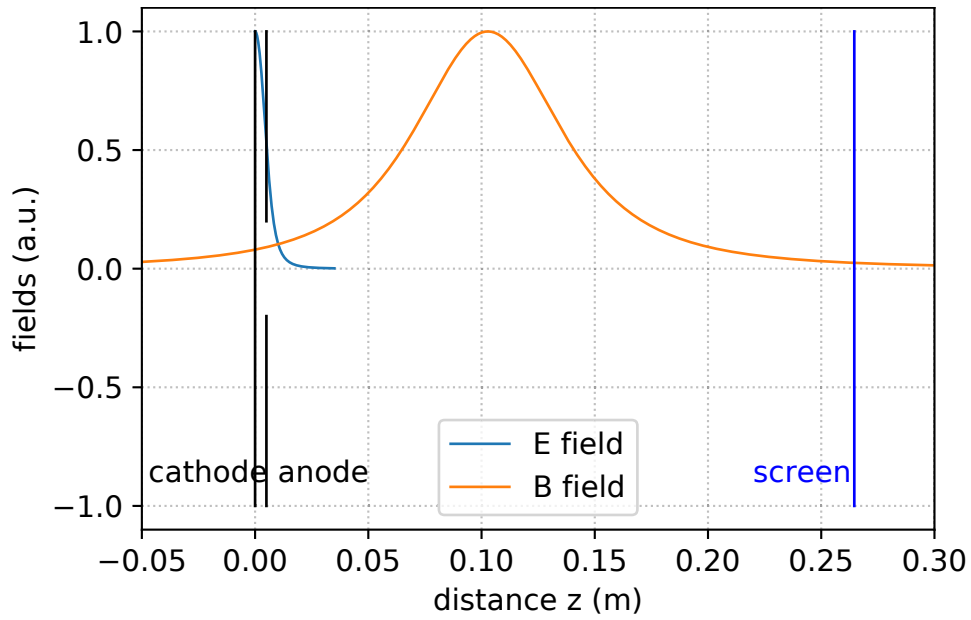

Figure 3.14.: Schematic illustration of the TE meter device. Electrons propagate from left to right through the electric and magnetic field. Normalized field amplitudes on the central axis are shown.

3.4.2. Beam Optics

The task in evaluating data from the TE meter (as in any emittance measurement) is to compute the initial beam properties from the beam properties that are accessible by measurements at the screen.

The notation below follows Minty and Zimmerman [82] and the method to compute the transfer matix in combined electric and magnetic fields is that of Gulliford *et al.* [83, 84].

Using the linear beam optics theory one writes the propagation of a particle in transverse directions as

$$\begin{pmatrix} x \\ x' \end{pmatrix}_{\mathrm{f}} = \begin{pmatrix} R_{11} & R_{12} \\ R_{21} & R_{22} \end{pmatrix}_{\mathrm{fi}} \begin{pmatrix} x \\ x' \end{pmatrix}_{\mathrm{i}} \tag{3.11}$$

where x and x' are the transverse position and divergence of one particle and the matrix $\mathbf{R}$ is the transport matrix. The indices i and f denote initial (cathode) and final (screen) positions, respectively. The transfer matrix is computed for stepwise slabs in beam direction as described in [83].

It is equivalent to express the linear transport equation in terms of the Twiss parameters

$$\begin{pmatrix} \beta \\ \alpha \\ \gamma \end{pmatrix}_{\mathrm{f}} = \begin{pmatrix} R_{11}^2 & -2R_{11}R_{12} & R_{12}^2 \\ -R_{11}R_{21} & 1 + 2R_{12}R_{21} & -R_{12}R_{22} \\ R_{21}^2 & -2R_{21}R_{22} & R_{22}^2 \end{pmatrix}_{\mathrm{fi}} \begin{pmatrix} \beta \\ \alpha \\ \gamma \end{pmatrix}_{\mathrm{i}} . \tag{3.12}$$

The first line of this system of equations is accessible to measurement as $\beta_{\mathrm{f}}\epsilon = \langle x^2 \rangle$ is the beam size on a screen. Thus, the left-hand side of

$$\beta_{\mathrm{f}}\epsilon = \begin{pmatrix} R_{11}^2 & -2R_{11}R_{12} & R_{12}^2 \end{pmatrix}_{\mathrm{fi}} \begin{pmatrix} \beta\epsilon \\ \alpha\epsilon \\ \gamma\epsilon \end{pmatrix}_{\mathrm{i}} \tag{3.13}$$

can be measured for many optics settings where the transport matrix $\mathbf{R}$ is known (e.g. from simulations) and the resulting system of equations can be solved in a linear regression to obtain the unknown initial conditions.

In this case, following [84], the numerical evaluation is as follows:

Equation 3.13 is written for n measurements as

$$\Sigma_x = \mathbf{B}_x \mathbf{s}_x \tag{3.14}$$

where $\Sigma_x = \left((\sigma_x^{(1)})^2, (\sigma_x^{(2)})^2, \cdots, (\sigma_x^{(n)})^2\right)^T$ contains the measured beam size at each beam setting, $\mathbf{s}_x = (\beta_x \epsilon_x, -\alpha_x \epsilon_x, \gamma_x \epsilon_x)$ is unknown, and

$$\mathbf{B}_x = \begin{pmatrix} (R_{11}^{(1)})^2 & -2R_{11}^{(1)}R_{12}^{(1)} & (R_{12}^{(1)})^2 \\ (R_{11}^{(2)})^2 & -2R_{11}^{(2)}R_{12}^{(2)} & (R_{12}^{(2)})^2 \\ \cdots & \cdots & \cdots \\ (R_{11}^{(n)})^2 & -2R_{11}^{(n)}R_{12}^{(n)} & (R_{12}^{(n)})^2 \end{pmatrix}. \tag{3.15}$$

Generally, when more than three settings have been measured, equation 3.14 will be over-determined and the solution from the linear regression is optimal in a least-squares sense.

Practically, the matrices are weighted by the measurement uncertainty and evaluated as follows. The normalized quantities $\hat{\Sigma}_x^{(i)} = \Sigma_x^{(i)}/\sigma_{\Sigma_x^{(i)}}$ and $\hat{B}_{x,ij}/\sigma_{\Sigma_x^{(i)}}$ are introduced. $\hat{\mathbf{B}}_x$ is generally not square, so multiplication by $\hat{\mathbf{B}}_x^T$ from the left yields

$$\hat{\Sigma}_x = \hat{\mathbf{B}}_x \mathbf{s}_x \tag{3.16}$$

$$\hat{\mathbf{B}}_x^T \hat{\Sigma}_x = \hat{\mathbf{B}}_x^T \hat{\mathbf{B}}_x \mathbf{s}_x \tag{3.17}$$

$$\mathbf{s}_x = \left(\hat{\mathbf{B}}_x^T \hat{\mathbf{B}}_x\right)^{-1} \hat{\mathbf{B}}_x^T \hat{\Sigma}_x \tag{3.18}$$

The geometric emittance can now be obtained as $\epsilon_x = \sqrt{s_{x,1}s_{x,3} - s_{x,2}^2}$. In this form, equation 3.18 can be solved by computer programs, e.g. MATLAB. In this case, the code developed by Hyeri Lee [81] has been employed with minor changes. Figure 6.3 shows one such data set and the fit to the data for the two transverse directions. The field distributions are obtained from static field calculations in the program Poisson Superfish [85].

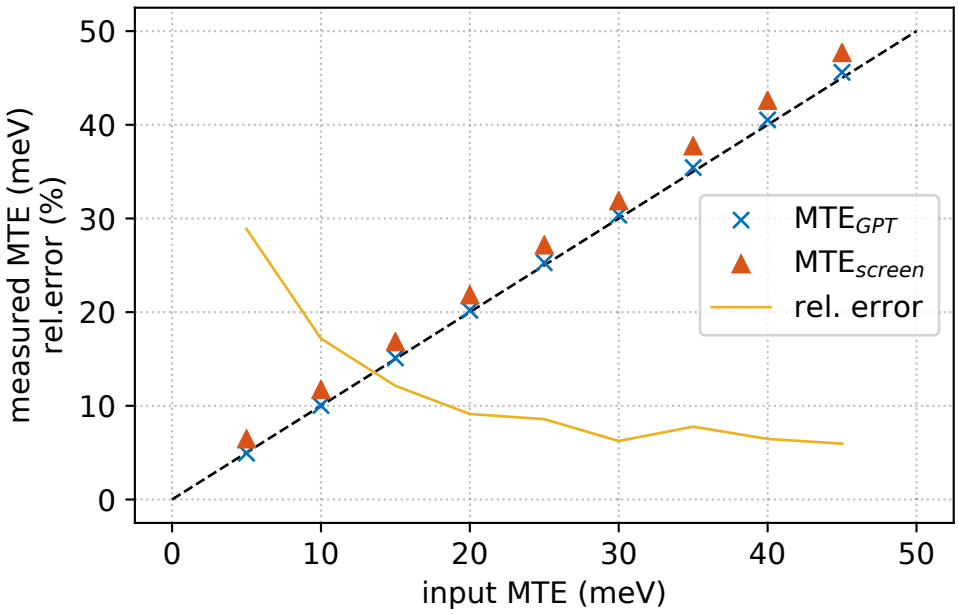

Figure 3.15.: Validation of the analysis routine of the TEmeter. The relative error shown is for the reconstruction from simulated screen images.

3.4.3. Verification of the Model

The accuracy of the reconstruction of the initial beam parameters was validated by numerically tracking a particle distribution through the electric field distribution of the device in a simulation using the General Particle Tracer (GPT [86]). Similar parameters as in the measurement were assumed for the initial beam size and distribution and the applied voltage. For each parameter set, the particle distribution at the screen position was then used to generate a screen image and feed the image back into the same analysis program that was used for the measurements. The initial emittance and MTE was reconstructed first from the beam parameters obtained directly from the simulation and second for the beam parameters obtained from the simulated screen images. The two values are denoted as *GPT* and *screen* in Fig. 3.15.

The algorithm and method itself is accurate and small MTEs can be resolved when assuming the beam parameters obtained directly from GPT. More realistic, however, is the reconstruction from the simulated screen images. Here, a Gaussian point spread function (PSF) was assumed for the resolution of the screen and imaging system. The reconstruction from the images also resembles closely the values initially given to the simulation but it introduces an additional uncertainty from the PSF of the screen and from numerical evaluation of the second moments from the screen distribution. A typical overestimation of 1-2 meV, as evident in Fig. 3.15 leads to a relative error of up to 30%, but still, very small MTE values below 25 meV can be resolved.

Another effect, smaller than the contribution above, was found when changing the shape of the initial particle distribution, e.g. between a flat top or radial Gaussian profile, as well as the shape of the initial momentum distribution. Further, the analysis seems only moderately affected by an uncertainty in the value of the cathode to anode gap. For likely values of ±1 mm, the error contribution was found to be a systematic over- or underestimation, but below 2% when the initial beam size is below 400 μm. Aberrations in the electric field can lead to an emittance growth during passage of the anode. The design of the anode hole has been optimized to mitigate this effect [81] and an emittance increase of less than 5% was found in the simulations for the parameters encountered in this study.

The details of the numerical simulation are as follows. The static field geometry was calculated for different gap distances on a radially symmetric, two-dimensional (2D) mesh of 2.9 million points using the program Poission Superfish which required less than 10000 cycles to converge in all cases. The field was then interpolated on a rectangular 2D grid of 0.1 mm resolution.

Using the field map generated before, different initial particle distributions were tracked through the electric field using the GPT software. In each simulation, 250000 particles were used and space charge forces were neglected. The time step for the Runge-Kutta solver was constrained between 0.01 and 1 ns. For the initial particle distribution radial uniform and radial Gaussian profiles were assumed for the spatial coordinates and the same profiles and a half-sphere distribution were assumed for the momentum coordinates. As the simulation of one measurement consists of several tracking runs with different parameters (e.g. a voltage scan), the simulations were executed in parallel on a computer cluster which required about 1 hour using 4 CPU cores per process and about 300 cores for a parameter scan.

3.5. Control System for the Photocathode Lab

Due to its significance for the commissioning and operation of the photocathode lab, as well as the daily work in the laboratory, a brief introduction to the software control system employed as well as the topography of devices involved is given in this section.

The strategy for deployment of the control system was based on the following requirements: The back-end of the system should be as reliable as possible, i.e. proven by experience in other accelerator and/or surface science experiments. At the same time it should be flexible enough to run on standard PC hardware and accommodate for the frequent changes and additions in hardware during the setup phase of the new laboratory. A log book of events and archive of process data must be provided such that one could look up the conditions during the preparation of a specific sample or another experiment. The front-end should be easy to use and not distract the operator from daily tasks. The system should be capable of operating most of the components

remotely, for example when the laboratory needs to be dark for quantum efficiency measurements.

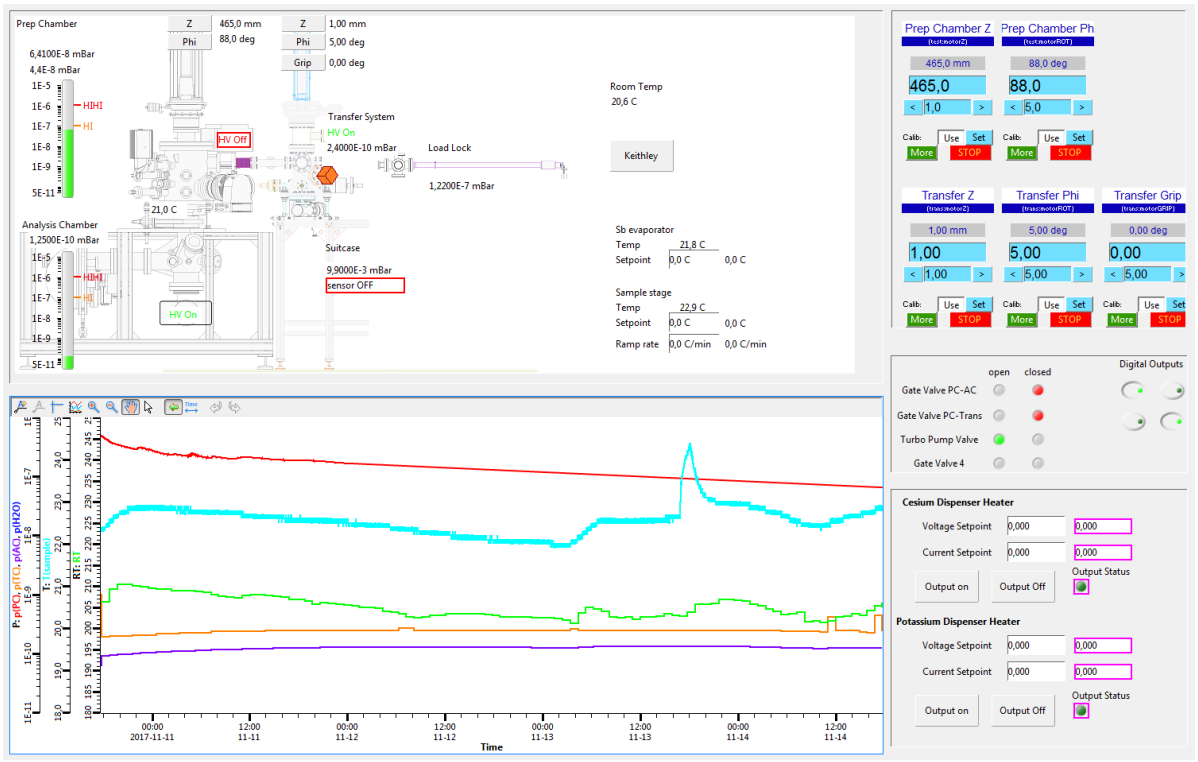

Figure 3.16.: Screenshot of the operator interface of the control system implemented in Control System Studio.

The common control system software at BESSY and many other accelerators is EPICS (Experimental Physics and Industrial Control System [87]) with its various operator interfaces and additions. Nearly all of our requirements are fulfilled by the combination of EPICS software IOCs (input and output controllers) with the archiver appliance [88] and Control System Studio (CSS) [89]. While we cannot guarantee availability of the control system above the level provided by the consumer PC hardware employed, the EPICS software itself is very robust and requires virtually no maintenance. Both EPICS and the archiver appliance are most easily set up on a Linux PC, thus they run within a virtual machine (VM) on the laboratory control computer with Debian (GNU/Linux) operating system. Control System Studio is the graphical operator front end that displays the state of the system, gives access to archived data, and exposes controls e.g. to change temperature setpoints, operate power supplies, move valves etc. All of the software components are developed actively within the accelerator community, licensed as libre and open-source software, and expertise and support is available in mailing lists.

Figure 3.16 displays a screenshot of the main display implemented in CSS. It shows a representation of the system with all relevant vacuum pressures and temperatures,

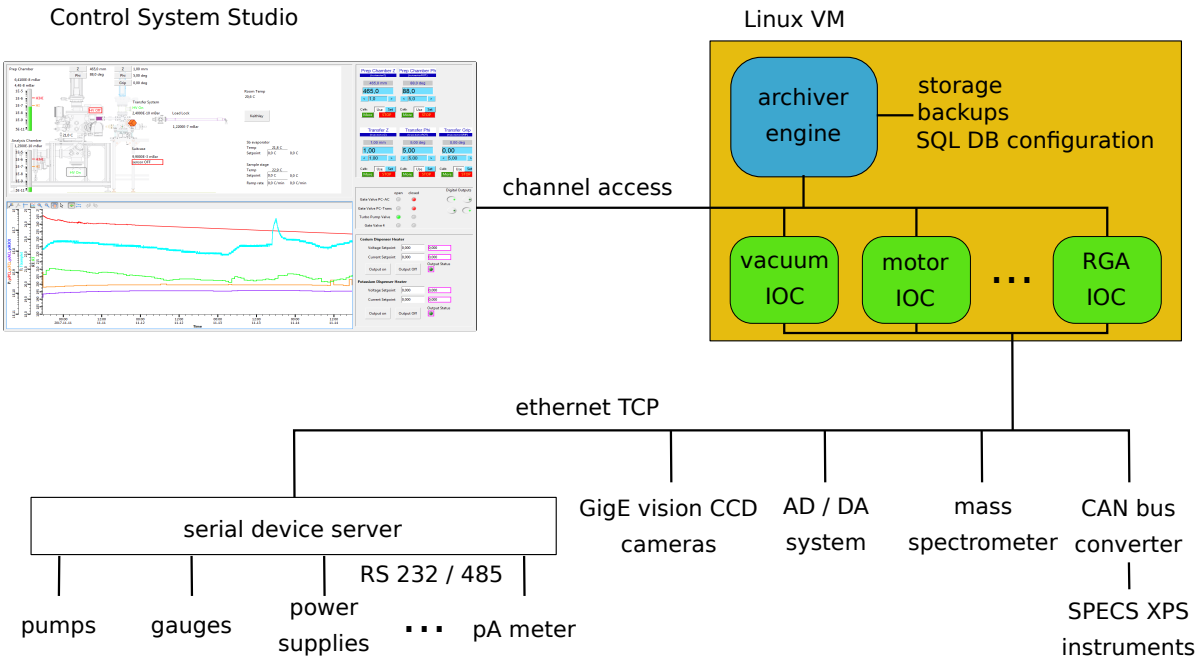

Figure 3.17.: Topography of the software and hardware protocols.

as well as access to the motor controls, setpoints and a plot of archived data. More detailed views are available to display individual instruments and their status. In addition, all devices can be controlled manually from the racks.

Most devices are controlled via RS 232 direct links or a RS 485 bus system. These serial links are aggregated to a serial device server (Moxa nPort 6650-16) which exposes them as TCP ports over ethernet to the software control system. Other devices like CCD cameras that obey the GigE vision specifications or the CAN bus adapter that controls the XPS equipment are connected via a local ethernet switch. The control system for the photocathode lab is an island solution and not integrated in the BESSY architecture. This option was chosen in order to remain flexible during the setup of the lab but should integration become desired it should be a rather simple process due to the similarity of the systems. The topography of software protocols and hardware links is sketched in Fig. 3.17.

To facilitate switching and maintenance of separate components, the software IOCs are implemented in several similar programs. The IOCs are registered as system services and thus started and stopped automatically with the VM. Weekly and monthly backups of the archived data are taken and the configuration files for the IOCs and operator interfaces are kept in a subversion repository.

4. Growth of Alkali Antimonide Photocathodes

The stable alkali antimonide compounds have the general formula A_3Sb, where A is an alkali metal atom and in this work either Cs or K. The binary compound K_3Sb exists in a hexagonal and a cubic phase [46] while Cs_3Sb and the ternary compounds CsK_2Sb and Cs_2KSb are always cubic in the face-centered cubic lattice (space group no. 225) [90]. The growth of photosensitive thin films is performed in UHV, at slightly elevated temperatures on a range of substrates. While cathodes for accelerators are commonly grown on metallic or single-crystal Si substrates, the commercial application in photo-multiplier tubes requires the growth on glass, quartz or sapphire windows which are typically coated with thin metallic interlayer (Pt) to mitigate electrical charging of the layer. During growth the material is evaporated and condenses on the substrate in a physical or chemical vapor deposition process (PVD/CVD). Antimony is evaporated by sublimation, either from pure material in an effusion cell or from PtSb alloyed beads that are fused to a tungsten heating wire [45]. The alkali metals are highly reactive and thus commonly liberated from alkali dispensers, which are commercially available. The evaporation from pure elemental effusion cells is practiced in some laboratories but mostly avoided due to the safety hazards imposed. See also section 3.1 for the evaporation setup used in this work.

Recent work investigates the crystal structure and crystallization dynamics during growth of the Cs-K-Sb compounds. It was shown that the thin films are polycrystalline and undergo multiple phase transitions from amorphous or polycrystalline Sb to polycrystalline K_3Sb (which can be hexagonal or cubic) and finally to polycrystalline CsK_2Sb during the sequential growth procedure [91–93]. The surface roughness depends strongly on the growth mechanism and increases with every phase transition [94, 95].

In the current configuration K and Cs can be evaporated separately or simultaneously onto an Sb film which can be deposited in the same chamber. The first option results in a three step procedure in which an Sb layer is formed on the substrate, then allowed to react with potassium, and finally the K-Sb interlayer is allowed to react with cesium. This procedure is termed the "traditional, sequential growth" procedure and was employed for the samples P006 and P007. The latter option is similar to begin with; an initial Sb layer is deposited and then allowed to react with both alkali metals, K and Cs, at the same time. This procedure is therefore a two step process and termed the "alkali metal co-evaporation" technique, and was used for the remaining samples P009, P013, P014, P015, P016 and G002. All other parameters are kept equal,

to the extent possible, if not noted otherwise. In particular the substrate temperature during deposition, deposition rates and partial pressures of residual gas species are constant. The initial Sb film thickness is varied between 10 and 30 nm as discussed below. For both deposition techniques the sample is formed by diffusion of alkalis into the Sb film and the subsequent recrystallization into an alkali antimonide structure. The process is dominated by the diffusion of alkalis into the material while sufficient alkali metal vapor pressure must be supplied on the surface. Thus the reading of, e.g., a quartz microbalance (QMB) cannot give reliable information on the total film thickness, rather relative information on the rate of metal supplied. Typically the final film thickness is about 5 times the initial Sb film thickness [95].

Before preparation all sources are carefully degassed and deposition rates are determined. Based on the experience gained in this work and measurements presented in [96], it is necessary to reach a total residual gas pressure below $5 \cdot 10^{-9}$ mbar and a water partial pressure below $5 \cdot 10^{-10}$ mbar during operation of all sources, because too high partial pressures of reactive species (H_2O, CO_2, and O_2) will poison the sample, prevent crystallization and reduce the performance of the photocathode.

For the deposition of K and Cs, a heating current of 6 A was applied to each dispenser. During the deposition the partial pressures were monitored with a quadrupole mass spectrometer (Pfeiffer QMA200M). For the sample preparation in both processes discussed below, the total pressure was dominated by the Hydrogen partial pressure contribution; the water vapor partial pressure never exceeded $5 \cdot 10^{-10}$ mbar, and all other species were lower.

The growth process is observed by measuring the photocurrent extracted from the sample. For this purpose, a bias voltage of 300 V is applied between the pick-up anode and the sample, which is constantly illuminated with green light at 2.33 eV (532 nm; frequency doubled Nd:YAG laser) or 2.4 eV (515 nm; monochromatic white light source).

As a reference, the relevant process parameters for the two deposition schemes are listed in Table 4.1. The Sb crucible temperature is PID controlled to an accuracy of 50 mK and the value of 411°C refers to the deposition rate of 0.2Å/ s. When no process is running and after bakeout and degasing of filaments and sources, the base pressure of the system is reached and should be below the values quoted below. The values for total pressure and H_2O vapor pressure should not be exceeded during the deposition steps.

In the following sections, the preparation of metallic substrates prior to the photocathode deposition will be discussed, followed by a detailed description of the two deposition techniques employed in this work. The figures 4.5 and 4.8 show the main deposition parameters of the two processes in an idealized manner, each followed by an exemplary preparation protocol for one photocathode sample grown by the respective method.

Parameter	**Value**	**Unit**	Note
Sb film thickness	30	nm	
total film thickness	150	nm	estimated
substrate temperature	120	°C	PID controlled
Sb crucible temperature	411	°C	PID controlled
Sb deposition rate	0.20	Å/ s	
K dispenser voltage	< 3.0	V	not regulated
K dispenser current	13	A	stay below 14 A
Cs dispenser voltage	< 3.0	V	not regulated
Cs dispenser current	12	A	stay below 14 A
vacuum total pressure	$\ll 1 \cdot 10^{-8}$	mbar	base pressure $< 5 \cdot 10^{-10}$ mbar
H_2O vapor pressure	$< 5 \cdot 10^{-9}$	mbar	base pressure $< 5 \cdot 10^{-11}$ mbar

Table 4.1.: Reference of typical parameters during the deposition process. The parameters are equal for both schemes. The currents listed are for two dispensers in a parallel cirquit.

4.1. Preparation of Substrates

Setting the stage for a successful deposition of photocathodes, the preparation of the substrate is an important step. A suitable substrate must be electrically conducting in order to sustain the photocurrent drawn during operation, its surface must be polished to an rms surface roughness of $R_q < 10\,\text{nm}$ so as not to disturb the electron beam emittance, and a very high purity of the material must be ensured. Contamination of the material with oxides, organic and inorganic residues, or particles will lead to several problems. For one, chemical impurities will react with the photocathode material and reduce its quality and lifetime or impede crystallization.

In this work, metal substrates are investigated as the cathodes are operated in reflecting mode and metals fulfil the conditions made above: high purity materials are available and metal single crystals can be polished to an rms roughness of a few nm. Polycrystalline samples can be polished to $R_q \approx 10\,\text{nm}$. Appropriate cleaning procedures had to be developed in order to achieve the required ultra high purity. Although successful fabrication of alkali antimonide photocathodes has been reported on stainless steel (AISI 304) and copper substrates [97, 98], there is also evidence obtained from Auger depth profiling [96, 99] that diffusion between the Sb layer and the

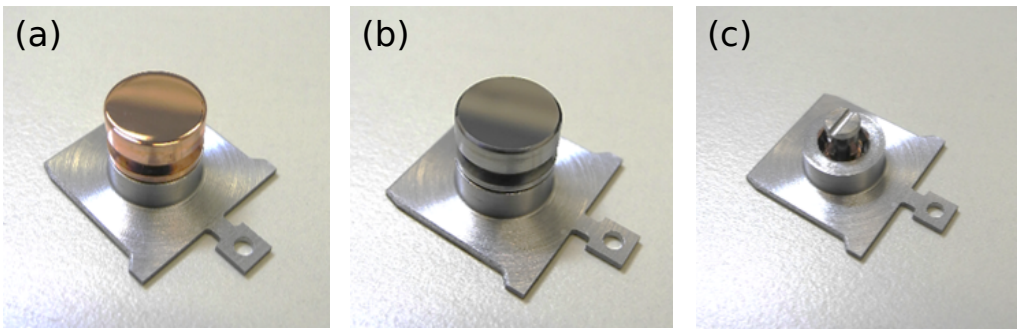

Figure 4.1.: Copper (a) and molybdenum (b) plug substrate design with polished surface and rounded edge. Both are shown on the flag style sample holder (c) which is compatible with common deposition and analysis systems and can be carried in the transfer systems and vacuum suitcase. Reprinted from [55].

substrate takes place on a scale of several nm. For Mo substrates a sharp transition between the deposited film and the substrate was observed.

The early samples discussed in this work (up to P006) were deposited on polished Mo sheets which were clamped to a standard flag-style sample holder (not shown). The later samples were all prepared on plug substrates which are compatible to the photocathode transfer chain as detailed in chapter 7. Plug substrates made from high purity Copper and Molybdenum are shown in Fig. 4.1 and can be placed on the modified sample holder which holds them in place by means of a crown-shaped spring made of Copper-Beryllium alloy. The procedures to grow photosensitive Cs-K-Sb photocathodes were optimized within the scope of this work from the standard procedures found in the literature to accommodate the use of the photoinjector plug substrates and are described in the following two sections.

Single Crystal Substrates

Two substrates were manufactured at Mateck from single crystal samples, one from Cu in (001) orientation and one from Mo in (100) orientation. The plug geometry was formed from the bulk samples by means of spark erosion and the top and bottom surface were polished to $R_q = 1\,\text{nm}$. While the surface of such single crystals is nearly perfect, the rounded edge at the top and the cylindical shape around the plug show clear remnants on the spark erosion process (see Fig. 4.2) which are unacceptable for the use in a photoinjector. The protrusions and additional roughness introduced by this process might lead to increased field emission.

Metal single crystals are much softer than poly-crystalline samples and cannot be worked in a typical milling or turning machine. Preference has thus been given to poly-crystalline substrates for the purpose of this project.

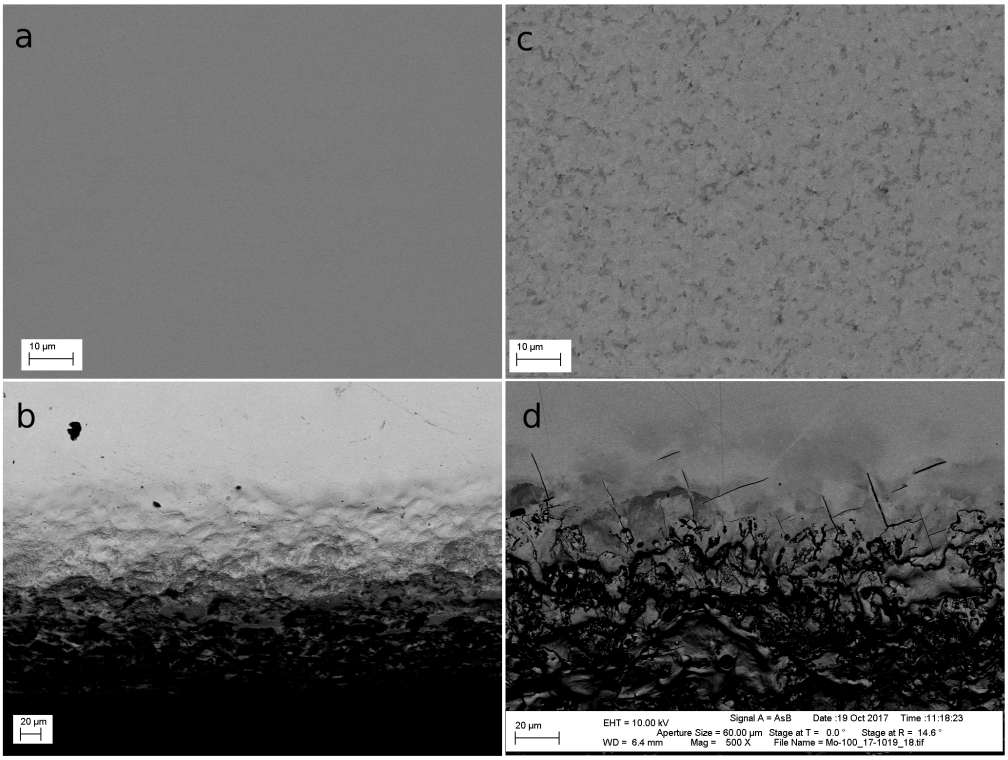

Figure 4.2.: SEM micrographs of a copper (a and b) and molybdenum (c and d) single crystal. The upper panels (a and c) are taken at central positions on the plug surface while the lower panels (b and d) are taken at the rounded edge.

Roughness Measurements

The surface quality and roughness can be assessed using white light interferometry (WLI) and atomic force microscopy (AFM). Both methods yield the surface morphology and can resolve nm sized features. They are especially useful to determine the surface roughness R_a and R_q on a microscopic scale. R_a is the arithmetic mean deviation of a measured surface profile from the center line and R_q is the root-mean-square deviation. The chemical composition of the surface and of residues or particulates found on the surface can be determined using scanning electron microscopy (SEM) when it is combined with energy dispersive X-ray spectroscopy (EDX). However, these methods scan over a microscopic area not larger than 100x100 μm^2. For substrates with intended use in the photoinjector it is therefore essential to assure a defect free surface and rim of the plug in an optical microscope over the entire area.

Poly-crystalline Mo substrates were polished to a surface roughness of approximately R_q = 10 nm. An increase in the surface roughness of less than 5 nm rms due to the sputter etch process discussed below was observed on a witness sample. In contrast, a first batch of copper substrates was only polished to R_q = 100 nm by hand. The wet

etch step with citric acid applied to the copper substrates resulted in a slight reduction of the surface roughness. A superior process to the hand polishing is offered by the company LT Ultra where Copper (but not Mo) plugs can be worked by Diamond turning to a surface roughness of $R_q = 8\,\text{nm}$ with a shape tolerance within $5\,\mu\text{m}$ and a new batch of copper substrates was obtained with such a surface finish.

Cleaning

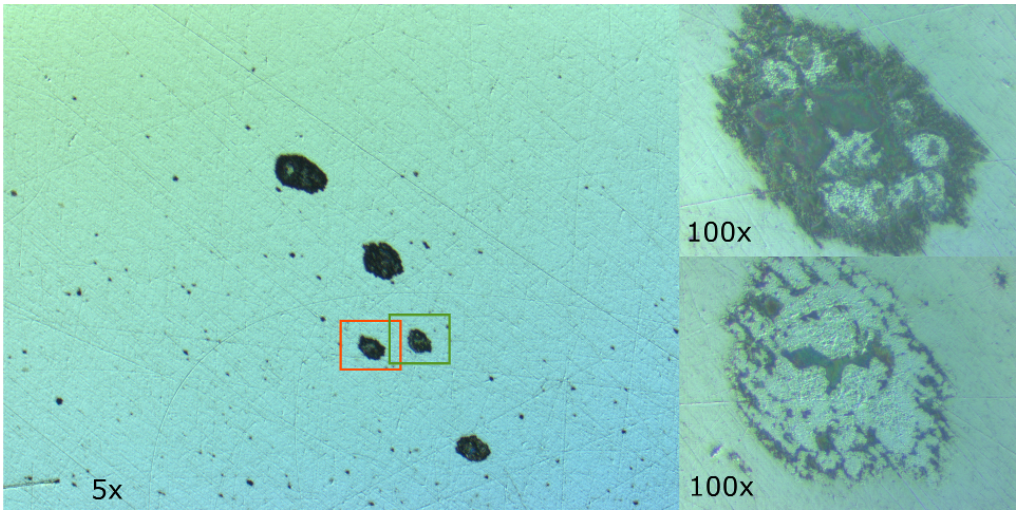

Figure 4.3.: Optical microscope images of a Mo plug substrate. The large black spots consist of Mo oxides and Copper impurities. Areas marked with rectangles are shown enlarged after 1 min of dry ice cleaning. Images are taken in C-DIC mode.

All machined parts, even if made from high purity material, will have significant amounts of impurities and unwanted particles on the surfaces. In order to reach a high surface purity and particle-free quality, each substrate has to undergo several cleaning steps. Dry ice cleaning (i.e. pointing a jet of solid CO_2 flakes at the part) has been shown to reduce the particle count on the surface as well as remove grease and coarse oxide spots. It is therefore applied before the parts and substrates are brought into the clean room.

Organic compounds such as remnants of the cooling and lubrication liquid from the machining process or from handling are dissolved in an ultrasonic bath with the solvents isopropyl alcohol and acetone. The substrates are then blown dry using dry, filtered, and ionized nitrogen and can then be stored in a clean plastic carrier for transport or, under the local clean room environment at the load-lock, inserted into UHV.

Finally, the native oxide and trace impurities are removed in UHV by baking the sample and bombardment with Ar^+ ions. Copper samples have been baked at 200°C

and Mo samples at 450 to 500°C The effect of these final steps is illustrated in Fig. 4.1 for the example of a Copper surface. The XP spectra after each cleaning step show a clear reduction of the peaks due to C and O impurities. The spectra were analyzed to yield the residual impurities concentrations in table 7.1.

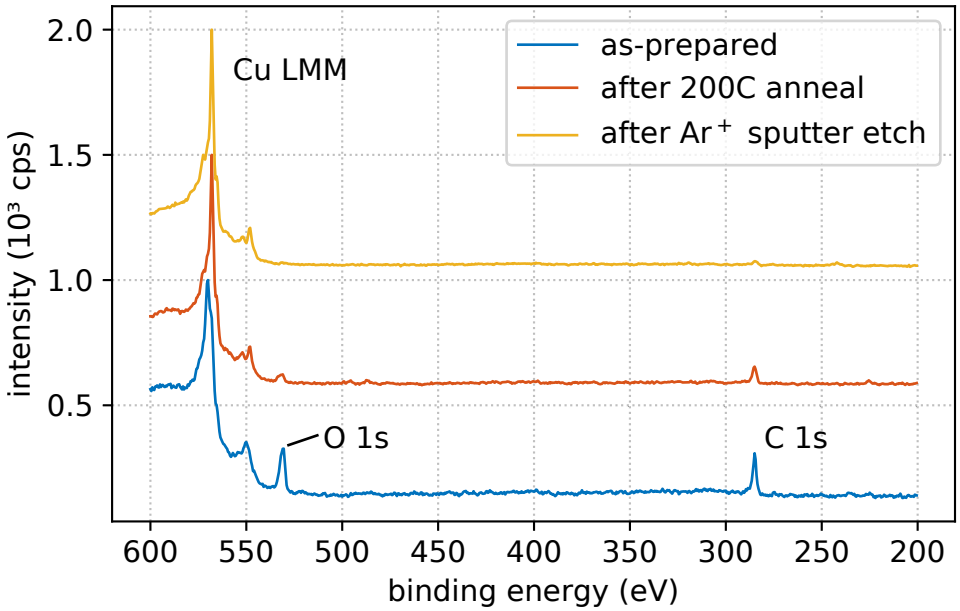

Figure 4.4.: UHV cleaning procedure of a copper substrate showing the XP spectra (Al Kα) including the Cu LMM Auger transitions (> 540 eV), O 1s (531 eV), C 1s (285 eV) peaks taken after each preparation step. Reprinted from [100].

4.2. Sequential Deposition

A high quantum efficiency (QE > 4 %) of sequentially deposited cathodes could be demonstrated for the following growth parameters [47, 101]: deposition of a 10 nm thick Sb film at 0.2 Å/s and 100°C substrate temperature, K deposition at 0.01 Å/s and 100°C until the photo-current plateaus, Cs deposition at 0.03 Å/s and 90°C until the photo-current plateaus. Note that the alkali rates are the maximum rates at the specified operation current. Usually each alkali deposition takes about 2 h.

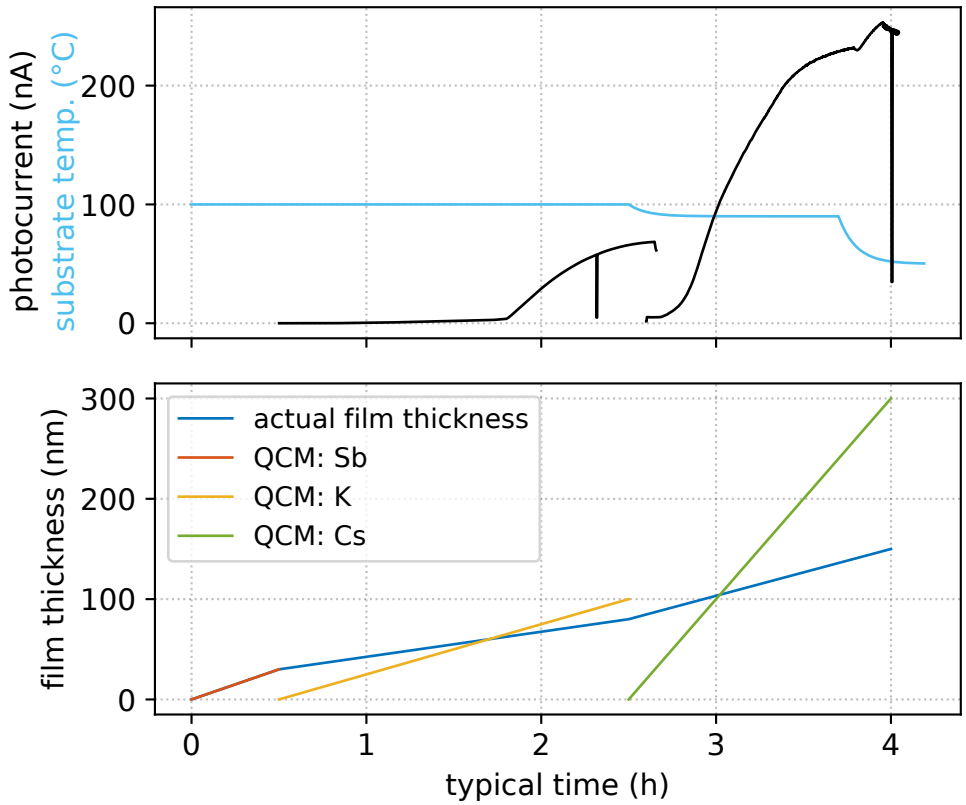

Figure 4.5.: Idealized growth scheme in the sequential growth procedure. The individual thickness values displayed for Sb, K, and Cs are the raw reading one might observe on a quartz crystal microbalance (QCM) but the actual film thickness depends on the temperature dependent rate of alkali diffusion into the bulk, not only on the deposition rate onto the surface.

A schematic representation of the process parameters relevant during the deposition is displayed in Fig. 4.5. The upper panel displays the substrate temperature which is regulated by a PID loop and set to specific temperatures during the different deposition steps. The photocurrent obtained from illumination at 532 nm is measured continuously during the deposition and provides the primary feedback about the progress of the reaction. Typical is the long duration in the beginning of the K depo-

sition step where a low photocurrent is observed, which results from the amorphous structure of the film as K diffuses into the Sb film and dissolves the lattice. A sudden increase corresponds to the onset of crystallization into a K_3Sb lattice. Such behavior was observed by *in-situ*, time-resolved XRD during the growth as presented in [92]. The photocurrent response during the Cs deposition is much more prompt and leads to the final QE value when a plateau in the measured values is observed. During both alkali deposition steps, also the plateau is used as an indicator to terminate the deposition.

A quartz crystal microbalance is used to determine the deposition rate of the Sb source prior to deposition. Note, however, that the surface of such a balance is not prepared in the same way as the deposition substrate and the temperature is not controlled. Thus, the deposition rate and total thickness reading obtained for the volatile alkali metals often oscillates, and cannot be used as a reliable measurement of the actual rate. At the same time, as mentioned above, the thickness of the photocathode film is not solely defined by the amount of alkali vapor generated and deposited but much more critically determined by the rate of diffusion of the alkali atoms into the film while sufficient vapor pressure is maintained at the surface. The final thickness after full conversion from Sb to Cs-K-Sb is a factor of 5 larger than the initial Sb film thickness.

Protocol of the Preparation of P006

P006 is a Cs-K-Sb sample prepared on a polished Mo sheet, with a QE of 4.8% at 532 nm grown by sequential deposition.

Before the preparation of the sample, the chamber was vented to mount new sources, baked, and had settled to a base pressure of $8 \cdot 10^{-10}$ mbar. Three K and two Cs dispensers were mounted in parallel. The K and Cs dispensers were degassed at 12 and 8 A respectively.

The Mo sheet (polycristalline, 99.95% purity, "Mo_005") was acquired from Goodfellow and polished to mirror finish by Pilz Optics. Before preparation the substrate was rinsed in isopropyl alcohol and blown dry with filtered N_2. After transfer into UHV via a load-lock the sample was annealed in several steps at up to 580°C for 60 minutes and sputter etched with Ar^+ ions at 3 keV for 30 minutes to remove any residual surface contamination and the oxide layer.

The preparation procedure of the Cs-K-Sb film was as follows: at a substrate temperature of 100°C, a thin Sb film is deposited by vapor deposition on the substrate. Sb is deposited at a rate of 0.2 Å/s until a nominal thickness of 10 nm is reached. The Sb film is then exposed to K vapor that is generated from the chromate reduction reaction in an alkali dispenser (see above). During the K deposition, monochromatic light of 532 nm wavelength from a solid state laser is directed onto the sample and the photocurrent is measured continuously using a biased pickup anode. The K dispenser

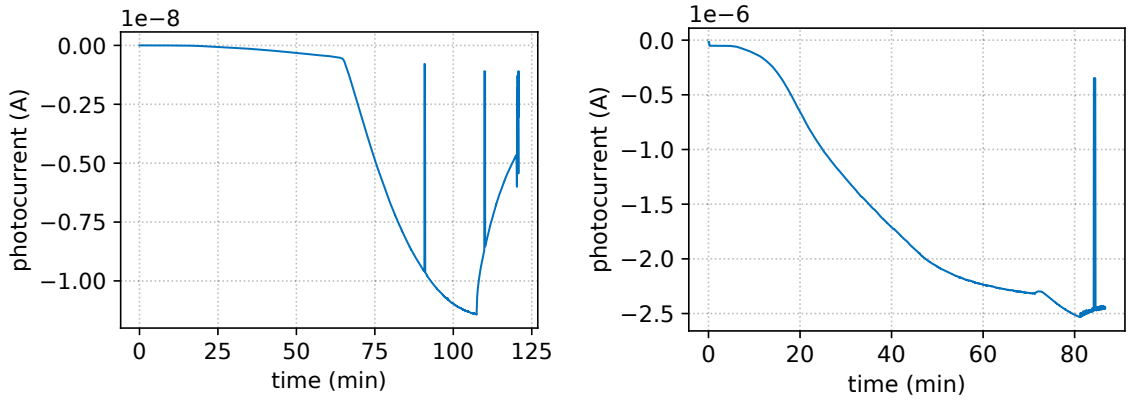

Figure 4.6.: Photocurrent collected by the biased anode during the reaction with K (left) and Cs (right). The short occasions where near zero current was measured (spikes) are due to a blocked light path in order to estimate the current that does not originate from photoemission (dark current).

current was increased step-wise from 18 A to 22.5 A during the K deposition over a time of 105 min, until the photocurrent plateaued.

In a similar manner, the film was subsequently exposed to Cs vapor to allow the reaction to Cs-K-Sb. Cs was deposited from two pairs of sources (one after another), while the current was gradually increased up to 15 A. The substrate temperature was held constant at 100°C. Cs was evaporated until a plateau in the photocurrent is observed. The photocurrent evolution during Cs deposition is shown in Fig. 4.6.

During the evaporation steps the chamber pressure rises to $2 \cdot 10^{-9}$ mbar when the Sb evaporator is active and $1 \cdot 10^{-8}$ mbar when the K or Cs dispenser were active. A peak water pressure of $3.5 \cdot 10^{-9}$ mbar was recorded.

After every preparation step, i.e. after substrate cleaning, Sb deposition, and after the reaction with K and Cs the sample was transferred to the analysis chamber and XPS spectra were acquired. Each time, a survey spectrum was taken to ensure the purity of the substrate and deposited material and region spectra of Sb 3d, K 2p, and Cs 3d were taken which can later be used for the analysis of the reaction and aging processes as well as to determine the stoichiometry of the film. Figure 4.7 shows a compilation of the survey spectra taken during the growth of the sample. The spectrum of the substrate (not shown) revealed no C or O contamination within the resolution of the measurement. The Sb spectrum shows no impurities. The K-Sb spectrum reveals prominent features of both Sb and K, and again no O 1s peak within the Sb 3d region. Similarly, after the reaction with Cs, all three species Sb, K, and Cs are found and again no O contamination. The final QE was determined as 4.8% at 532 nm.

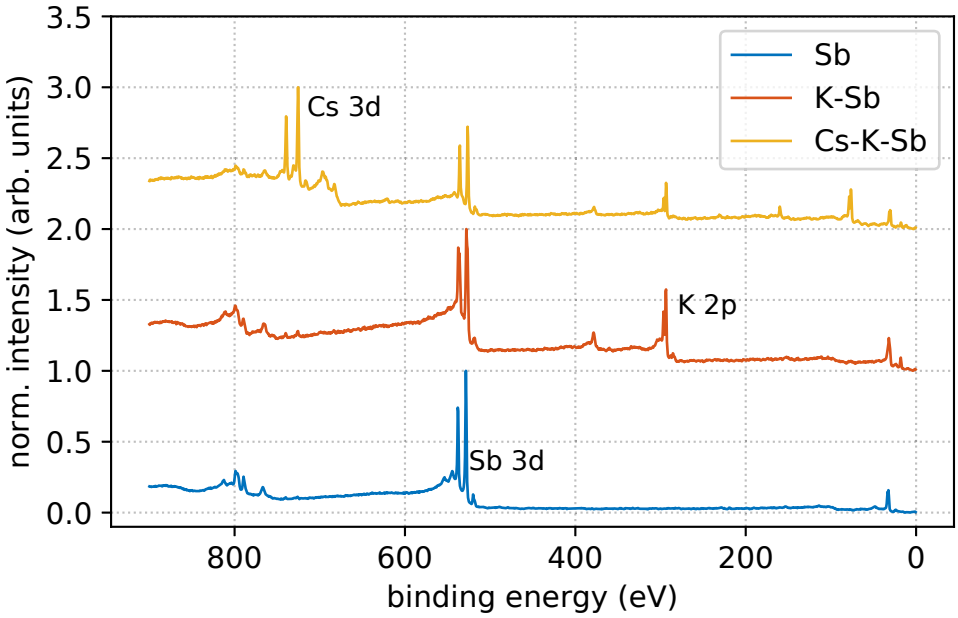

Figure 4.7.: XPS survey spectra of the individual films during growth of sample P006.

4.3. Alkali Co-Deposition

The co-evaporation scheme has been developed as a means to overcome the issues with reproducibility inherent to the sequential evaporation procedure. As noted above, the success of the Cs step in the sequential method depends strongly on the phase (cubic or hexagonal) of the K_3Sb intermediate layer. Thus the overall result depends on external growth parameters (substrate temperature, partial pressures, deposition rate) and even if these are ideal and constant the result might not be satisfactory due to the slow reaction of hexagonal K_3Sb with Cs.

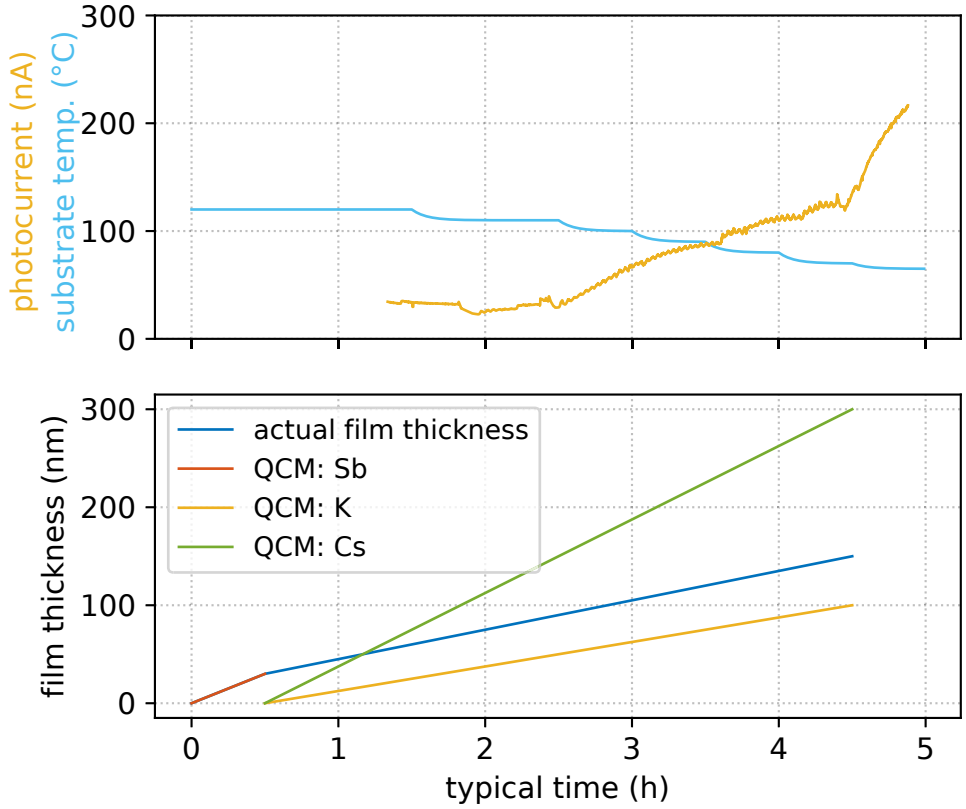

Figure 4.8.: Idealized growth scheme in the co-evaporation growth procedure.

Similar to the description of the sequential procedure above, a scheme of the co-evaporation technique is shown in Fig. 4.8. Instead of trying to selectively grow cubic K_3Sb and convert it to CsK_2Sb, the goal in the alkali co-evaporation procedure is to allow K and Cs to diffuse simultaneously into the film and reach a single phase transition from crystalline or amorphous Sb to Cs-K-Sb. For that purpose, the deposition starts, similar to the sequential procedure, with the deposition of 10 to 30 nm Sb by physical vapour deposition. The temperature of the sample stage is set to 120°C and Sb is evaporated from pure beads in the effusion cell at a rate of 0.2Å/s. The rate is determined by means of a quartz crystal microbalance and the required crucible

temperature is typically 411°C. An aperture is placed at about 1 mm distance to the sample and restricts the deposition to a circular area of 6 mm diameter. The thickness of the Sb film is determined by the duration of the deposition and typically amounts to 1500 s · 0.2Å/s = 30 nm. In a second step, the Sb film is exposed to K and Cs vapor generated by alkali dispenser sources as described above. The dispensers are mounted in pairs, at an angle of 25°to the sample surface. No aperture is used as the overlap of the evaporation cones of the sources was not satisfactory through the small bore. A larger bore aperture might be used that exposes the full plug surface but covers the mantle face of the plug. The dispensers are heated directly by passing a current through the boat. The deposition rate cannot be determined reliably by a quartz balance but the readings obtained varied between 0.01 Å/s and 0.3 Å/s for heating currents between 5 A and 7 A per source.

Protocol of the Preparation of P013

P013 is a Cs-K-Sb sample prepared on a polished Mo sheet, with a QE of 7.3% and 5.6% at 515 nm and 532 nm, respectively, grown by co-evaporation of K and Cs onto the Sb film. Figure 4.9 presents the observed photocurrent evolution during the alkali deposition.

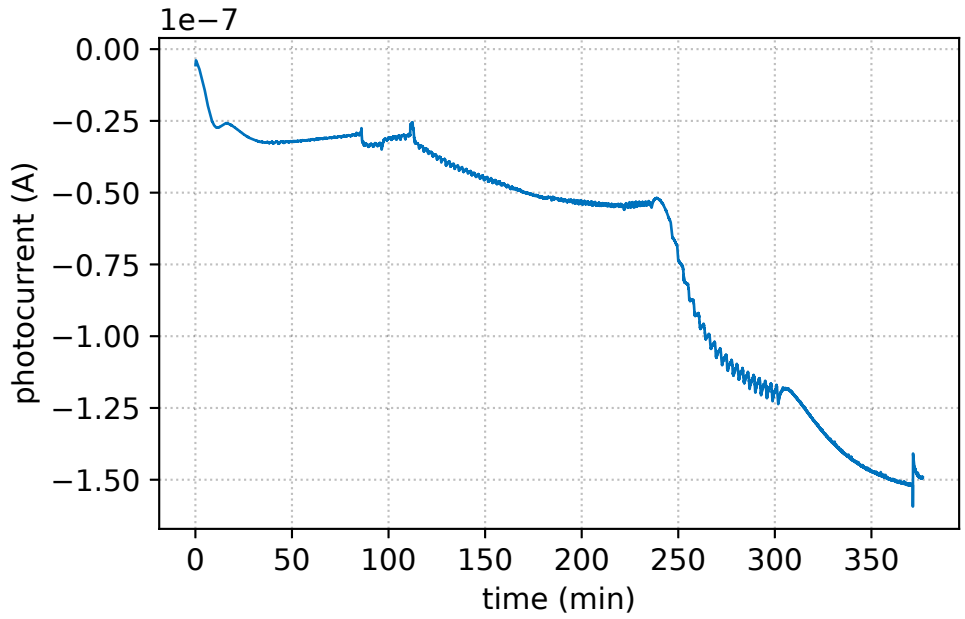

Figure 4.9.: Photocurrent at 532 nm during the reaction with K and Cs. The small oscillations in the measured photocurrent are due to variations in the PID loop that controls the substrate temperature.

The Mo plug (polycristalline, 99.95% purity, "Mo_010") was turned and milled in the HZB workshop and polished to mirror finish by Pilz Optics. Before preparation the substrate was cleaned in an ultrasonic bath with pure water and detergent, then rinsed in pure water and isopropyl alcohol and blown dry with filtered N_2. After transfer into UHV via a load-lock the sample was annealed 450°C for 60 minutes and sputter etched with Ar^+ ions at 3 keV for 20 minutes.

During the evaporation the chamber pressure rises to $6.6 \cdot 10^{-9}$ mbar when the Sb evaporator is active and $9 \cdot 10^{-9}$ mbar when the K and Cs dispenser were active. A peak water pressure of $4 \cdot 10^{-9}$ mbar was recorded.

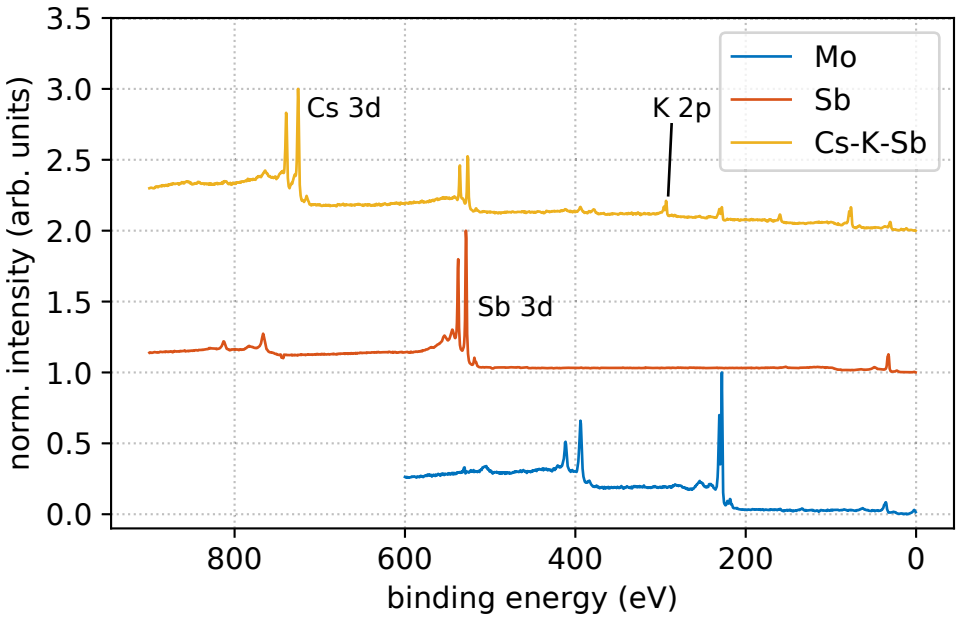

Figure 4.10.: XPS survey spectra after each deposition step of P013.

The same XPS analysis was performed as discussed for the sequential growth of P006, i.e. survey spectra and detailed region scans of the Cs 3d, K 2p and Sb 3d transitions were taken after each deposition step. Figure 4.10 shows a compilation of survey spectra taken during the growth of the sample. The spectrum of the substrate reveals no C or O contamination. Refer to the following chapter for the analysis of the stoichiometry of this sample. The Sb spectrum shows a strong Sb 3d peak and no impurities. Similarly, after the reaction with K and Cs, all three species Sb, K, and Cs show prominent transitions and again no O contamination. The final QE was determined as 5.6% at 532 nm.

5. Analysis of Cs-K-Sb photocathode samples

Several samples of Cs-K-Sb photocathodes have been prepared in order to gain experience with the deposition and understand the correlations between process parameters, physical quality of the thin films, and the figures of QE and MTE obtained for each sample. Here, the systematic study of the growth procedures discussed above is presented in section 5.1. The chemical analysis by XPS of the two different growth procedures is preformed considering the samples P006 and P007 for the sequential growth and P009 and P013 for the alkali metal co-deposition on Sb. The data acquired from the XPS analysis is then used in section 5.2 to obtain the stoichiometry of the samples and determine its influence on the QE. Furthermore, the behavior of the spectral response when the photocathode is cooled is addressed in section 5.3.

The sections 5.1 and 5.3 have been published previously in [10].

5.1. Sequential and Co-Evaporation

For the discussion of the reaction of the initial Sb film with the alkali metals consider the signal of the Sb 3d transition which is known to be sensitive in terms of peak shifts to the chemical situation (metallic, bound, or oxidized) of the atoms [101, 102]. The behavior of the Sb 3d signal is observed during the reactions and a discussion of the implications on the reaction dynamics that can be derived is presented.

Figure 5.1 shows the Sb 3d region spectra for each preparation step. For all samples a pure Sb layer was grown on polished, pure and clean Mo substrates. No signal from the Mo substrate was discernible after any deposition step.

Figure 5.1(c) and (e) show that after the first step, the Sb $3d_{5/2}$ peak was found at 528.3 eV and the Sb $3d_{3/2}$ at 536.7 eV, corresponding to Sb(0). The next step for P006 and P007 was the K deposition on the Sb-layer as shown in Fig. 5.1(b); for P006 this resulted in a mixed K-Sb phase. The dominant Sb $3d_{5/2}$ peak at 528.0 eV is related to K deposited on Sb, while the second peak with lower intensity at 526.6 eV is indicative of the Sb(3-) state of K_3Sb.

Finally for P006 and P007, Cs was deposited on the K-Sb film reacting to a Cs-K-Sb photocathode (Fig. 5.1(a)). For P006, the Sb(3-) $3d_{5/2}$ peak shifted to 526.3 eV, while the Sb(0) $3d_{5/2}$ disappeared.

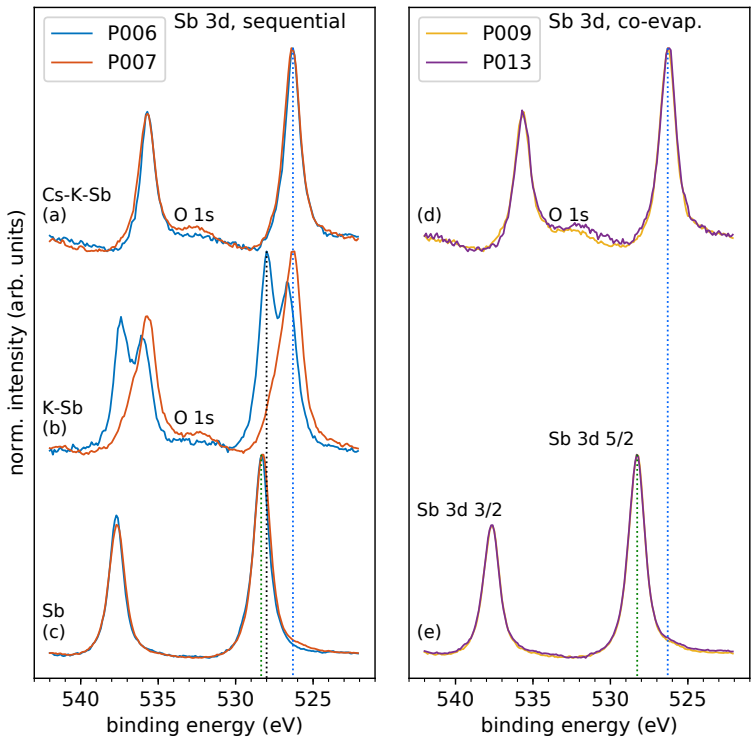

Figure 5.1.: Comparison of the Sb 3d spectra of four samples, two grown sequentially (left) and two by alkali metal co-evaporation (right). In both processes the alkali metals were evaporated on a pure Sb layer (c, e). The Sb 3d spectrum of the K-Sb layer of P006 shows two peaks, indicating that the Sb has not fully reacted with K (b, blue line). The spectra of the Cs-K-Sb layers are identical for all samples (a and d).

The composition of both the intermediate K-Sb layers of P006 and P007 as determined by XPS show a K deficiency with respect to K_3Sb (see Tab. 5.1). Nevertheless, the almost rigid shift of the Sb 3d peak of P007 indicates that most antimony in the probe depth has reacted (peaks at 526.3 eV and 535.6 eV, red line). A shoulder is discernible in the Sb 3d 5/2 peak for P007 which hints at traces of non-reacted Sb. In contrast, the double structure in the Sb 3d peak of P006 indicates the presence of non reacted Sb (peaks at 528.3 eV and 536.7 eV) as well as reacted Sb in the Sb(3-) state. The effect of different levels of reaction will be discussed below. The final Cs-K-Sb photocathode layers of P006, P007, P009 and P0013 have almost identical Sb 3d peak shapes which are fully converted to the Sb(3-) state (Fig. 5.1(a) and (d)).

Figure 5.2 presents the K 2p and Cs 3d spectra of the respective samples. Figure 5.2(c) shows the K 2p spectrum of P006 and P007 after the second step (K-Sb); for P006 the K $2p_{3/2}$ peak is at a binding energy of 293.7 eV and the K $2p_{1/2}$ is at 296.5 eV. The K 2p peaks are shifted by approximately 0.4 eV to lower binding energies after the Cs

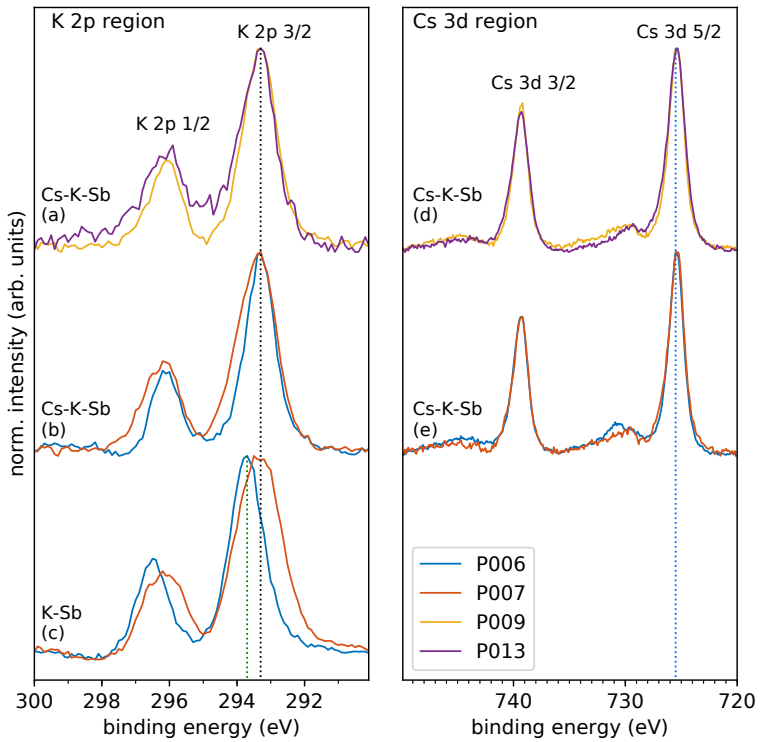

Figure 5.2.: Comparison of the K 2p (left) and Cs 3d (right) spectra of each sample. The color code holds for both panels. Note the shift in the P006 K 2p spectra between the K-Sb and Cs-K-Sb layer (b and c, blue lines). The K 2p and Cs 3d spectra of the Cs-K-Sb layer of the other layers show no difference in terms of binding energy and peak shapes (a and d).

deposition (Fig. 5.2(b)); this is now the same position compared to the K 2p spectra of the other samples. The Cs 3d spectra in Fig. 5.2 are almost identical for all samples. The Cs $3d_{5/2}$ in Cs-K-Sb is at a binding energy of 725.5 eV and the Cs $3d_{3/2}$ at 739.2 eV.

The measured spectra - Cs 3d, K 2p, and Sb 3d - have equal binding energies and peak shapes for the final Cs-K-Sb films of all samples regardless of the slight differences in the stoichiometry. In Fig. 5.1(a) and (d), the Sb 3d spectrum of P007, P009 and P013, a weak O 1s peak is discernible at about 532.6 eV, which might originate from residual gases or from the K and Cs dispensers. It is also observed in the intermediate K-Sb layer of P007 (Fig. 5.2(b)), but no oxygen was observed in the pure Sb layers. The presence of oxygen may be an additional factor contributing to the lower QE values for these samples.

All measured binding energies are in good agreement with a previous XPS study by Schubert *et al.* performed in a different laboratory [101].

The present data suggests, that the full crystallization of a K_3Sb layer, as evidenced in P007, leads to formation of a stable phase prior to the final preparation step. Thus re-crystallization into a Cs_2KSb or CsK_2Sb lattice that incorporates the much larger Cs atoms is energetically unfavorable, leading to the low performance of a sample like P007. It is possible in the sequential technique to grow high QE samples when the intermediate K-Sb phase does not fully react and thus stays more susceptible to diffusion and re-crystallization during the cesiation step, as observed with sample P006. The hypothesis is supported by XRD data presented by Schubert *et al* [93, 103]. The formation of a stable hexagonal K_3Sb phase is witnessed as a last step during the K deposition after formation of the cubic phase. The temperature dependence observed in their data shows that the recrystallization of the hexagonal phase is unfavorable compared to the cubic phase. Co-evaporation of both alkali metals avoids this problem because the formation of the hexagonal phase seems unlikely considering that it develops last in the K deposition of a sequential growth. Here, only a single crystallization into the cubic Cs-K-Sb lattice takes place which is also favorable in terms of surface roughness.

The chemical composition of six photocathodes in total were analyzed based on XPS data. The stoichiometry of the samples in Tab. 5.1 was determined from the relative peak intensity of the Sb 3d, K 2p and Cs 3d peaks taken from survey spectra. The quantification model assumes a homogeneous depth distribution of the atomic concentrations, which have been normalized to Sb. For the sequential growth (P006, P007), the composition of the K-Sb layer is also given. The rest of the photocathodes presented in Tab. 5.1 have been grown in two steps. The quantitative data of P014 and P015 additionally demonstrates the reproducibility of our growth process with respect to high QE. Our data supports the claim that higher stoichiometric content of Cs, e.g. Cs_2KSb, is favorable for a higher QE relative to the CsK_2Sb lattice. This agrees with the theoretical findings by Ettema and de Groot [25].

The thickness of the Sb layer is also presented in Tab. 5.1. High QE samples have been achieved by tuning the initial thickness of the Sb-film. Furthermore a thicker film is known to be correlated to a longer QE lifetime [104].

No further *in-situ* diagnostics are required to perform the growth of CsK_2Sb samples in the alkali metal co-evaporation technique, which might prove as an alternate path next to the ternary co-evaporation where the stoichiometry needs to be monitored during growth by, e.g., X-ray fluorescence measurements [105].

In conclusion from this section, a co-deposition procedure of Cs-K-Sb photocathodes was developed and evaluated. The XPS results of the sequentially grown and the alkali metal co-deposition grown Cs-K-Sb photocathodes are in good agreement, which makes the co-deposition preferable, because the process is more reliable, time efficient and is expected to deliver photocathodes with a lower surface roughness. The data suggests, in agreement with other work, that the main reason for lacking reproducibility in the growth of CsK_2Sb cathodes is the formation of stable K_3Sb

crystallites which are less likely to react. At the same time it as hardly controllable which phase of K-Sb forms during reaction of K with Sb.

Therefore, growth techniques where Cs is introduced earlier into the system, like the alkali co-evaporation presented here or triple evaporation should be favored.

Furthermore, the more recent samples were grown on a Mo plug in the geometry that can be used in the photoinjector, which is an essential step forward towards using a Cs-K-Sb photocathode in the bERLinpro SRF-photoinjector. The results of the co-deposition procedure on a Mo plug are very promising for the development of a reproducible growth procedure delivering high QE and stable Cs-K-Sb photocathodes for photoinjector applications. A comparison of the spectral response of a few selected samples with reference data for the sequential growth procedure is presented in Fig. 5.3.

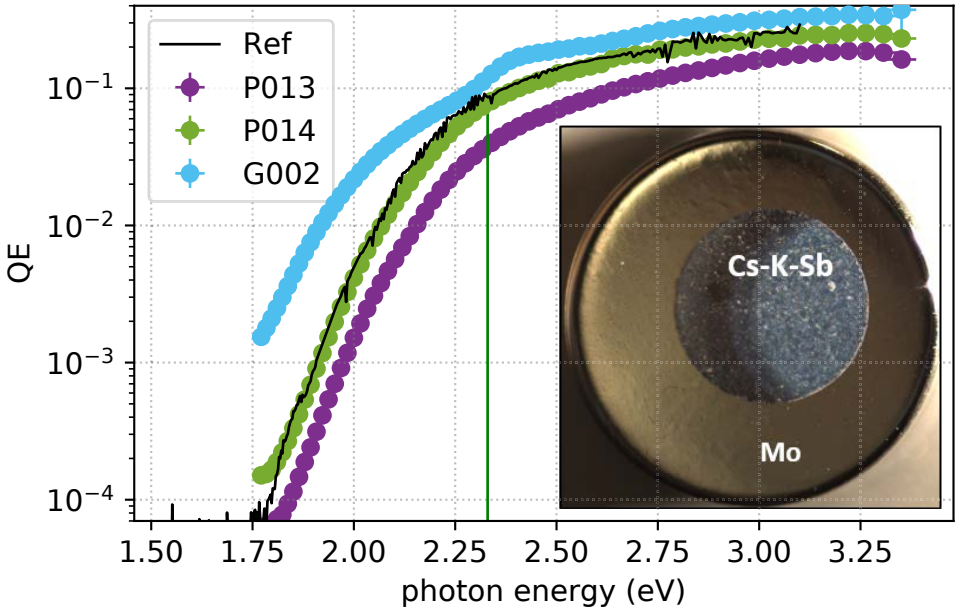

Figure 5.3.: Spectral response data of P013, P014, and G002 after preparation and photograph of sample P014. The green vertical line marks the excitation energy of a 532 nm laser. The reference curve was obtained from ref. [98]

Sample		Sb layer (nm)	Stoichiometry Sb	K	Cs	QE (%)
P006	K-Sb	10	1	2.3		
	Cs-K-Sb		1	1.8	1.4	4.8
P007	K-Sb	10	1	2.7		
	Cs-K-Sb		1	2.4	0.8	1.6
P009	Cs-K-Sb	10	1	1.9	1.4	2.6
P013	Cs-K-Sb	30	1	1.5	2.3	5.6
P014	Cs-K-Sb	30	1	0.5	1.8	7.7
P015	Cs-K-Sb	30	1	1.0	2.3	7.2
P016	Cs-K-Sb	30				3.03

Table 5.1.: Chemical composition, thickness of the initial Sb layer, and final QE of the sequentially and co-deposited samples. The QE is measured at 2.33 eV, as-prepared.

5.2. Stoichiometry of the Samples

As discussed above, the phase diagram of the Cs-K-Sb system allows for different configurations that can be thought of as a parameter range between the stable formations of

$$K_3Sb - CsK_2Sb - Cs_2KSb - Cs_3Sb$$

and real samples will deviate from those ideal stoichiometries as they might consist of polycristalline areas where each grain has an individual stoichiometry, amorphous regions, and might have a defect concentration where vacancies and intercalated atoms create a deviation from the local lattice stoichiometry.

The samples that were investigated here are all Cs-K-Sb samples and the stoichiometric indices are defined as

$$Cs_xK_ySb,$$

where, ideally, $x + y = 3$.

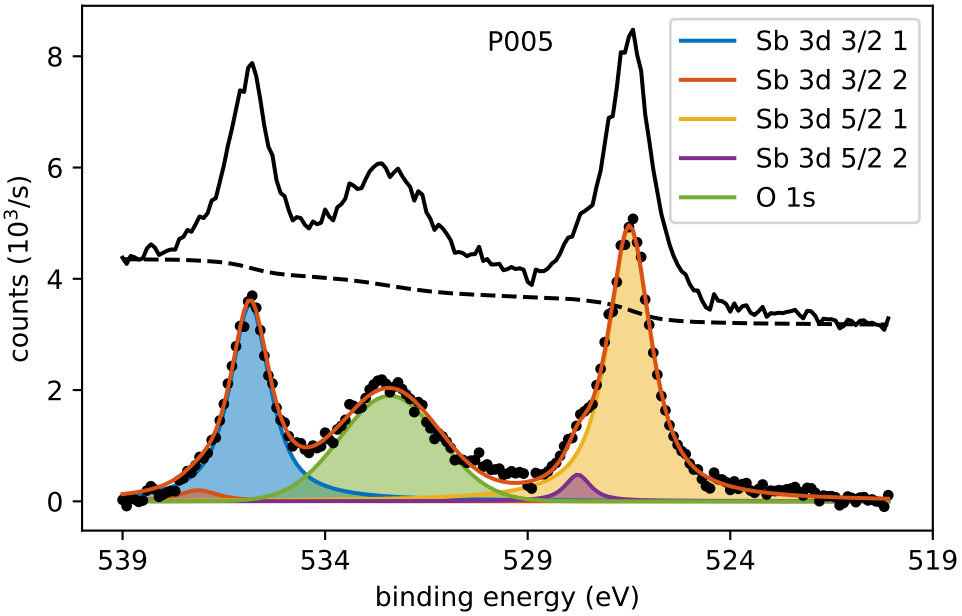

Figure 5.4.: Deconvolution by fitting of synthetic peaks to the Sb 3d and O 1s region. The measured signal and the Shirley background are shown as black lines above the model.

Using the XPS methods described in section 3.3 and the quantitative analysis as described in section 3.3.3, one can obtain the concentration of the atomic species in the sample. The analyzed volume in the XPS measurements stems from a large (millimeter) area of the surface, which will average over a large number of crystal

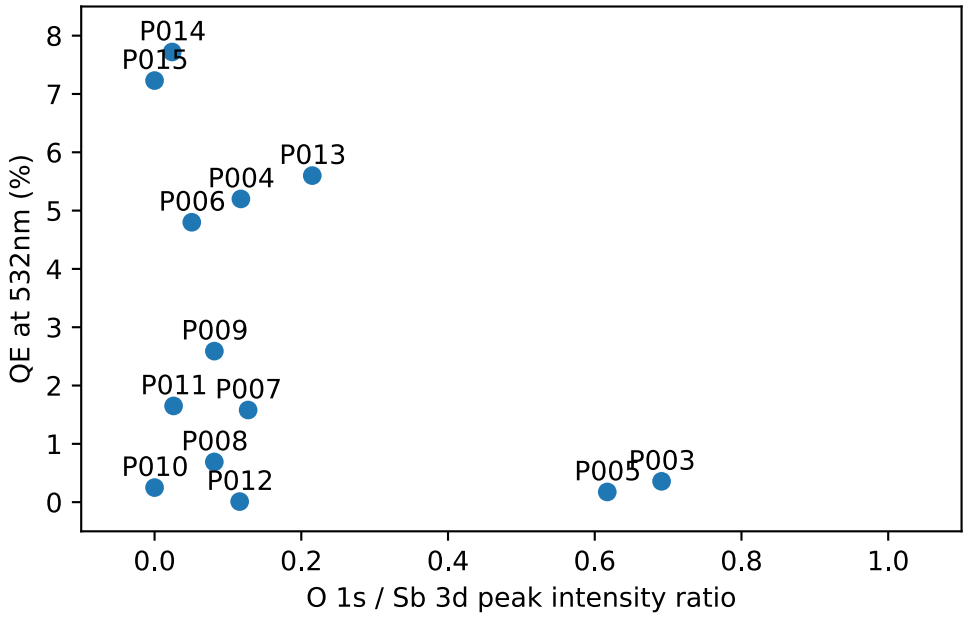

Figure 5.5.: Correlation of QE with the relative oxygen signal.

sites, but from a very shallow depth of a few nanometer into the surface which will emphasize the surface concentration of the atomic species while neglecting any depth distribution. Keeping these constraints in mind, what follows discusses the empiric influence of the stoichiometry (Cs vs. K vs. Sb concentration) and the amount of oxygen contamination on the performance of the samples.

A relative measure of the oxygen contamination of a sample can be obtained from the ratio of the peak intensity of the O 1s and Sb 3d 5/2 peaks. Due to the similar binding energy of the two states, the peaks overlap in the spectrum and must be deconvolved to obtain the individual intensities. The procedure is outlined below an example of the fitted peaks is shown in Fig. 5.4. The antimony 3d and oxygen 1s peaks have their binding energies in a region between 519 and 542 eV and the deconvolution is performed on high-resoultion spectra of that region. Typically, the spectrum contains contributions from two Sb species, one is the Sb^{3-} state where the spin-split $3d_{5/2}$ and $3d_{3/2}$ peaks are found at 526.3 eV and 535.6 eV, the other is remaining Sb in the Sb(0) state with peaks at 528.2 eV and 537.7 eV, respectively. The signal from the O 1s state is centered at 532.5 eV. For the deconvolution, a model was constructed from a sum of four Voigt profiles, each centered at the respective Sb peak positions and a Gaussian profile centered at the oxygen peak. The model was then fitted to the measured spectrum with the peak positions, heights and width as free parameters. The fit was constrained such that the 3:2 intensity ratio and an equal distance between the spin split pairs was retained. The Python LmFit [106] package was used to minimize the difference between the measured signal after a Shirley background subtraction and the modeled spectrum.

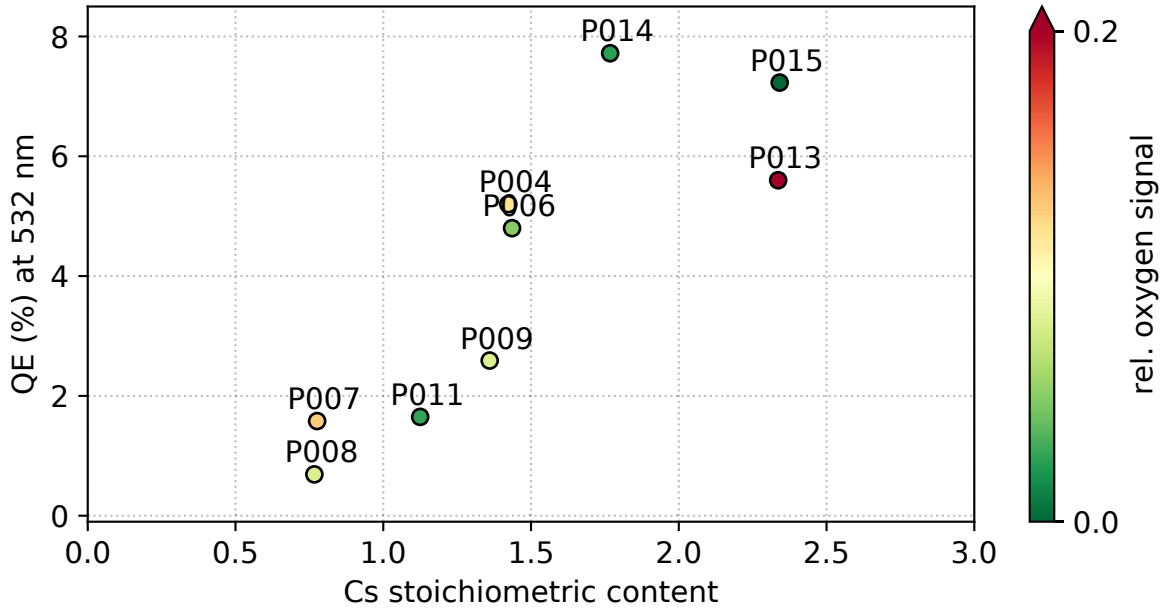

Figure 5.6.: Correlation of QE with Cs stoichiometric content.

Oxygen adsorption on the surface can have two effects on the QE of a sample. For sub-monolayer coverage, a Cs-O dipole layer forms and lowers the work function of the surface, thus increasing the QE [96]. On the other hand, any higher exposure to oxygen leads to segregation of alkali metals and antimony and formation of the respective oxides, effectively destroying the surface [102]. This results in a dramatic decrease of QE.

Due to the counteracting nature of the two effects there is no clear correlation discernible between the relative oxygen signal and QE as shown in Fig. 5.5. Instead, a QE range between 0 and 8% is observed for small oxygen signals where the spread in QE must have a different explanation, and, as expected, no high-QE samples are found with a high oxygen signal. However, the measure of Fig. 5.5 will be used in the color coding of the subsequent figures to illustrate the oxygen signal obtained for each sample. Since the low QE of the samples P003 and P005 can be attributed to the high oxygen contamination, they have been excluded from the further analysis.

The correlation of QE with Cs and K stoichiometric content (x and y) is shown in Figures 5.6 and 5.7. There is no clustering of the samples around either $x = 1, y = 2$ or $x = 2, y = 1$ as one would expect from the nominal chemical formulas, but the total alkali concentration clusters around $x + y \approx 3$. This can be attributed to the polycrystalline nature of the films where grains of the different species mentioned above exist. The analytical stoichiometry, again, is a mean value that averages over a surface area of several mm^2. Clearly, the QE correlates with the average Cs content and high quantum efficiencies of up to 8% are observed for samples with $x \approx 2$.

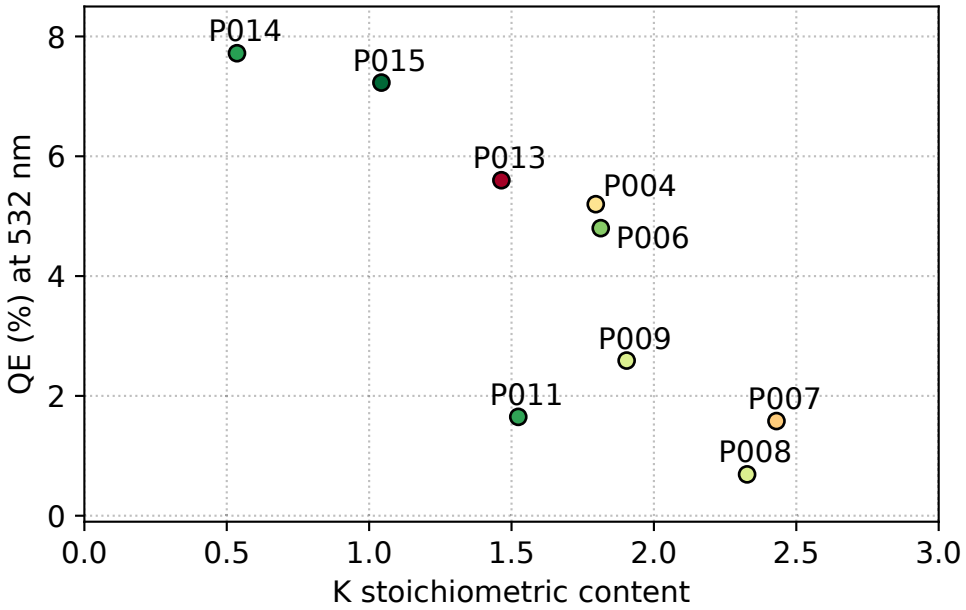

Figure 5.7.: Correlation of QE with K stoichiometric content.

At the same time, the opposite trend is discernible for the average K concentration y, where the high-QE samples are located near $y \approx 1$. As becomes evident in Fig. 5.8, the samples do not diverge strongly from the $x + y = 3$ line indicating a good overall crystallinity, while the varying stoichiometry of individual grains contributes to deviations from the nominal Cs_2KSb or CsK_2Sb values.

In summary, one may conclude that the growth of Cs_2KSb instead of CsK_2Sb is desirable in terms of quantum efficiency at 532 nm and a very similar result is obtained for the same analysis at 515 nm. However, other operation parameters as discussed in chapter 2 might lead to a different preference and should be analyzed in a similar fashion. One could imagine, for example, that a higher content of volatile Cs in Cs_2KSb results in a lower acceptable operational temperature or reduced lifetime.

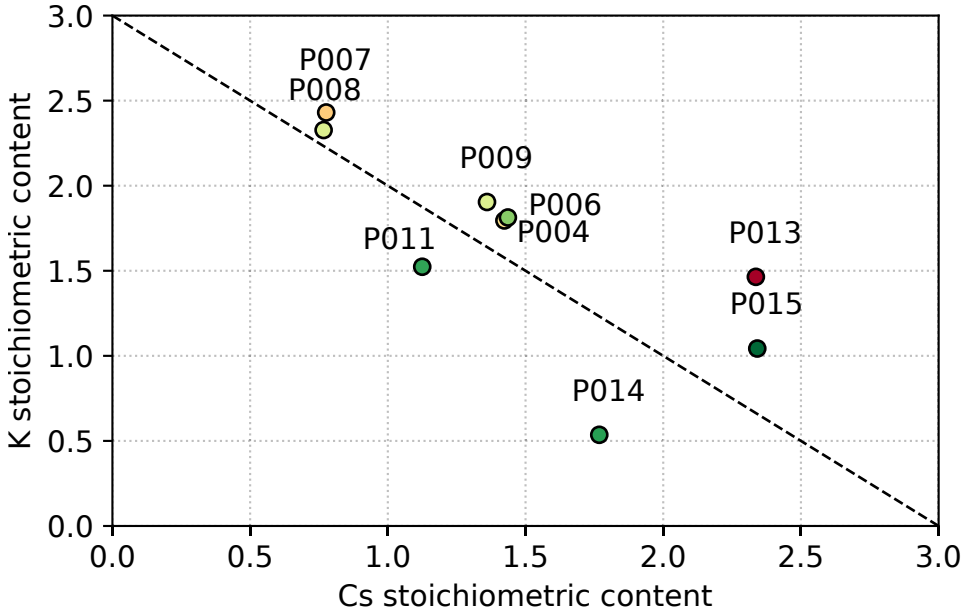

Figure 5.8.: Scattering of the individual alkali constituents. The black dashed line represents the $x + y = 3$ case.

5.3. Temperature Dependence of the Spectral Response

In the case of the SRF photoinjector for bERLinPro, the photocathodes will be operated at 80 K within the 1.8 K cavity back wall. Thus, the effect of temperature reduction on the spectral QE of a photocathode is a topic of great interest for SRF photoinjectors. The photocathode must be cooled to a) reduce thermal radiation in the cavity and b) mitigate the heat load from RF surface currents and the photocathode drive laser power. Furthermore, it is expected that the transverse energy distribution of photoelectrons is dominated by the lattice temperature when the excitation energy is lowered close to the photoemission threshold and, thus, ultra-cold electron beams can only be emitted from cryo-cooled cathodes [107].

Literature offers a few recorded data points on the behavior of cryo-cooled alkali antimonide photocathodes, some consistent, some inconsistent. The cooling in a photomultiplier setting, using commercial tubes, was investigated in [22, 44]. The active films were prepared on a Pt conducting layer to mitigate the influence of a change in resistivity. Both references consistently report a slight increase in sensitivity for blue light of $\lambda < 500\,\text{nm}$ and a reduction in sensitivity for red light $> 600\,\text{nm}$. The relative sensitivity depends on the specific sample. In one case it is greater than unity for all wavelengths $< 550\,\text{nm}$, but it generally falls off to about 0.1 for wavelengths $> 600\,\text{nm}$.

Less promising are reports in accelerator applications [108, 109] where a reduction of the QE of up to a factor of 5 was reported. However, lacking information of wavelength or total pressure, it is not possible to attribute these results to either changes in the lattice and population of electronic states or to adsorption of gas species on the surface and changes of the local work function.

In order to obtain reliable performance data for the cryogenic operation, cooling tests with two photocathodes, P013 and P016, have been performed in the preparation chamber in order to observe the photocathode performance in terms of QE. Both photocathodes were cooled with liquid nitrogen using the manipulator in the preparation chamber, which is also used for the sample preparation. The effective cooling for each photocathode varied slightly due to minor difference in the nitrogen gas flow and also in the thermal contact of the copper cooling wire to the sample stage.

The characteristic spectral response plots are shown in Fig. 5.9. No strong reduction of the QE at 2.4 eV was observed when P013 was cooled from room temperature to 150 K. The measured photocurrent remained nearly constant and the maximum vacuum pressure observed was $2 \cdot 10^{-10}$ mbar. A significant decrease in QE was observed when the cold sample was moved into the analysis chamber (in vacuum); which coincided with an increase in pressure above $1 \cdot 10^{-9}$ mbar. The warm up of P013 back to RT neither showed a decrease nor recovery of the QE. To reduce the risk of increasing the vacuum pressure, movement within the system was avoided in the

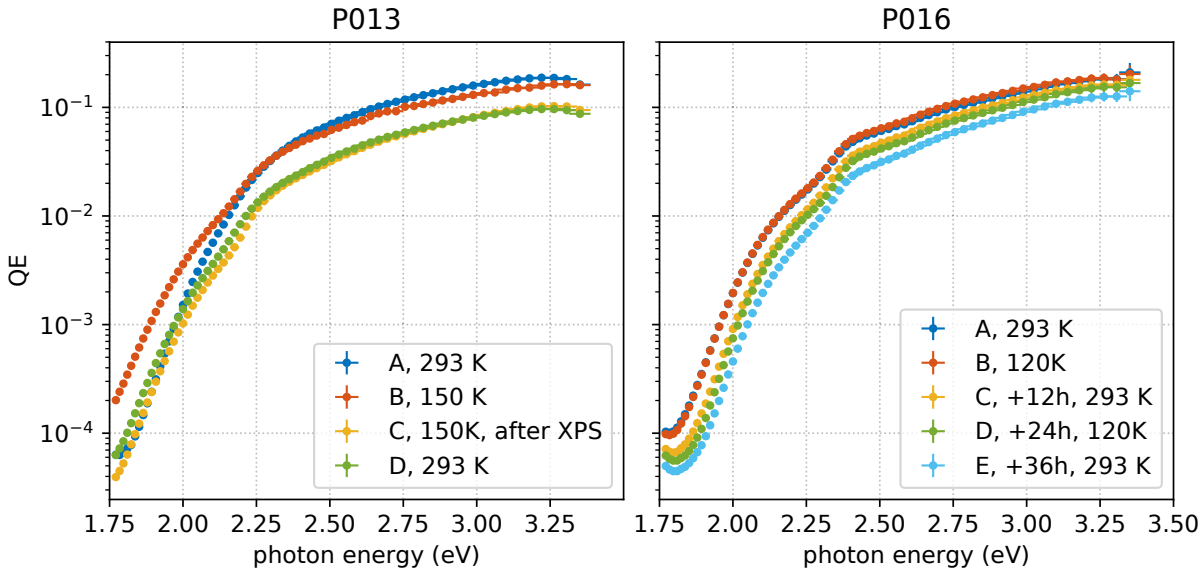

Figure 5.9.: Spectral response of the cathode samples P013 and P016 before, during, and after the cooling.

case of P016. Consequently the pressure stayed constantly below $6 \cdot 10^{-10}$ mbar. There is very little discernible difference in the spectral response between the warm and cold sample (Fig. 5.9, P016, A and B). The decrease of the QE observed in the following measurements (C, D, E) is related to fatigue of the sample, as discussed below.

For the purpose of this discussion, the relative sensitivity, $S_{\mathrm{rel}}(\lambda)$, is defined as the fraction of the spectral response at room temperature and the cryo-cooled sample:

$$S_{\mathrm{rel}}(\lambda) = \frac{QE_{\mathrm{cryo}}(\lambda)}{QE_{\mathrm{RT}}(\lambda)} \tag{5.1}$$

The corresponding plots shown in Fig. 5.10 are deduced from the spectral response measurements during the thermal cycles displayed in Fig. 5.9. For P013, two relative sensitivities are deduced from one cycle as a ratio of the spectral response measurements before and after the cooldown as well as the ratio before and after letting the sample warm up. The two ratios shown for P016 are obtained from the cooldown of two consecutive cycles. The format of Fig. 5.10 has been chosen for ease of comparison to the values reported in the literature, e.g. [44]. Notably, for both samples the relative sensitivity differs strongly between the first thermal cycle (blue lines) and the second thermal cycle (red lines). The spectral sensitivity during the first cycle shows values greater than unity, and yet there is no clear trend nor similar behavior between the two samples. The difference in behaviour can perhaps be attributed to the fact that during the first thermal cycle, the photocathode is still active - the alkali metals would still be diffusing into the Sb layer, and residual gas molecules would be adsorbing on the pristine surface. This dynamic environment contrasts with the relatively saturated surface found during the second cycle. The pronounced increase

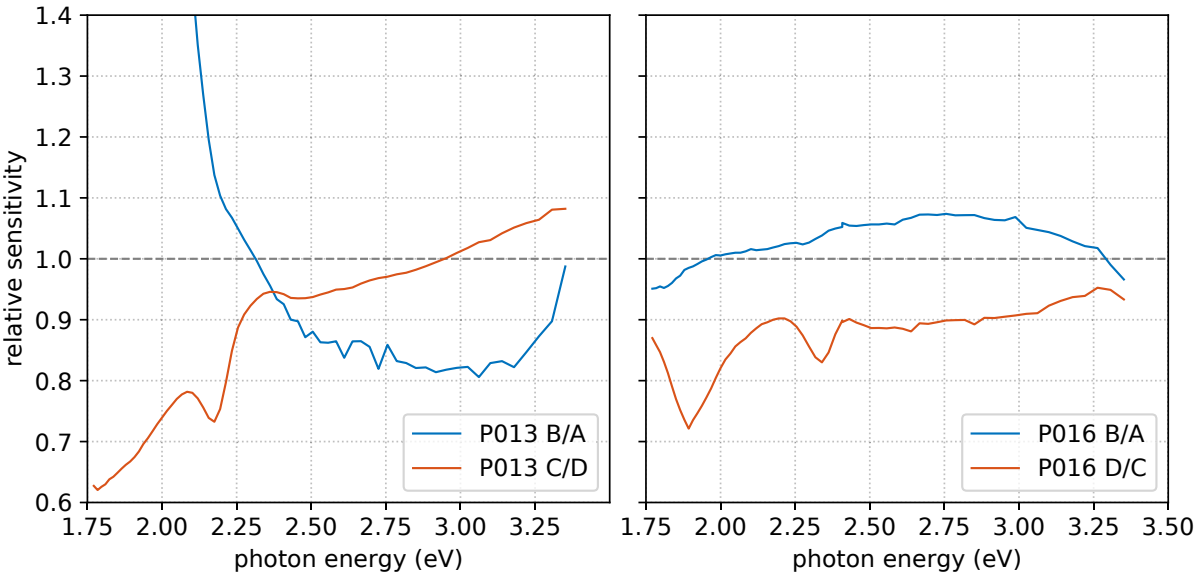

Figure 5.10.: Relative sensitivity of the two samples that were cooled. The spectral response was measured at room temperature and 150 K and 125 K for P013 and P016, respectively.

in the low-energy response shown for P013 B/A has also been reported in [96] after a slight exposure (<2 L) to oxygen. We therefore attribute this effect to the adsorption of oxygen on the surface and formation of a surface dipole, in this case intensified by the larger sticking coefficient of the cold surface.

Considering the relative sensitivity measurements from the second cycle, it is evident that the results are in agreement; they indicate that the spectral sensitivity reduces with lower photon energy. One may assume that the reduction in QE for low photon energies can be explained by a reduced number of states populated by the tail of the Fermi-Dirac distribution which contribute to photoemission at room temperature but are less populated at cryogenic temperatures. At the same time the number of scattering partners for the electrons excited by higher photon energies is reduced, thus the mean free path and QE are increased; this can explain values greater than unity or a less pronounced loss of QE for excitation energies greater than 2.5 eV. Yet, such general consideration cannot explain the oscillatory behavior observed in the range of 2.0 eV and 2.5 eV (red lines in Fig. 5.10) which necessitates a much more detailed treatment, taking into account the full band structure and scattering during the emission process; such models are currently being developed by [21, 110]. The measurements presented by Menegolli *et al.* and Nathan *et al.* agree with the results presented here by the fact that the QE at approximately 2.4 eV remains constant with temperature [22, 44].

Their measurements are performed in PMT tubes where one may assume that vacuum effects are not dominant and the effect of reduced electrical conductivity is mitigated by metallic leads or a Pt conduction layer.

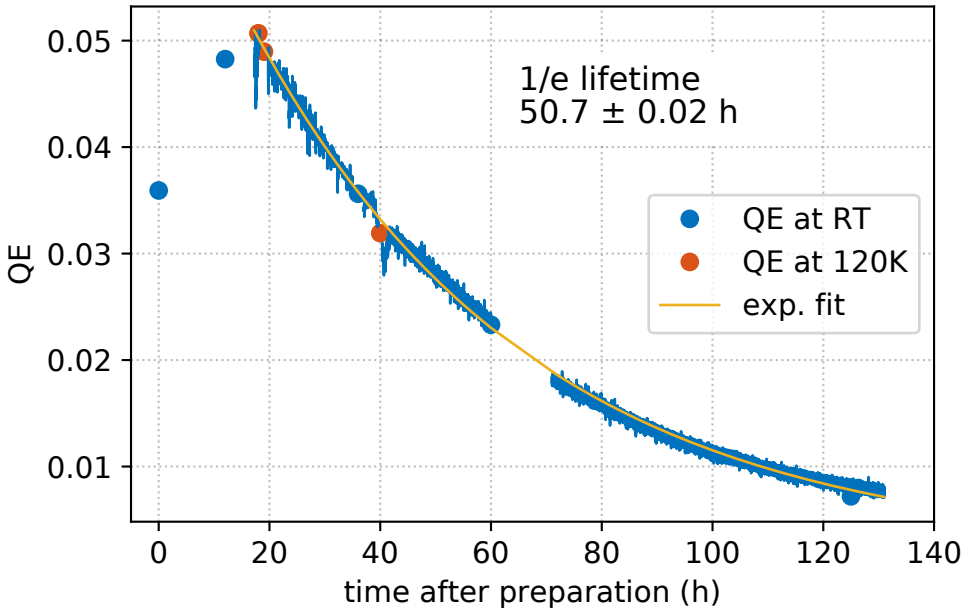

Figure 5.11.: Lifetime in terms of QE at 515 nm of sample P016. The emphasized data points (red and blue circle) are extracted from the spectral response measurements at room temperature and 125 K, respectively, while the blue curve represents a continuous measurement.

There are two additional effects to consider when discussing the behavior of cathodes at cryogenic temperatures. For one, the sample surface has a much higher sticking coefficient for the adsorption of residual gas molecules, i.e. the sample acts as a cryopump. Adsorbed molecules and atoms change the local work function and, in case of reactive species like oxygen and water, contribute to the degradation of the sample by oxidation of Sb and segregation of alkali ions from Sb. It is therefore essential to run cooling experiments in pure vacuum to suppress this effect. Secondly, as reported by [22, 111] the conductivity of K_2CsSb is reduced by 5 orders of magnitude when the sample is cooled to 150 K. While a possible charge-up effect represents an issue for the use in photomultipliers on a glass substrate, it is not expected to affect thin film photocathodes grown on metallic substrates.

These experiments indicate that the operation of a Cs-K-Sb photocathode at 80 K is possible without compromising the QE. Nevertheless the vacuum conditions in the SRF photoinjector are still unknown, but are expected to be even better than in the preparation chamber, because of the enhanced cryogenic pumping performance of the Nb-cavity at 1.8 K.

Generally at the target wavelength of 515 nm the change in QE is around 10%. In this case, the QE is found to be dominated by the age induced decay of the sample with only slight deviations from the exponential behavior due to temperature cycles: according to Fig. 5.11 the cooling and warm up cycles did not lead to significant acceleration of the degradation process, and the separate values taken from spectral response

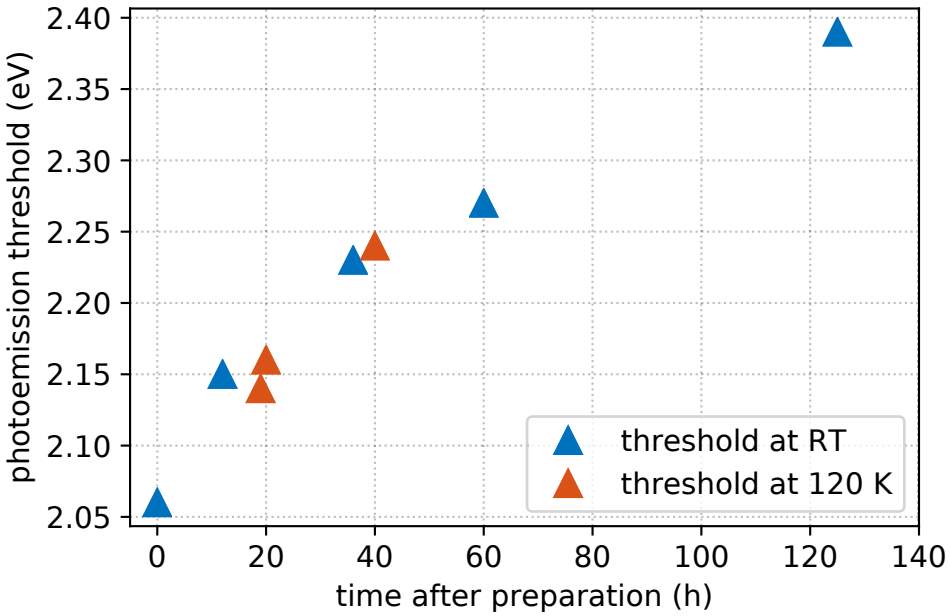

Figure 5.12.: Evolution of the photoemission threshold of sample P016 during the cooling experiment. The increase of the threshold progresses with time and independently of the sample temperature.

measurements line up with the exponential decay that progresses independently of the temperature.

A $1/e$ lifetime of 50.7 h was determined for the sample P014, by illuminating the photocathode with green light (2.4 eV) over more than 120 h. The constant illumination was paused at several points to acquire the spectral response and the corresponding points are highlighted in Fig. 5.11.

To determine the photoemission threshold, the spectral QE shown in Fig. 5.9 is approximated to a linear function [62]:

$$QE(\nu) = A(h\nu - \phi) \tag{5.2}$$

where A is a constant equivalent to the gradient, and ϕ is defined as the photoemission threshold and is determined from the x-intercept. The values for the photoemission threshold are shown in Fig. 5.12.

In the first 19 h after preparation, the QE continues to increase due to the ongoing reactions in the photocathode layer. After this period, the QE decreases, and an increase of the photoemission threshold is observed; this is likely related to the adsorption of residual gas molecules and their reaction with the highly reactive photocathode layer [112]. By the end of the measurements (125 h) the QE reached 0.7% and the threshold calculated was found to be 2.39 eV.

6. Intrinsic Emittance and Mean Transverse Energy

The normalized intrinsic emittance $\varepsilon_{n,u}$ is defined by the emission spot size σ_u and the mean transverse energy (MTE) due to the photoemission process

$$\varepsilon_{n,u} = \sigma_u \sqrt{\frac{MTE}{m_e c^2}} \tag{6.1}$$

and is often a large fraction of the emittance in the injector (see chapter 2). A measurement of the intrinsic emittance is therefore key to understand the influence of the photoemission process on the beam quality and to derive empiric or analytical models that describe the intrinsic emittance. In that sense, the dependence of the intrinsic emittance on the excitation energy and temperature is of great interest during the design of a photoinjector.

The following chapter describes a measurement of the MTE obtained from Cs_3Sb which was carried out at the photocathode laboratory of Cornell University.

6.1. Preparation of the Sample

The data in this section refers to a Cs_3Sb sample grown on a polished single-crystal silicon substrate in (100) orientation with strong n-type (Phosphorus) doping. The substrate was rinsed in isopropyl alcohol, etched in a 3% HF solution to remove the native surface oxide, and placed on a Puck-style substrate holder as shown in Fig. 3.12. After transfer into the photocathode system by means of a vacuum load-lock, the substrate was baked in UHV at 450°C.

A photosensitive Cs-Sb film was grown on the entire surface of the substrate by deposition of 20 nm of Sb at a rate of 0.5 nm/min and a temperature of 160°C and subsequent exposure to Cs vapor from an effusion cell while the substrate temperature slowly cooled from 130°C to 50°C. The Cs deposition was stopped when a plateau in the monitored photocurrent was observed and the QE at 532 nm was 1.7%.

The spectral response of the sample was determined after the transfer to the vacuum chamber of the TE meter. The drain current was measured by means of a Keithley model 6487 picoampere meter with 18 V bias applied to the cathode by a battery. The

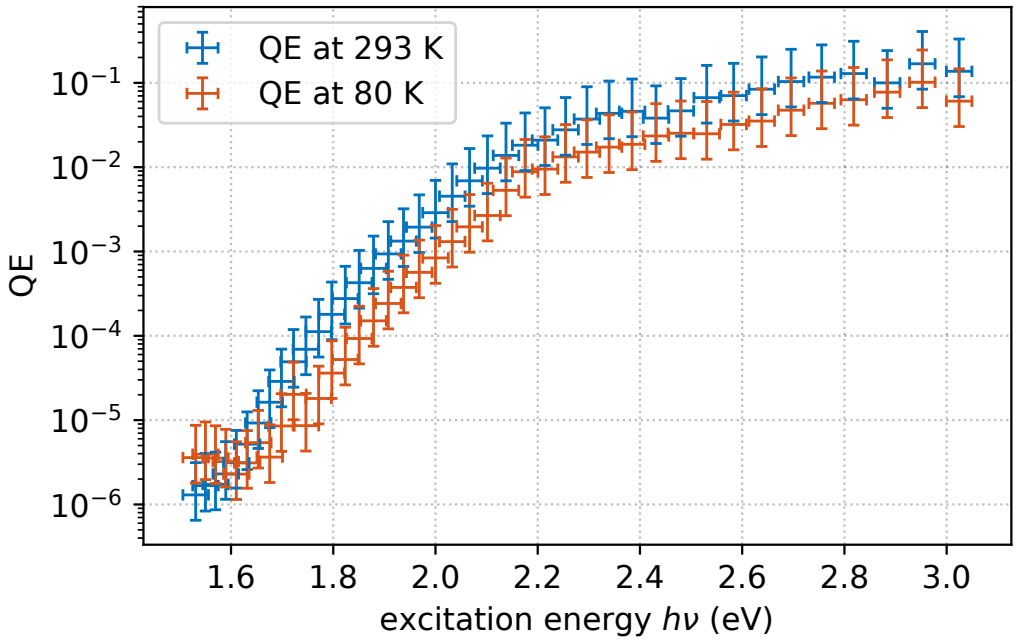

Figure 6.1.: Spectral response of the Cs-Sb sample. The threshold changes by 0.1 eV due to the cooling.

sample was illuminated by the drive laser used for the TE meter measurements using the identical setup to suppress out-of-band contributions from the supercontinuum laser as discussed below.

It is evident from Fig. 6.1 that the slope of the spectral response is identical near the photoemission threshold but the peak QE is lower for the cooled sample. The two spectra show a shift due to the respective photoemission threshold of 1.7 eV and 1.6 eV in the 293 K and 80 K case, respectively.

6.2. Measurement of the Mean Transverse Energy

Photoemission from the sample was excited with broadband light from a supercontinuum laser (NKT SuperK extreme) which was filtered by an Acousto-optic Tunable Filter (NKT Varia) which allows to select a 10 nm broad bandpass region between 410 and 800 nm. The illuminated spot size on the sample was defined by a set of interchangeable pinholes, each on a magnetic base. The pinholes were aligned to assure a common position of the centroid of the beam on a virtual cathode camera and the pinhole plane was imaged on the sample by a single f=250 mm achromatic lens. Pinholes of diameter 100 to 500 μm were used in 100 μm steps. The beam position on the sample was aligned using the screen camera which, when focused at the anode, captures the diffuse reflection of the laser spot and the circular anode opening.

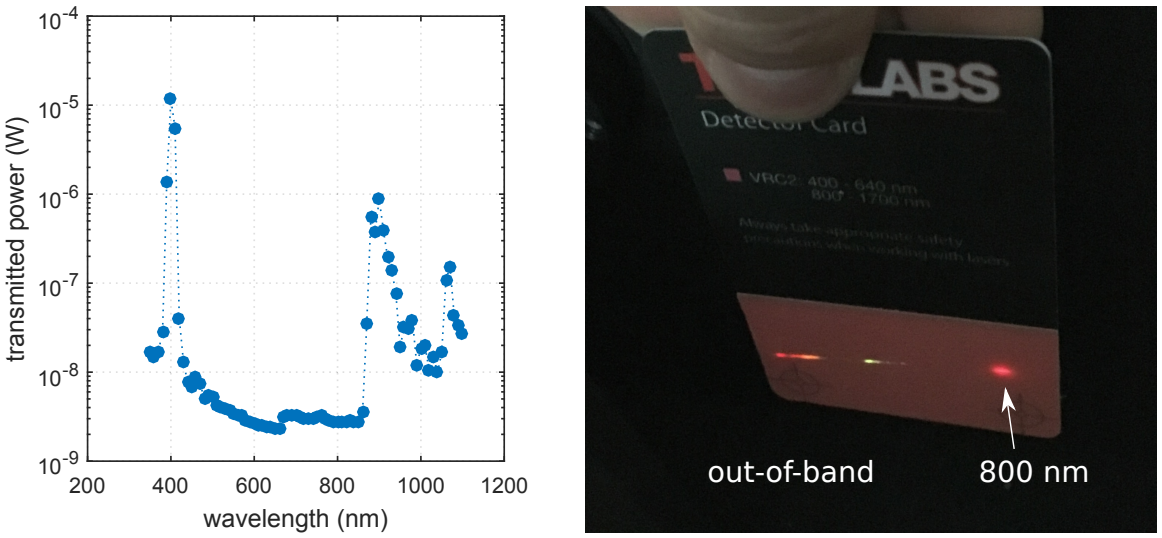

Figure 6.2.: Spectral flux of the pre-filtered excitation laser. Left: Spectrum of the light when the output is centered at 405 nm. The remaining IR contribution was filtered by a short pass filter at 850 nm. Right: Photograph of the dispersed light when the output is centered at 800 nm. Clearly, short-wavelength contributions are present in the spectrum and require additional filters.

A region of interest defined in the camera software then allows to center the beam centroid in the anode circle.

The optical filter does not fully suppress all out-of-band wavelengths (as shown in Fig. 6.2) so in practice a series of reflective longpass and shortpass filters were used to enclose the bandpass spectrum within 50 nm steps and further suppress the unwanted parts of the spectrum. The short-wavelength contribution was especially observed trough a non-physical increase of the quantum efficiency at long wavelengths. Likewise, the effective filtering of these out-of-band components could be verified by the mitigation of this effect. With the light source aligned and focused, and monochromaticity ensured, the intrinsic emittance of the photocathode sample could then be measured for several wavelengths.

At each wavelength and pin hole (initial beam size) setting, the accelerating voltage was scanned between 2 kV and 10 kV in 500 V steps and images of the screen were captured to obtain the beam size at each step. After background subtraction, the beam size for each image was obtained from a 2-D Gaussian fit to the intensity distribution.

The initial beam parameters are calculated within a linear approximation to the beam optics model using equations 3.13 and 3.18. Figure 6.3 shows two exemplary fits to the voltage scan at 450 and 700 nm. A linear regression is performed at every excitation wavelength for the different initial beam size settings. The intrinsic emittance is thus averaged over the number of measurements, as shown in Fig. 6.4.

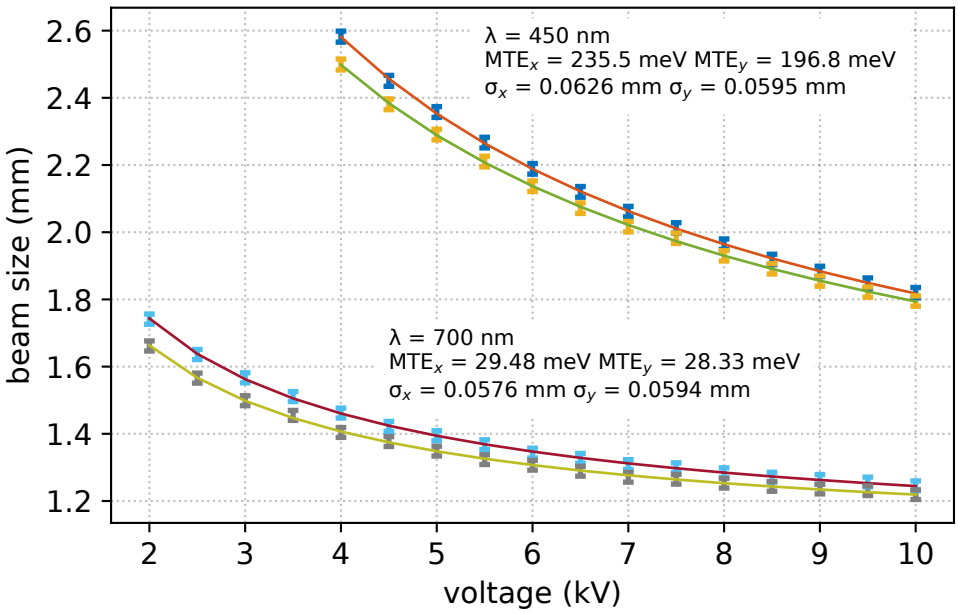

Figure 6.3.: Exemplary data of two voltage scans at 450 (top) and 700 nm wavelength (bottom) with a 300 μm pin hole, the beam size measured in x and y direction is shown. A low transverse energy below 30 meV is measured for the near threshold excitation at 700 nm while it is much higher at 450 nm.

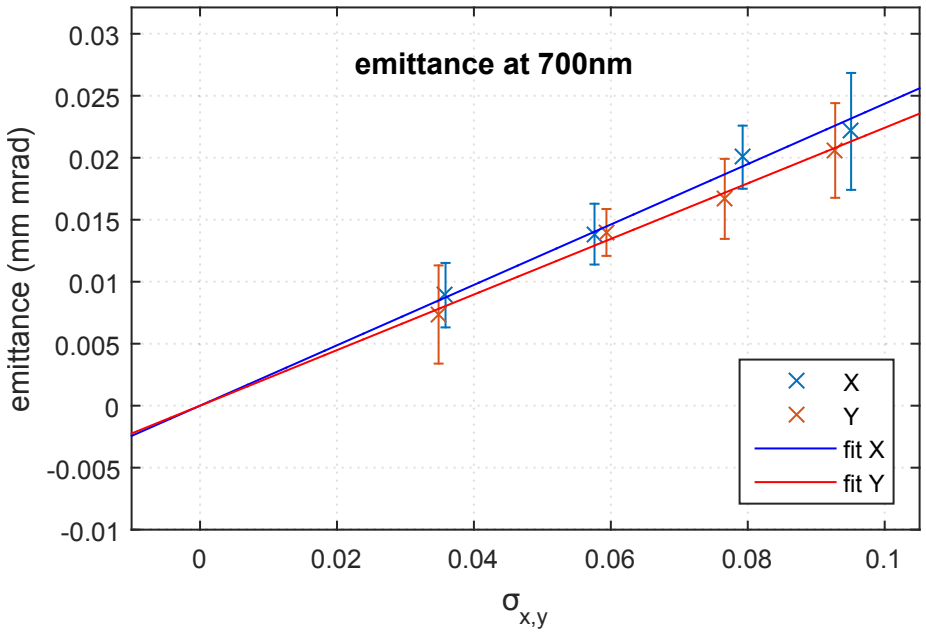

Figure 6.4.: Linear regression to the intrinsic emittance obtained at different initial beam sizes.

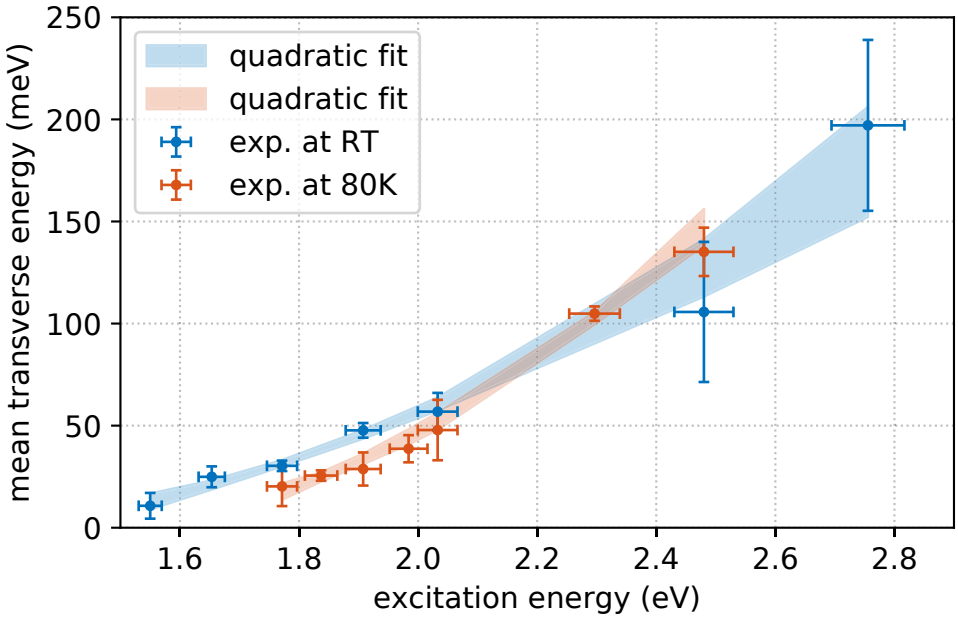

Figure 6.5.: Empirical quadratic model to the MTE.

Finally, the data points for each wavelength are computed as detailed above and collected in a MTE versus excitation energy plot as shown in the Figures 6.5, 6.6, and 6.7. A strong decrease of the MTE is observed with lower excitation energy as it approaches the photoemission threshold. Empirically, the data can be represented by a quadratic function. The minimum values of the two fit functions are located at photon energies lower than the emission threshold and cannot be used for photoemission. Effectively, the lowest MTE attainable is 20 meV using 750-800 nm light at room temperature and 16 meV using 700 nm at 80K. The data sets coincide in the value at 2.4 eV (515 nm) where the MTE amounts to 120 meV. The data presented here, is in an energy range where the MTE deviates from the linear slope predicted by very simple models of the MTE like the assumption that MTE $= \frac{h\nu - \Phi}{3}$.

The difficulties in modeling near-threshold (low energy) photoemission are that the low kinetic energy of excited electrons results in a long de Broglie wavelength indicating a strong influence of surface effects, scattering partners and impurities. Scattering events are particularly relevant as they – in a semi-classical picture - randomize the momentum distribution of the excited electrons. Additionally, for alkali antimonides, significant uncertainties and ambiguities exist in the literature regarding macroscopic solid-state properties that are parameters to the transport step in the three-step model. Presently, the most successful models in terms of reproducing experimental emission data from semiconductors are semiclassical models where the density of states is obtained from ground state DFT calculations and the transport step is treated in the Monte-Carlo approach [19, 21].

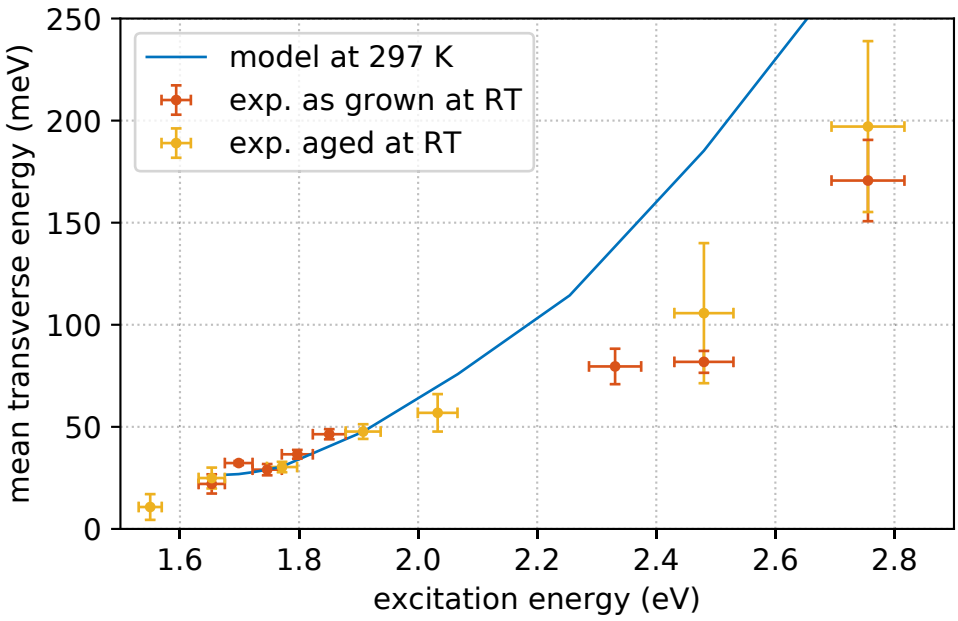

Figure 6.6.: Measured values and model of the MTE at room temperature. The model data was extracted from [21].

The model recently presented in [21] is assumes a parabolic shape of the highest occupied and lowest unoccupied Γ-valleys, a tail of acceptor states within the band-gap and models the transmission step within a Monte-Carlo approach considering only polar optical phonon scattering. The details of their simulation are well documented in [21]. Below, the experimental data is compared to the modeling results. Two sets of measurements are shown along the model data. The same Cs_3Sb sample was measured at room temperature and at 80 K, directly after preparation and two weeks later. The measured data sets are indicated "as-grown" and "aged" in the figures and show no significant difference except the marked increase in the 80 K case for the aged sample which is discussed below. Clearly, the MTE near the photoemission onset is well represented by the model. In the room temperature case, it seems that the model overestimates the MTE for higher excitation energies.

Despite the significant scattering in the 80 K experimental data it is well represented by the model. Unlike the theoretical prediction, however, the experimental data seems to flatten towards a limiting value of 20 meV when approaching the photoemission threshold.

The high-MTE point at 1.85 eV for the aged sample at 80 K cannot be explained within the interpretation presented so far. One plausible interpretation is that the signal due to single photon absorption is low enough and the laser fluence high enough that two-photon photoemission becomes dominant at this point. A recent model for metals [113] reports that the fraction of singly excited electrons reduces below 1 at a laser fluence above 10^{-5} mJ/cm^2 when the photon energy is slightly below the

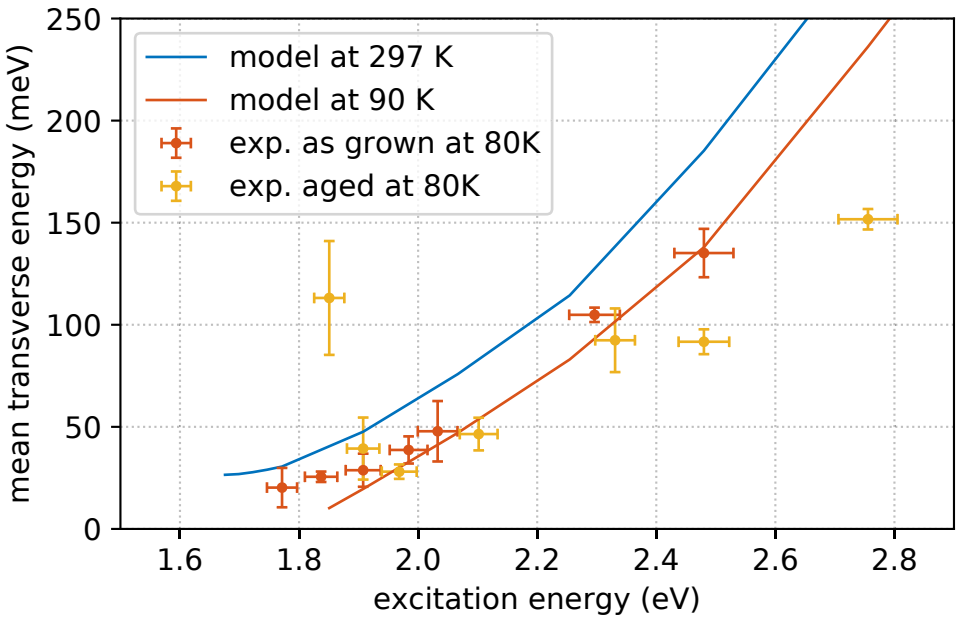

Figure 6.7.: Measured values and model of the MTE at 80 K.

photoemission threshold. The laser fluence in this experiment was up to 10^{-6} mJ/cm^2 for low photon energies, thus a strong emittance increase like evident in the model in Fig. 6.8 can be expected. The measured MTE increases when multi-photon emission contributes to the emission because a higher total energy is transferred to the electrons.

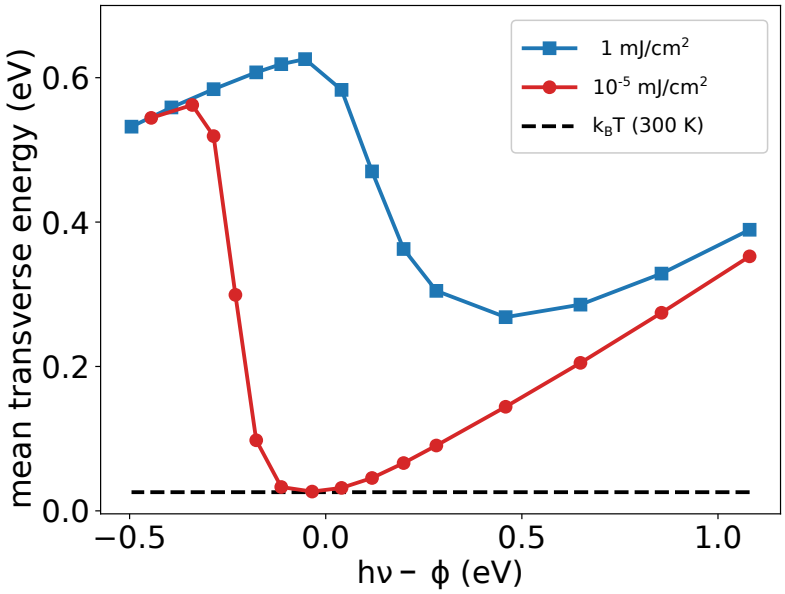

Figure 6.8.: Model of the MTE obtained from a copper surface considering single and two-photon emission at high laser fluence near the photoemission threshold. Reprinted from [113].

7. Cathode Transfer and Commissioning of the Photoinjector

The insights gathered in the previous chapters should finally be employed to grow high quality photocathodes and demonstrate the commissioning of the entire photocathode life-cycle from substrate preparation, deposition and characterization, to UHV transport and application in a superconducting RF photoinjector. In this chapter the design of the cathode interface to the SRF photoinjector as well as results from the assembly and commissioning of the photoinjector prototype are presented.

Following the operation of an SRF photoinjector prototype with a fixed, superconducting lead cathode in the back wall [35–37], the current experiment realized a new SRF cavity within a dedicated cryomodule [114], an enhanced diagnostic beam-line [49, 115] and a cathode transfer system that allowed the exchange and insertion of normal conducting photocathodes on a plug substrate.

The photoinjector experiment was commissioned in the radiation shelter of the HoBiCaT experiment, and an overview is shown in Fig. 7.1. During operation, the cavity is immersed in a liquid Helium bath which is kept at 1.8 K by evacuating the gaseous phase to a pressure of 16 mbar. Such low temperatures can only be sustained in vacuum insulation and when the radiative heat load from the room temperature walls of the cryomodule is shielded by a metallic thermal shield at 80 K and several layers of thin Aluminum foil ("superinsulation" foil). The cryogenic liquid is supplied from a central liquefier and distributed in vacuum-jacketed pipes. A separate vacuum tank (feedbox) next to the cryomodule contains the required valves and reservoirs from where the liquid is supplied to the experiment. The components that need to be close to the cavity and thus inside the cryomodule are assembled in the clean room as the "cold string" shown in Fig. 7.2. Its main parts are the cathode cooler and RF filter assembly, the cold parts of the fundamental power coupler and the cold part of the beamline with the solenoid lens, a SiC absorber for higher order RF modes, and air-coil corrector magnets. After assembly in the clean room, the cold string was installed in a dedicated cryomodule.

The drive laser system is based on a Ytterbium (Yb) doped oscillator crystal whose emission is amplified in an Yb doped glass fiber. The central emission is at 1030 nm and frequency doubling crystals are used to generate radiation at 515 and 257 nm wavelength. A beamline guides the light from the separate laser hutch to the photoinjector, transporting both the green and UV wavelengths. Within the beamline is a variable aperture and selectable pinholes which are imaged onto the cathode surface

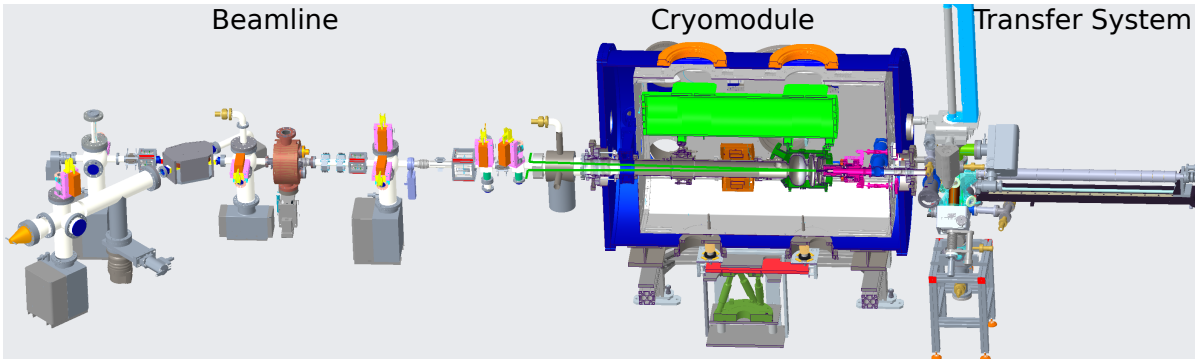

Figure 7.1.: Overview of the photoinjector test setup showing (from right to left) the transfer system, the cryomodule, and the diagnostic beamline.

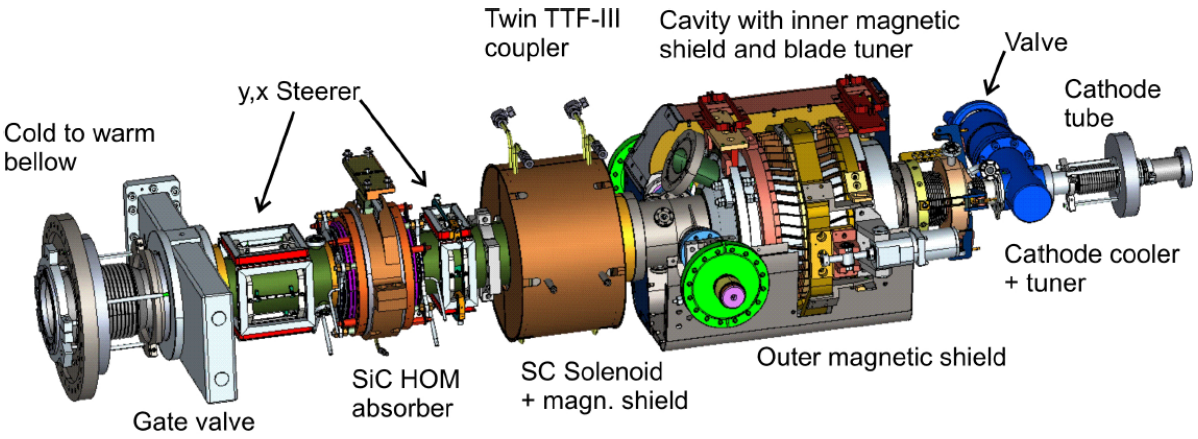

Figure 7.2.: Components inside the cryomodule, the cold string. Image courtesy of A. Neumann [116].

plane. In order to comply with the current limits imposed by the operation permit of the radiation shelter, the laser was operated at a reduced frequency of 12 kHz; phase locked to the master oscillator of the 1.3 GHz RF signal of the cavity. The laser pulse energy can be adjusted by altering the current of the diodes that pump the amplifier and was kept below 70 nJ (UV light power at the cathode) throughout this work. After a cold start the power stabilizes to ±0.3% after a few minutes and the pulse length stabilizes to 1.5 ps FWHM (UV) after a few hours.

A diagnostic beamline was developed and comissioned in order to analyze the properties of the electron beam and is detailed in [49]. It allows the measurement of average current and pulse charge via charge collection in a Faraday cup, the measurement of the beam momentum and momentum spread by bending the beam into a dispersive section as well as transverse emittance measurements in a slit scan with scanner coils as well as waist scans of a quadruple pair and the solenoid lens. A transverse deflecting cavity is foreseen to allow full characterization of the bunch length and slice emittance and thus achieve a 6-D characterization of the phase space distribution.

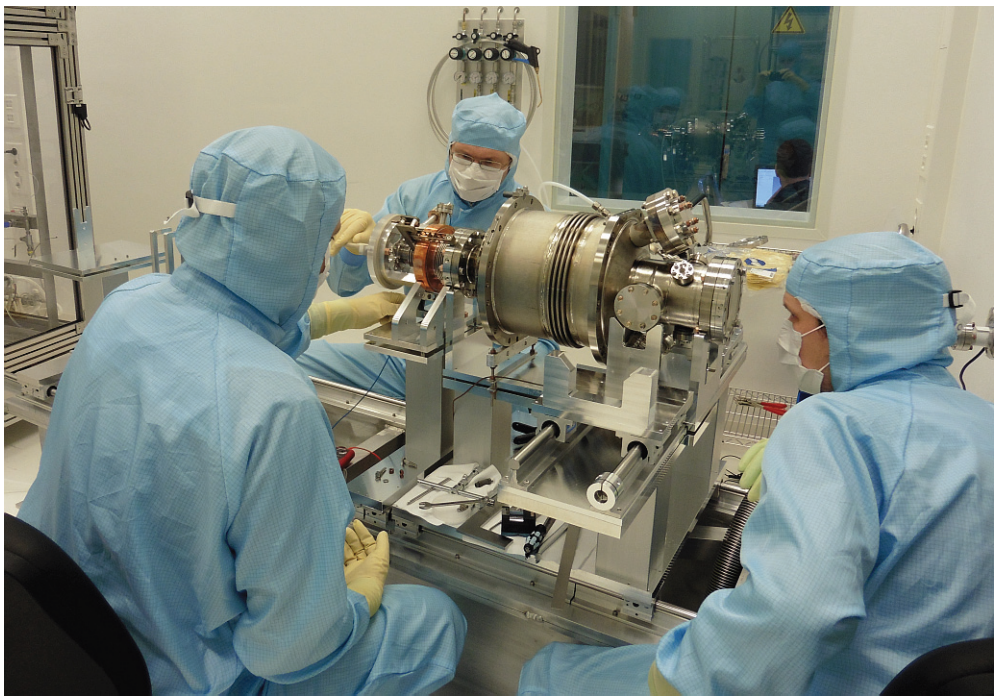

Figure 7.3.: The SRF gun cavity during assembly in the cleanroom. The cathode interface is mounted on the left hand side of the cavity (hidden in its He tank) and must be aligned to ensure a concentric axis between the RF filter and the hole in the back wall.

7.1. Cathode Interface and Transfer Systems

The challenges in the engineering of the exchangeable cathode interface to the SRF gun are that the normal conducting cathode cannot be in contact with the superconductor, both to avoid thermal quenching of the cavity as well as to disconnect the cathode from surface currents flowing in the cavity wall. Furthermore, particulate-free cleaning and assembly of all components must be ensured in order to mitigate particulate contamination of the cathode and cavity.

The ring shaped opening between the cathode and the cavity wall allows the passage of RF field components into the region behind the cathode and a choke cell structure and a RF filter in coaxial arrangement is required to reflect the RF power before it propagates towards the normal conducting components upstream of the filter. A detailed view of the CAD model of the cathode interface to the cavity is shown in Fig. 7.4. A photocathode plug (red) is held onto the cathode insert (pink) by means of the internal clamping mechanism. The insert with the plug can be moved along the cavity axis and thus extracted and inserted from the right hand side, by means of the cathode transfer system, which is shown in Fig. 7.5. Upon insertion, the insert is locked in place by a bajonet mechanism that applies forward pressure towards the conical opening in the filter (copper brown).

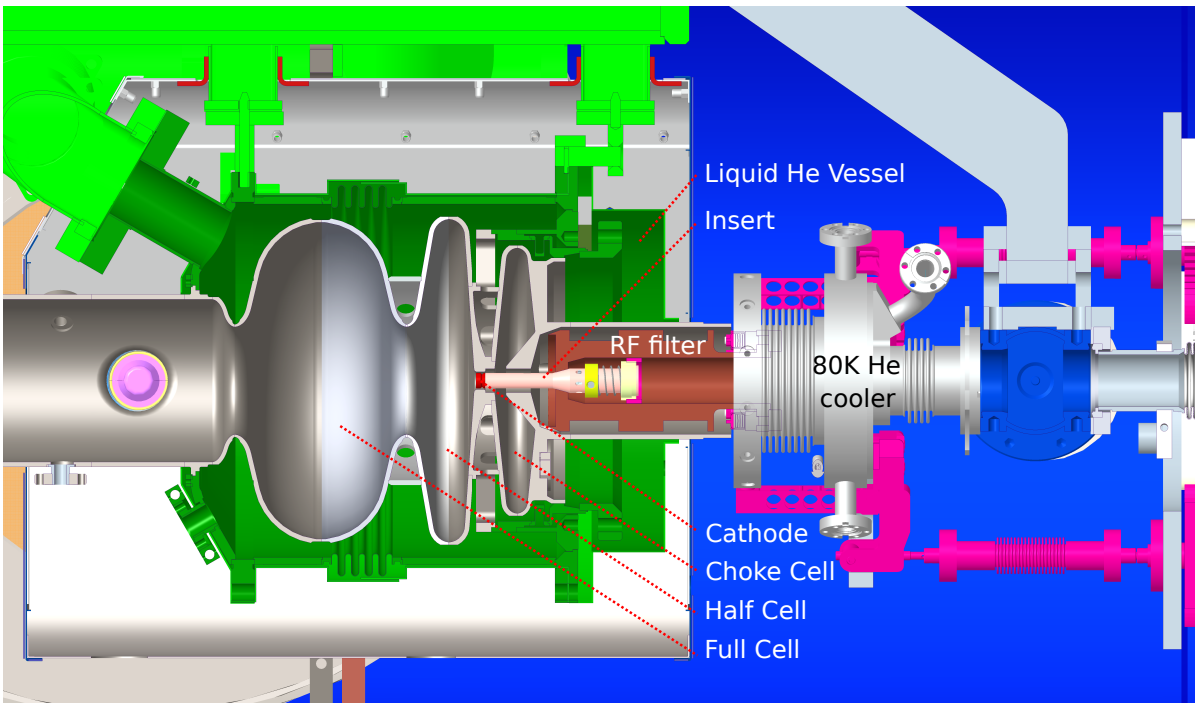

Figure 7.4.: Detailed view of the cathode interface to the SRF injector. The Cathode plug, insert, and cooler are shown on the right, with the cathode protruding into the back wall of the cavity.

The cathode must be cooled by a cryogenic medium in order to reduce the radiated heat inside the cavity and dissipate the heat that is introduced by RF induced surface currents and the drive laser. In practice, the cathode cooler (grey, not cut in the picture) is circulated by gaseous He at 80 K and the heat transfer must pass from the cathode plug through the insert, and an electrically isolating ceramic towards the cooler.

Particle free conditions of the cathode systems require that the cathode cooler and RF filter assembly is cleaned and prepared in the clean room to the same standards as the SRF cavity itself during assembly of the cold string. All UHV components of the transfer systems and suitcase, especially the horizontal manipulator and cathode insert are carefully cleaned and assembled in the clean room. All parts are pre-cleaned by wiping with isopropanol and dry-ice cleaning prior to insertion in the clean room. Especially edge-welded bellows and membrane vacuum hoses showed increased particle contamination before the cleaning steps, even if they were declared as "clean room compatible" by the manufacturers. Dry-ice cleaning was applied also to sensitive bellows and showed effective removal of the contamination in terms of the particle count rate and no vacuum leaks were opened. UHV chambers and the in-vacuum mechanisms were cleaned in ultrasonic baths in ultra-pure water with and without Tickopur detergent, blown dry with filtered, ionized nitrogen gas and assembled only after checking the particle count in the nitrogen flow. Silver-plated nuts and bolts as well as CuNiSi alloy nuts have shown significant and visible abrasion and particle

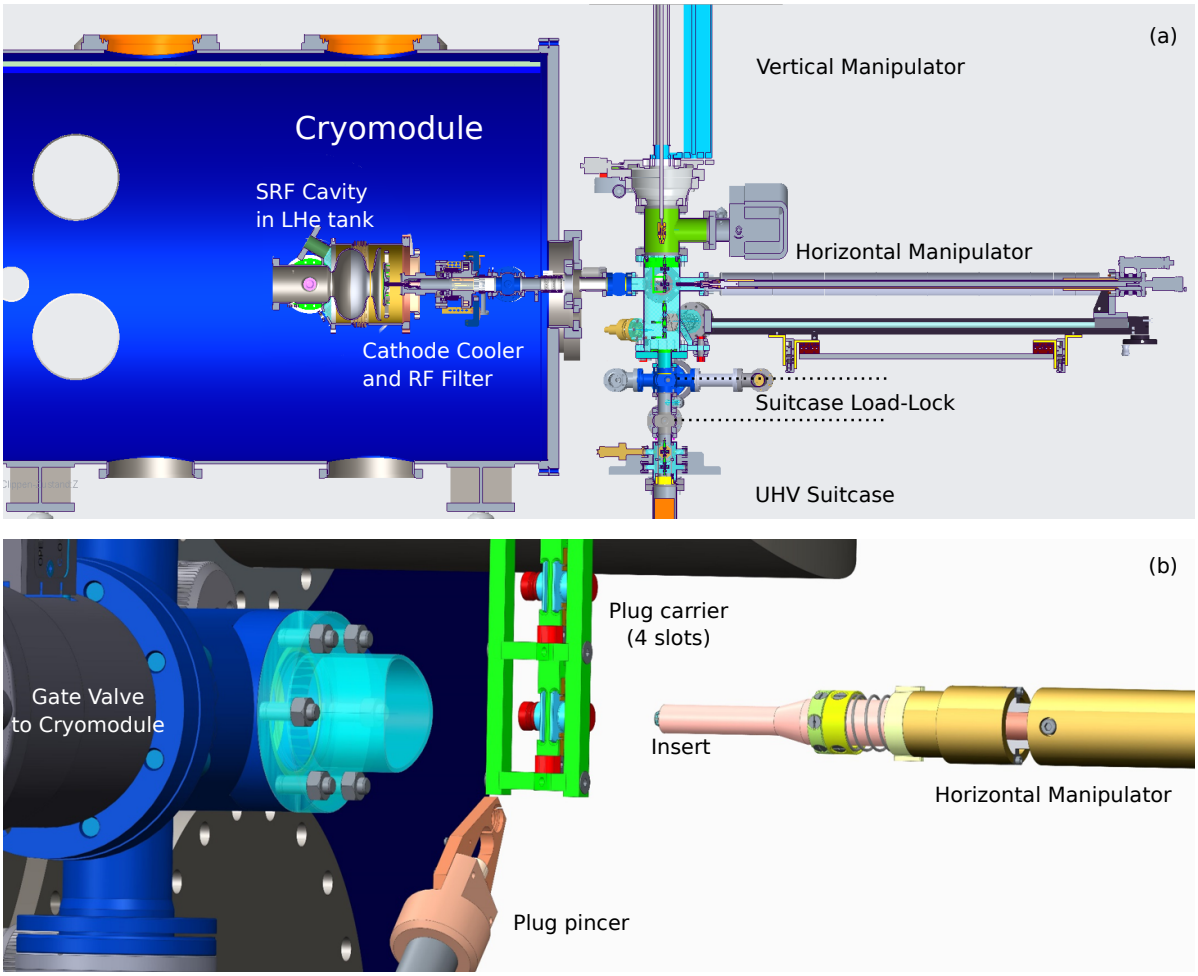

Figure 7.5.: (a) Reduced model of the transfer system at the photoinjector cryomodule. The cryomodule with a section of the SRF cavity and the cathode cooler and RF filter is shown in blue on the left hand side. The transfer system with the UHV suitcase attached is shown on the right hand side. (b) Detail of the plug exchange mechanism. The plug carrier can be fetched from the suitcase and moved by the vertical manipulator. A pincer is used to move plugs between the plug holders and the insert. Part (b) reprinted from [55].

production and are not used in the clean room. Thus, for the flange connections stainless steel and Titanium grade 5 pairs were chosen (Ti nuts and stainless steel bolts or Ti studs in tapped holes). These fasteners were tested within the scope of this work and found to prevent galling, produce low amounts of particles per assembly, provide long term-stability after multiple bake-out cycles and can be used several times in contrast to CuNiSi hardware.

A specialized venting and pumping cart was developed within the bERLinPro project because expedited evacuation and venting in the turbulent flow regime can move

	rel. peak intensities			atomic percentage*		
	Cu	O	C	Cu	O	C
as prepared *ex-situ*	90.3	5.5	4.2	36.9	19.3	43.8
after annealing 200° C	96.7	1.2	2.1	60.1	6.3	33.6
after Ar^+ etch	99.5	0.0	0.5	88.9	0.5	10.6

Table 7.1.: Relative peak intensities and atomic concentrations of the copper sample G-001 after different preparation steps. * see text regarding the procedure to determine atomic concentrations.

remaining particles within a vacuum system [117]. The venting and pumping speed at pressures above 5 mbar is limited to $3\,l_n$/min by means of mass flow controllers. At lower pressures the gas transport is governed by molecular flow and the cart can switch to the full pumping speed. A prototype of this cart was assembled in the clean room within the scope of this work and used for the assembly and operation of the transfer system at the gun module. Several improvements to the sealing concept and software defined procedures were implemented.

7.2. Commissioning of the Photoinjector with a Copper Photocathode

Photocathode plugs were manufactured from high purity copper (99.99% purity, Cu-OFE, CW009A) and prepared for the commissioning of the GunLab photoinjector test stand [100]. The advantage of a metallic surface for the commissioning phase is that it is rather robust in terms of vacuum requirements and can tolerate vacuum pressure spikes that are likely to happen during initial conditioning of the cavity when a cathode plug is inserted for the first time. Furthermore, the risk of contaminating the cavity is deemed lower when a metallic plug is inserted, compared to a multialkali photocathode with volatile alkali components.

Several plugs had been manufactured and polished to a surface roughness of $R_q \approx 100$ nm. The plugs were stored for several weeks in a desiccator cabinet which was purged with dry N_2 gas. However several of the samples showed visible tarnishing and color changes after the storage period. New plugs are thus stored in an evacuated cabinet now.

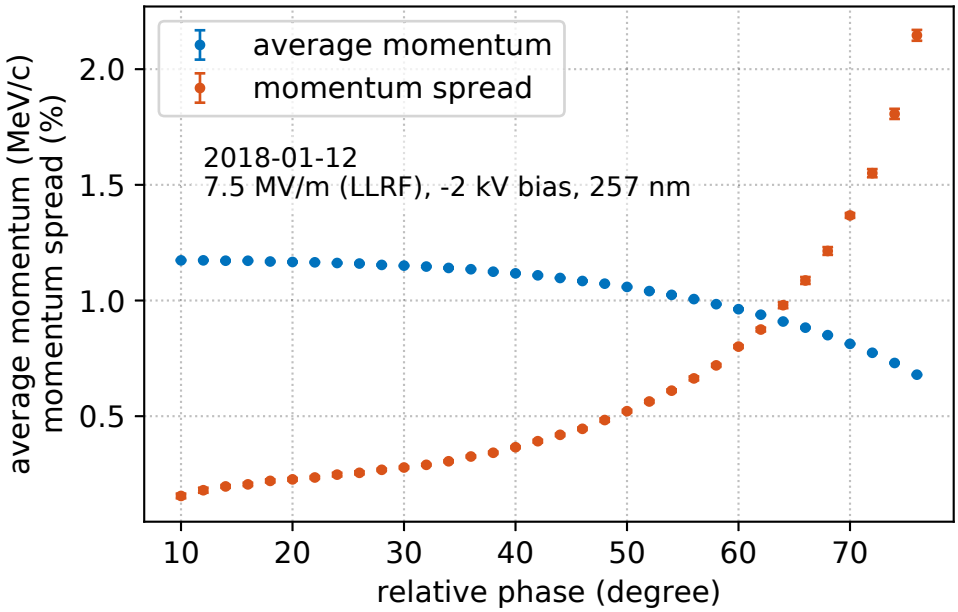

Figure 7.6.: Beam momentum and momentum spread scanned over the extraction phase.

One plug was identified which had no surface irregularities visible under 5x optical magnification but only an oxide layer indicated by a typical color change compared to clean copper surfaces. Optical microscopy is an important step to assure a defect free rim and surface of the plug. The plug was prepared as follows: 1 min of cleaning in a dry ice snow jet was applied to the sample and a plastic carrier box to remove any particulate contamination. A winter bicycle glove under a latex clean room glove was used to hold the parts during cleaning. The sample was then transferred to the photocathode lab, where it was placed in a 0.1 M aqueous solution of citric acid for 5 min with ultrasonic agitation to dissolve the surface oxide. Following a rinse with de-ionised water and isopropyl alcohol for 1 min each, the sample was blown dry with ionized, filtered nitrogen and immediately transferred into UHV. All preparation steps were carried out either in the ISO 14644-1 class 5 clean room or local, class 6 environments and the sample was transferred in the cleaned carrier between the dry-ice cleaning and the steps in the photocathode lab. A witness sample was used to assess the surface roughness after the wet etching with citric acid and showed a slight decrease in the measured surface roughness.

XPS analysis was used to determine the chemical purity of the surface. Spectra of the sample were taken as-prepared, after an annealing step for 20 min at 200° C, and after bombardment with Ar^+ ions at 2 keV for 20 min. Table 7.1 lists the relative peak intensities and surface atomic percentage of copper, carbon, and oxygen after the individual processing steps. Note that the procedure to determine the atomic concentrations assumes that the concentration is constant with depth, as laid out in section 3.3.3. However it is likely that most carbon and oxygen impurities are located

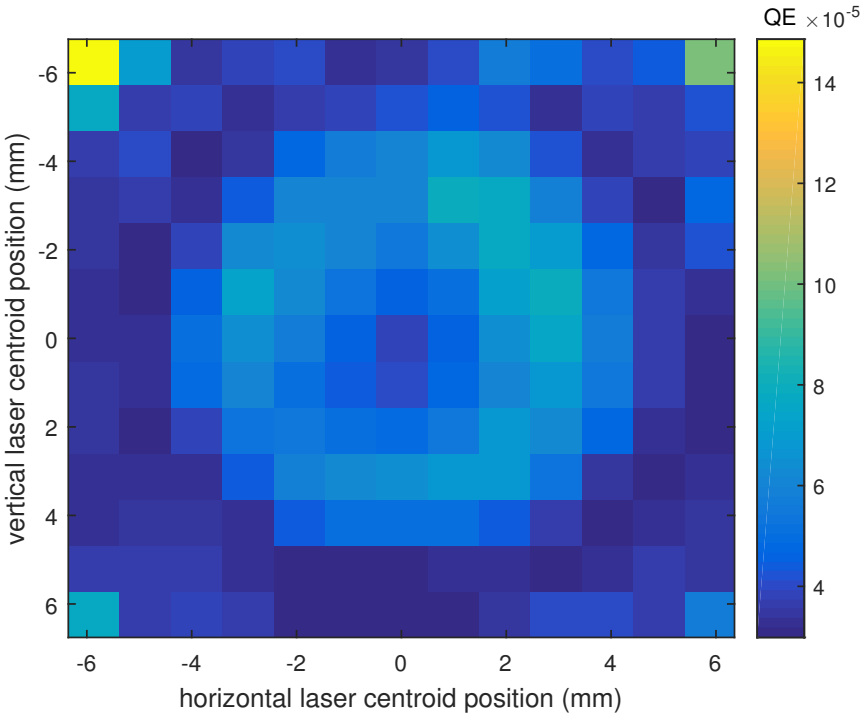

Figure 7.7.: Quantum efficiency map of the copper cathode during commissioning. The data was taken at a gradient of 7 MV/m and a launch phase of 50° relative to the LLRF signal. Reprinted from [100].

at the surface rather than equally distributed within the probe depth of XPS. The signal from surface contaminants is not attenuated by the IMFP, while the copper signal is attenuated but the procedure assumes the same attenuation for all components. Thus, the atomic concentrations in table 7.1 are overestimated and one should use the relative peak intensities as a measure for effectiveness of the cleaning procedure.

The copper photocathode was transferred through the transfer chain as detailed above and inserted into the resonator for the first time in September 2017. Several unwanted events had led to an increase in field emission in the resonator and limited the achievable field amplitude for the operation with cathode to 6 MV/m peak field on axis. Additionally, it was later observed that the cathode protruded too far into the resonator, thus acting as an antenna and suffering from strongly increased losses on the cathode which led to a thermal runaway as the hot cathode expanded even further into the cavity due to its thermal expansion. The situation was clarified once a laser distance tracker was available to scan the back wall of the cavity and the cathode surface. Using this tool and capacitive distance sensors in the cathode interface as feedbacks, the relative position of the cathode cooler and insert position was retracted 0.8 mm behind the cavity back wall. Helium processing was attempted to increase the maximum field amplitude and field levels of up to 7.5 MV/m could be reached afterwards. Following the re-insertion of the Cu cathode, finally, stable RF operation

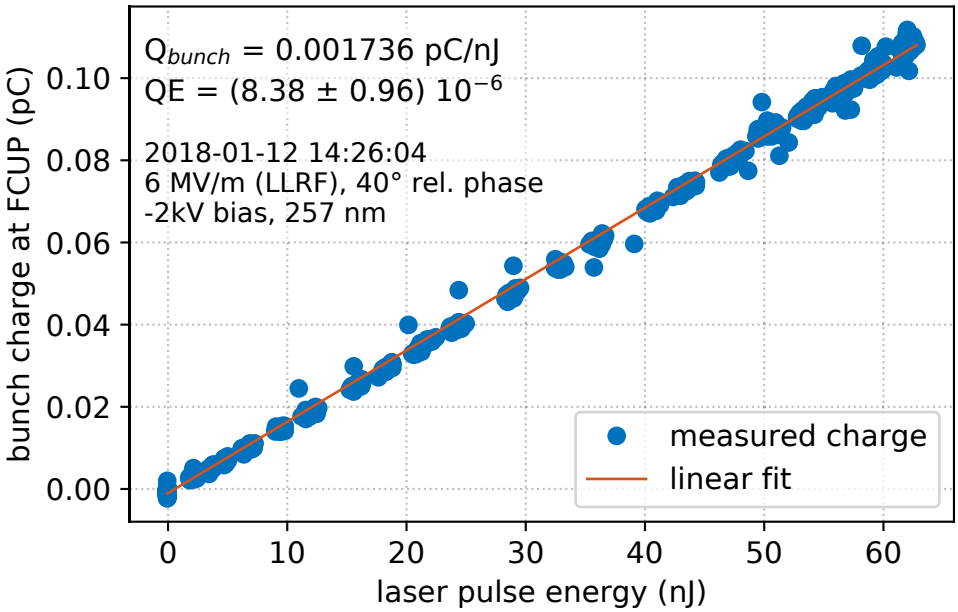

Figure 7.8.: Quantum efficiency scan versus laser pulse energy. The entire range covered here is in the linear regime. The data was taken at a gradient of 6 MV/m and a launch phase of 40° relative to the LLRF signal.

with phase locked laser allowed the generation of photoelectrons in the injector and detection of the beam in the diagnostic beamline. Details of the evolution of the resonator's quality factor, the level of field emission as well as the field calibration and Helium processing are published in [114].

The beam's average momentum and momentum spread was measured by bending the beam by a calibrated magnetic dipole [49] into the dispersive section where it could be detected on a YAG:Ce screen, see Fig. 7.6. The emission phase in this measurement and the values given below are determined from the constant, but relative offset between the LLRF system and the laser oscillator, and shifted to place zero phase approximately at the zero crossing of the electric field.

The QE of the copper cathode was mapped over the surface by scanning the circular laser spot of 1.9 mm diameter using two motorized mirrors at the end of the laser beam line as shown in Fig. 7.7. The injector was operated at a peak field of 7 MV/m and 50° relative phase. The QE of the copper plug is close to the values reported at low fields for clean (Hydrogen ion bombarded) and pure Cu surfaces [16]. Note the high QE values at the corners where the laser reached the Niobium surface which has a lower peak QE than copper but due to the lower work function shows a higher QE at the used wavelength of 257.5 nm. The low QE values at a radius of 5 mm from the center are where the laser spot samples the vacuum gap between cathode and cavity.

Additionally, the QE was determined from a scan of the laser pulse energy with otherwise constant operation parameters, see Fig. 7.8. The slope of the charge

measurement in the linear regime defines the QE. Note the lower value of $8.38 \cdot 10^{-6}$ compared to the values in the QE map above, which was recorded at a higher field amplitude. The quantum yield is field dependent due to the lowering of the work function by the Schottky effect.

7.3. Thermal Load on the Photocathode

It was observed in the beam operation of the current photoinjector setup that the cooling of the cathode is critical to the operation of the photoinjector. The expected power dissipated from the RF field is 14 W at the nominal cathode position and 30 MV/m field gradient. With the cathode protruding further into the cavity the dissipated power rises strongly. It is therefore essential to measure the cathode position relative to the cavity back wall by means of a scanned laser distance sensor [100].

The optical power impinging from the drive laser is at most 25 W for the generation of 100 mA average current at 1% QE. Note that the reflectivity of the alkali antimonides is between 10 and 30% [26, 27, 118–120] - with significant scatter in both the experimental and theoretical data - thus, the thermal design must take a significant fraction of the laser power into account for the cooling budget of the cathode and cavity. Also note that both the electrical and thermal conductivity of the metallic substrates and Copper cathode insert reduce with increasing temperature thus possibly leading to an uncontrolled overheating of the cathode.

The radiated power from the cathode's front face is less than 0.1 W for temperatures below 400 K, even if assuming a black body in the Stefan-Boltzman law, and is thus unlikely to cause a too high load on the Helium bath.

In the case of the first commissioning of the photoinjector, with the cathode protruding into the cavity, the heat load was certainly even too high to operate the metallic photocathode and led to the failure of the cathode insert. In the case of a coated Cs-K-Sb photocathode layer it has however been shown that the lifetime of the film reduces drastically above 70°C due to loss of Cs from the compound [121]. This temperature should thus be regarded as the maximum operating temperature for Cs-K-Sb photocathodes. Higher operating temperatures might be tolerable with Na-K-Sb photocathodes where photomultiplier tubes with this kind of cathode are specified up to 200°C operation temperature.

Previous experiments in the BNL/JLab DC gun have shown that a substrate of high thermal conductivity, i.e. Mo or Cu, is required instead of stainless steel in order to sustain a tolerable temperature during several W of laser power irradiation. Additionally, cryogenic cooling is required to shift the temperature gradient such that the cathode surface remains below the specified temperature e.g. 70°C.

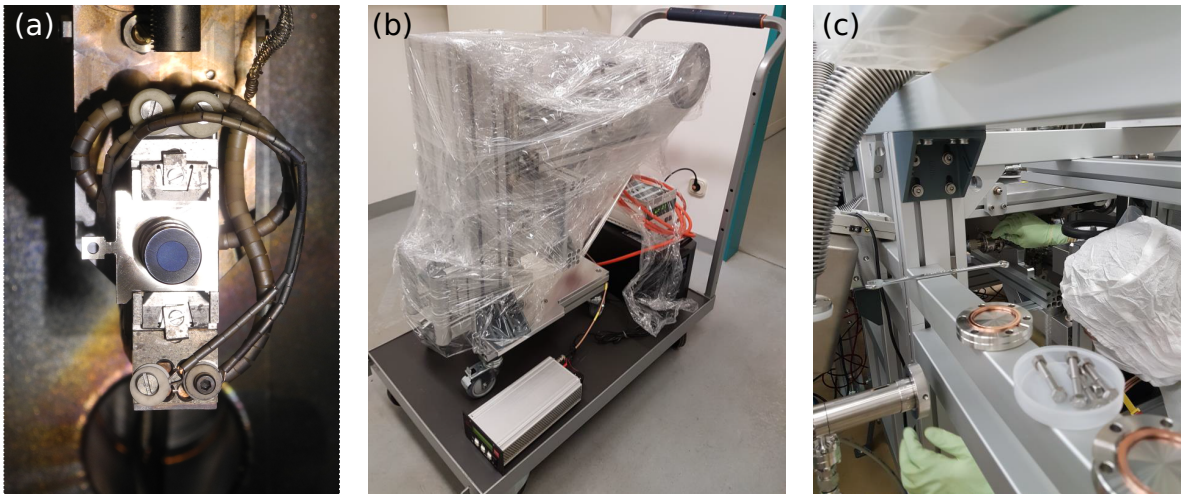

Figure 7.9.: Photocathode G002 in the preparation chamber (a). The blue circular spot on the plug surface is the deposited Cs-K-Sb layer. Transfer of the vacuum suitcase on a trolley (b) and attachment of the suitcase to transfer system 2 in a local clean room environment (c).

Critical for the heat conduction is the thermal contact between the individual parts which introduces a local resistance and can severely limit the actual power dissipation. A detailed discussion of the thermal contacts, temperature gradients and size of cross sections of these parts is beyond the scope of this work but is currently under investigation in a dedicated experiment and simulations.

7.4. Growth and Transfer of a Cs-K-Sb Cathode for the Photoinjector

In parallel to the commissioning with the copper cathode, a new cathode "G002" was prepared in the photocathode lab in order to demonstrate the transfer and application of a semiconducting high-QE cathode to the photoinjector.

A Mo plug was selected from a batch of three polished plugs by optical spectroscopy to ensure a defect free rim and smooth front surface of the plug. It was then cleaned in the cleanroom and transferred to UHV in the photocathode lab, following the steps detailed in section 4.1. Following closely the procedure for the alkali metal co-evaporation as detailed in section 4.3 a photosensitive film of Cs-K-Sb material was deposited on the cathode. In this case, it was avoided to take any XPS spectra or move the cathode unnecessarily in order to reduce the exposure to elevated vacuum pressures. The spectral response of the sample was recorded once closely after preparation and a second time before the transfer into the vacuum suitcase. The spectral

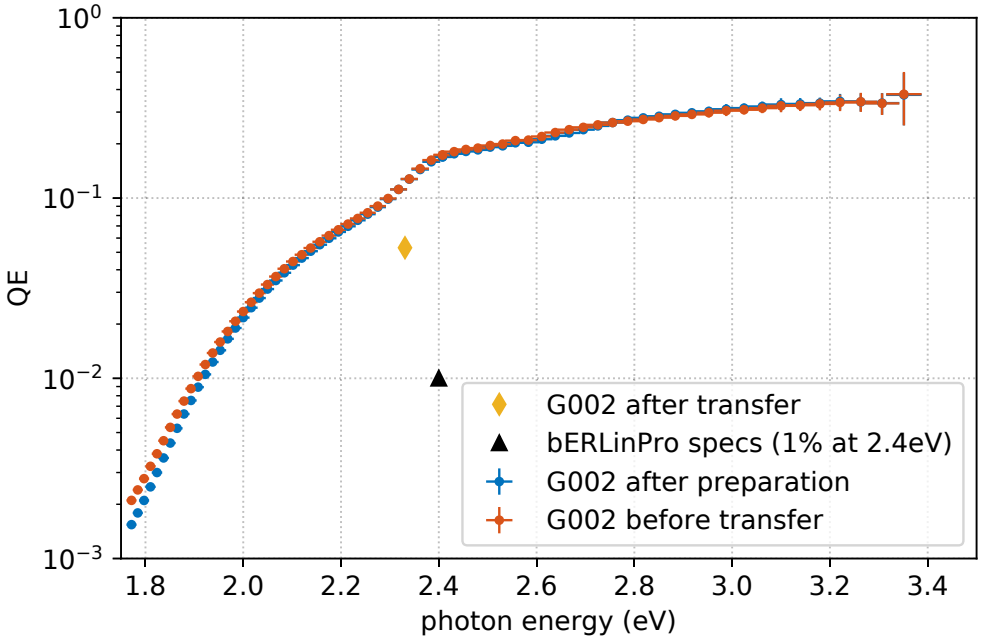

Figure 7.10.: Spectral response of sample G002. The QE after the transfer to the photoinjector as well as the bERLinPro specification are indicated.

response and final QE after the transfer is presented in Fig. 7.10. Note the very high QE of 16.8% at 2.4 eV.

The sample was transferred from the preparation chamber onto the cathode carrier in the transfer system 1 and the carrier was placed in the vacuum suitcase. A vacuum pressure of $1 \cdot 10^{-10}$ mbar could be held in transfer system 1 at rest and it did not exceed $5 \cdot 10^{-9}$ mbar during the transfer steps. Most critical in terms of pressure rise is the movement of the magnetic transfer rods and actuation of the all-metal gate valves, both have to be done slowly with feedback from a pressure gauge. The vacuum suitcase was detached and wrapped in shrink wrap within the local clean room environment in the photocathode lab. It is transported with a battery power supply to maintain the high voltage of the ion getter pump and thus sustain a pressure of $3 \cdot 10^{-11}$ mbar.

After connecting the vacuum suitcase to the transfer system at the photoinjector and pumping of the load-lock it was observed that the vacuum pressure of both transfer chamber and load-lock were insufficient to transfer the cathode. The valve was thus opened only after an additional bake-out cycle and re-activation of ion getter and NEG pumps. After the additional bake-out, the transfer was continued at a base pressure of $9 \cdot 10^{-10}$ mbar. Using a 532 nm solid state laser, the QE was measured as 5.3% in the transfer chamber (yellow diamond in Fig. 7.10).

During the cathode exchange from the Cu cathode that had been used during the commissioning to the new Cs-K-Sb cathode, it was noted however that the strong

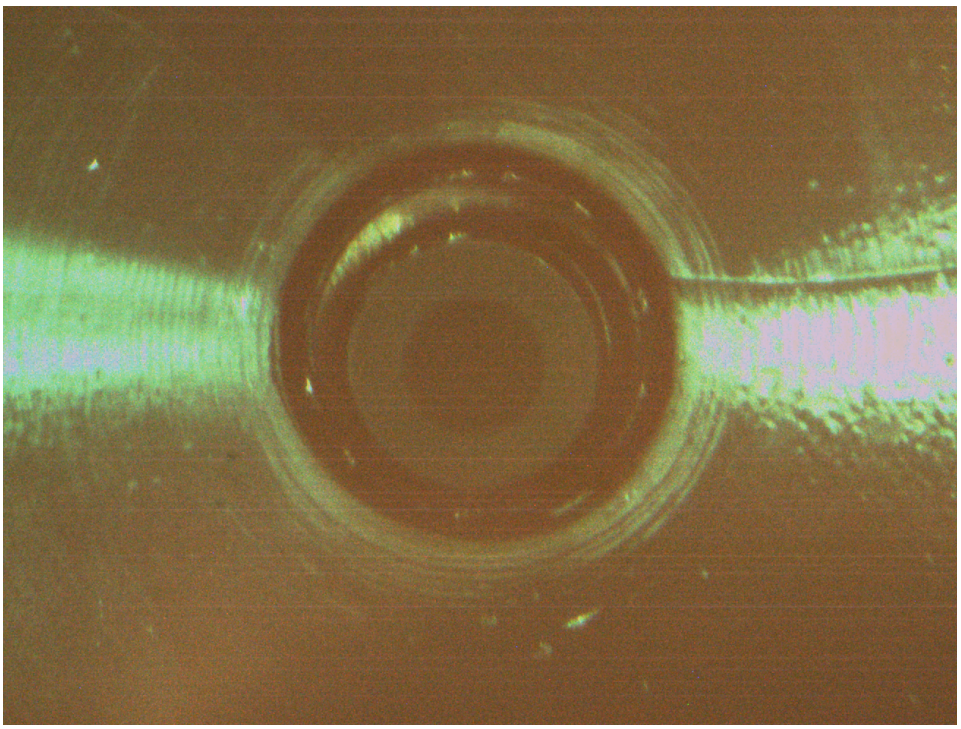

Figure 7.11.: The coated photocathode in the back wall of the SRF cavity as seen from a downstream diagnostic camera.

heat load on the copper cathode had brazed the stainless steel spring to the copper and the spring had to be torn apart in order to remove the old cathode. Despite the obvious damage to the cathode insert, the new cathode was placed on the insert, locked by the internal mechanism, and could not be removed when pulling it with the plug pincer. After discussion, it was decided to accept the risk and proceed with the Cs-K-Sb coated cathode on the damaged insert. The insert with the new cathode was moved into the RF filter using the horizontal manipulator and the bajonet lock was engaged. Figure 7.11 shows the coated cathode in the cavity as it was observed by a diagnostic camera. Unfortunately, however, the cathode plug was lost and fell into the half cell of the cavity when the transfer rod was pulled back from the insert. Thus, no RF or beam operation was possible afterwards. Nevertheless, the demonstration of the UHV transport of a high-QE cathode and the preservation of 5% QE when the cathode was placed on the insert presents an important step towards the actual operation of a Cs-K-Sb photocathode in the SRF photoinjector.

8. Conclusions and Outlook

This work was focused on the application of high QE photocathodes as electron sources for superconducting RF photoinjectors. This poses a challenge as a reliable deposition process for the cathodes needed to be developed, the high reactivity of the cathode surface requires preparation, transport and operation in ultra-high vacuum, and the interface to the superconducting RF cavity requires that the substrate and final cathode are prepared free of field-emitting particulates or defects and protrusions.

The complete process chain for the production, transport and use in the photoinjector was demonstrated. Early in the development process, Cs-K-Sb was singled out as primary candidate for the photocathode material due to the known high QE, and photoemission threshold close to the available laser wavelength which was expected to result in a low intrinsic emittance. A reproducible procedure to produce photocathodes with high QE was developed which evolves from the established three-step sequential method to a two-step alkali co-evaporation method. The new method is compared to the established one and found superior in terms of quality of the produced cathodes and stability of the process.

Considering the application in a cryogenic photoinjector this work further aimed at investigating the two relevant figures, spectral response and MTE, both at room temperature and in a cryogenic environment. For that purpose, the relative change of the QE was observed when photocathode samples were cooled by liquid nitrogen and the influence on the QE at 515 nm was found to be in the order of unity, thus allowing the application without compromise on the QE. These measurements are sidelined by wavelength and temperature dependent measurements of the mean transverse energy (MTE) obtained from a photocathode sample, albeit a similar material Cs_3Sb. The transfer of the findings from this material to Cs-K-Sb is discussed.

The necessary preparation chambers and analytical methods have been developed and commissioned specifically for this project. Especially the XPS and spectral response measurements have been set up within the scope of this work. The transverse energy measurements have been conducted at a device developed at Cornell University.

Considering the application in the bERLinPro photoinjector, work is ongoing to measure the thermal contact between photocathode plug, insert and cooler and thus to qualify the parts for a new assembly of the photoinjector. Certainly, the next step towards operation is the preparation of new photocathode samples and to repeat the cathode transfer and insertion in order to produce an electron beam from a Cs-K-Sb photocathode.

On a broader scope, a comparison of the two materials Cs-K-Sb and Na-K-Sb and their lifetime and robustness in terms of laser damage and thermal dissociation would be beneficial. The specified operation temperature of commercial Na-K-Sb photomultiplier tubes is much higher compared to Cs-K-Sb, but it remains speculative to now if this results in a greater resilience against damage due to high laser pulse energies or the average power dissipated in the photocathode.

It has been observed that very low emittances can be obtained from alkali-antimonide photocathodes when the excitation energy is close to the photoemission threshold. For technical applications, however no suitable laser medium is available at the 2.0 to 2.1 eV threshold energy of the Cs-K-Sb photocathodes. An interesting combination would be the excitation of CsSb:NaKSb photocathodes ("S20") with the fundamental radiation from a Ti:Sapphire laser at 800 nm. The CsSb:NaKSb cathodes have 10^{-5} QE at this wavelength, thus still comparable to metallic cathodes while the expected mean transverse energy is at the thermal limit of the photoemission process (25 meV).

As an overall conclusion from this work, the use of high QE photocathodes allows the c.w. operation of photoinjectors while retaining the average drive laser power in feasible limits. This is a key requirement to operate ERLs and opens the frontier to high-duty cycle operation of FELs. Two effects make the use of Cs-K-Sb photocathodes attractive especially for FELs. The reduced intrinsic emittance that is expected in comparison with Cu or Cs_2Te directly translates into higher beam brightness and thus supports the generation of higher pulse energies and shorter wavelength. At the same time, the reduced drive laser pulse energy allows for more flexibility in the optimization of the emission spot size to smaller values thus easing the optimization of the emittance evolution in the injector.

A. The Energy Scale in X-ray Photoemission Experiments

The XPS tools in the photocathode preparation and analysis system were comissioned within the scope of this thesis. After visual alignment, the position was optimized to obtain a maximum signal to noise ratio (SNR). The 3d spectrum of a cleaned and pure Ag reference sample was taken at different analyzer lens modes and pass energies to record the line width, SNR and energy calibration and finally determine a default operation mode of the instrument.

First, consider the energy levels of a sample, the spectrometer and the vacuum in between as shown in Figure A.1:

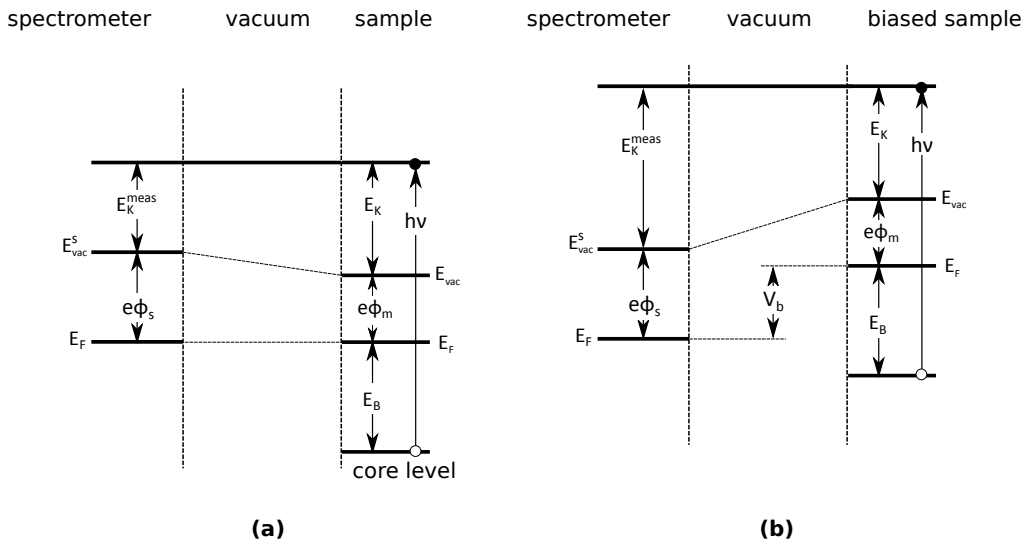

Figure A.1.: Energy levels in photoelectron spectroscopy, after [122]. (a) for a conductive sample in electrical contact with the spectrometer, (b) shows the effect of an applied bias voltage V_b. In both cases the measured kinetic energy E_K^{meas} differs from the kinetic energy after emission due to the potential difference between the sample and the spectrometer. The remaining symbols are defined in the text.

The work function $e\Phi_m$ of a surface is defined as the energy difference between the chemical potential μ inside the material and the (local) electrostatic potential energy of an electron just outside the surface $e\Phi_{vac} \equiv E_{vac}$.

$$e\Phi_m \equiv -E_{vac} - \mu \tag{A.1}$$

This energy level is local because the vacuum electrostatic potential varies in the spectrometer due to the contact potential of the different materials. The common reference E_0 is the vacuum level of an electron at rest in infinite distance. The electrostatic potential in the material is the difference between $E_0 \equiv 0$ and the Fermi-level, thus

$$E_0 - E_F = -\mu \tag{A.2}$$
$$e\Phi_m = E_{vac} - E_F \tag{A.3}$$

The kinetic energy of an electron liberated from an energy-level with binding energy E_B below the Fermi level is

$$E_K = h\nu - E_B - e\Phi_m \tag{A.4}$$

but the kinetic energy measured by the spectrometer is shifted by $\Delta\Phi = (\Phi_m - \Phi_s)$ due to the different local vacuum levels. It follows that

$$E_K^{meas} = h\nu - E_B - e\Phi_m + e\Delta\Phi = h\nu - E_B - e\Phi_s \tag{A.5}$$

and the measured kinetic energy is independent of the sample's work function.

Energy Calibration

As a reference sample, a silver sheet (99.99%) was obtained from Sigma-Aldrich. The sample was rinsed with Isopropyl alcohol and Acetone, in UHV it was heated to 150°C and sputter cleaned by an Ar^+ ion beam at 3 keV ($p_{Ar} = 5 \cdot 10^{-6}$ mbar, I_{emi} = 10 mA) for 30 min to remove surface oxides and carbon contamination.

A survey spectrum was taken to ensure the cleanliness of the sample and correct orientation (i.e. no contribution from the sample holder or screws). The spectrum is displayed in Figure A.2. There are no oxygen (O 1s at 532 eV) or carbon (C 1s at 285 eV) impurities visible.

The Ag 3d spectrum was taken at different lens modes and pass energies to determine the instrument resolution, SNR and energy calibration. The energy calibration was previously done by SPECS and the measured peak position were found to agree very well (within 0.1 eV) with literature values [65]. The resolution of the instrument can be determined from the line width of the measured peaks. The measured width (FWHM) is a convolution of the energy width of the exciting radiation ΔE_x, the energy

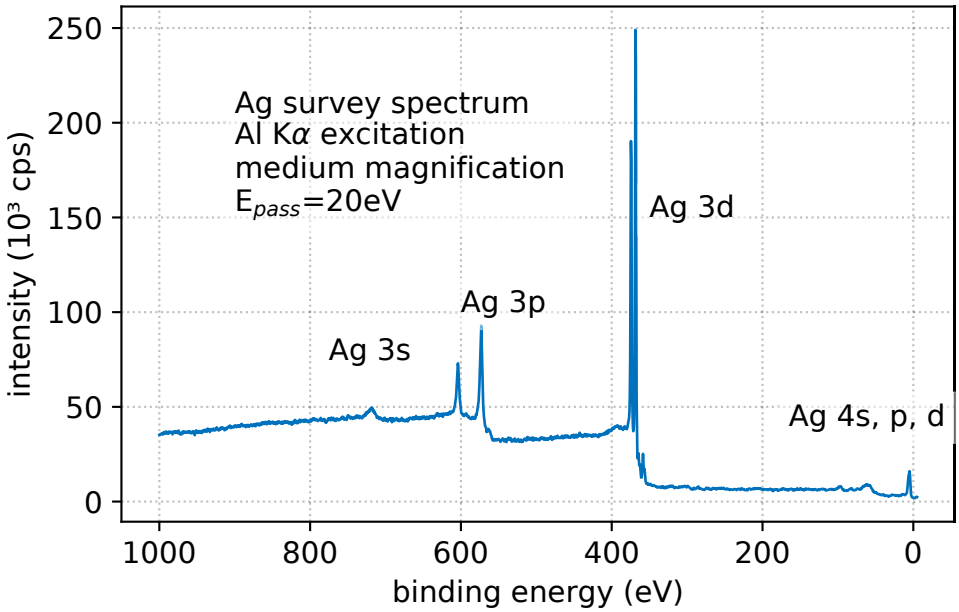

Figure A.2.: Survey spectrum of the Ag reference sample as obtained during the alignment.

resolution of the electron analyzer ΔE_A which depends on the energy window or pass energy, and the physical line width ΔE_2 of the electronic state in the sample

$$\Delta E = \left(\Delta E_x^2 + \Delta E_A^2 + \Delta E_2^2\right)^{1/2} \tag{A.6}$$

Figure A.3 shows one measured Ag 3d spectrum. The spin split 5/2 and 3/2 states are annotated. In order to determine the FWHM width for one set of measurement parameters, the background was estimated by the Shirley method and subtracted, and the 3d 5/2 peak was fitted with a Voigt profile.

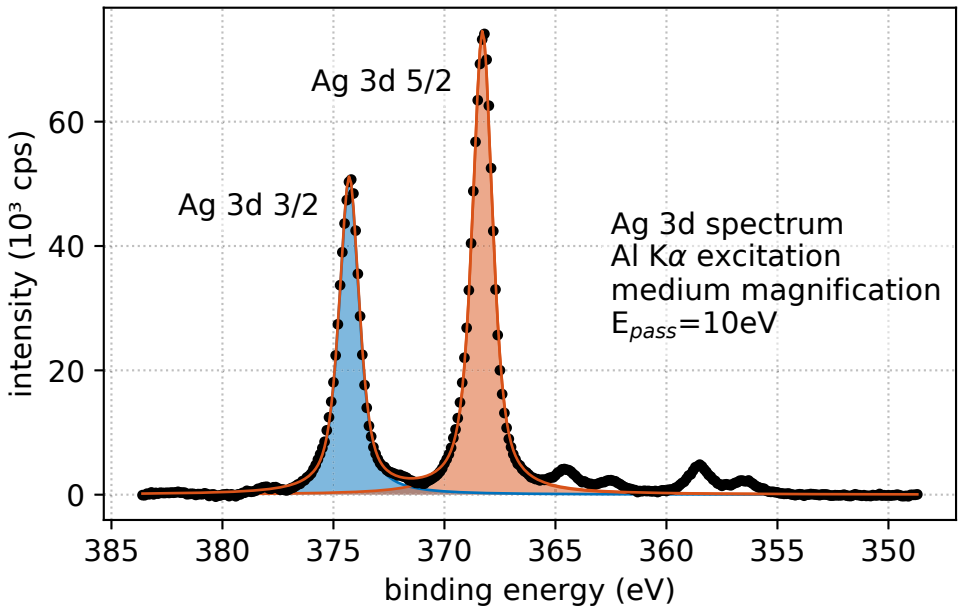

Figure A.3.: Ag 3d spectrum of the Ag reference sample.

As can be seen in Figure A.4, the energy resolution depends on the selected X-ray anode. Within the selected range of pass energies, the contribution from ΔE_A rises linearly with the pass energy at a slope of (average) 0.0186 ± 0.001 eV/eV. The contributions from the X-ray anode are constant and amount to 0.70 eV and 0.85 eV for the Mg Kα and Al Kα line, respectively [123]. The measured constant part (intercept with zero pass energy) of 0.78(1) eV and 0.93(1) eV originates from the convolution of the natural line width of the Ag 3d 5/2 transition of 0.33 eV [65, 124] with the X-ray line width and dominates the resolution of the measurement.

One may conclude that only a moderate additional uncertainty of 0.37 eV is introduced by taking survey spectra at 20 eV pass energy and 0.19 eV by taking fine spectra of individual transition at 10 eV pass energy. These settings in the medium magnification mode were chosen as standard operating modes throughout this work, unless otherwise noted. Generally, despite its larger line width, the Al anode is employed due its more common use and the higher availability of reference data for this excitation energy.

The magnification lens modes image the sample surface plane to the entrance plane of the analyzer and thus define the spatial acceptance area to first order as slit width divided by magnification factor. The factor is 2, 5, and 10 for the low, medium and, high magnification mode. Here, the medium magnification was used together with a 7 mm entrance slit of the analyzer resulting in a 1.4 mm diameter of the analyzed area. The spot size of the X-ray source is larger than this area, thus, the analyzer settings limit the analyzed area and define a sharp circumference. An iris aperture

in the first diffraction plane of the lens system can be adjusted between 50 mm and 1 mm diameter which defines the angular acceptance of the electron transport. In this work, all measurements were taken with the iris set to 15 mm resulting in an angular acceptance of ±5°.

In summary the standard operating mode for the XPS instruments is to run the X-ray source at 12.5 kV accelerating voltage and 20 mA emission current on the Al anode and setting the analyzer to medium magnification mode with a 7x20 mm entrance slit, 15 mm iris and 20 or 10 eV pass energy, depending on the resolution required. The selected settings are a reasonable compromise between resolution and electron count rate. Typical peak heights over background are $75 \cdot 10^3$ cps for prominent peaks. Further restriction of the apertures would not lead to drastic improvement of the resolution which is limited by the line width of the non-monochromatized source. Survey spectra in this work are taken at 1 eV steps with 0.1 s exposure time and fine spectra are taken at 0.1 eV steps with 1 s exposure time.

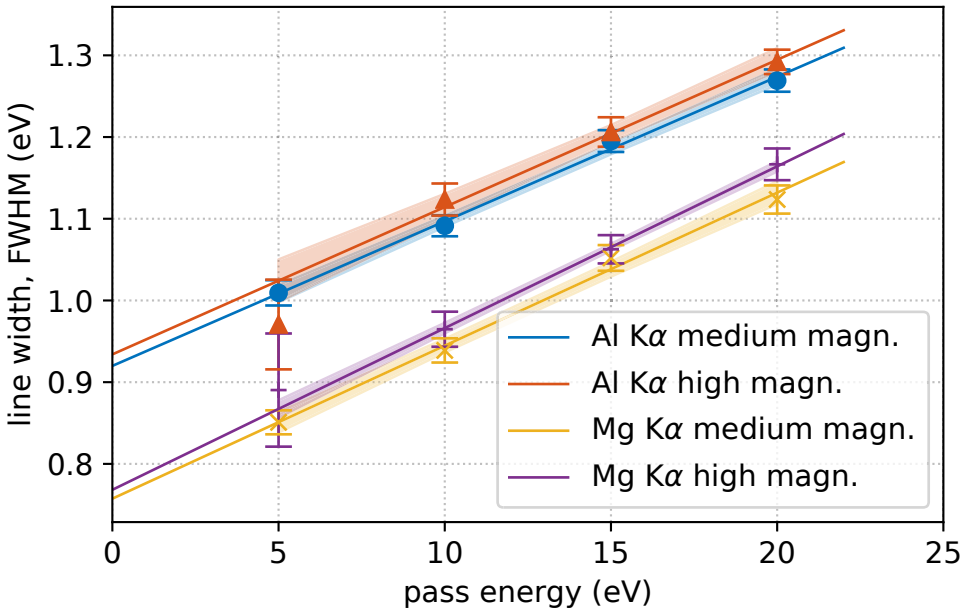

Figure A.4.: Line width (FWHM) of the Ad 3d 5/2 peak obtained using the medium and high magnification lens modes. A fit to a linear model with $1\,\sigma$ confidence bands is displayed.

B. Complete Data of the XPS Stoichiometry Results

For the sake of completeness, the data of the stoichiometry analysis from the XPS data is presented here, including the samples that have been eliminated from the discussion in chapter 4.

Sample P003 has been excluded because it is a Cs-Sb sample.

Sample P005 has been excluded because it shows extreme oxygen contamination due to excess heating of the alkali sources.

Samples P010 and P012 have been excluded because they have not fully reacted with the alkali metals, due to misalignment in the case of P010 and empty sources in the case of P012.

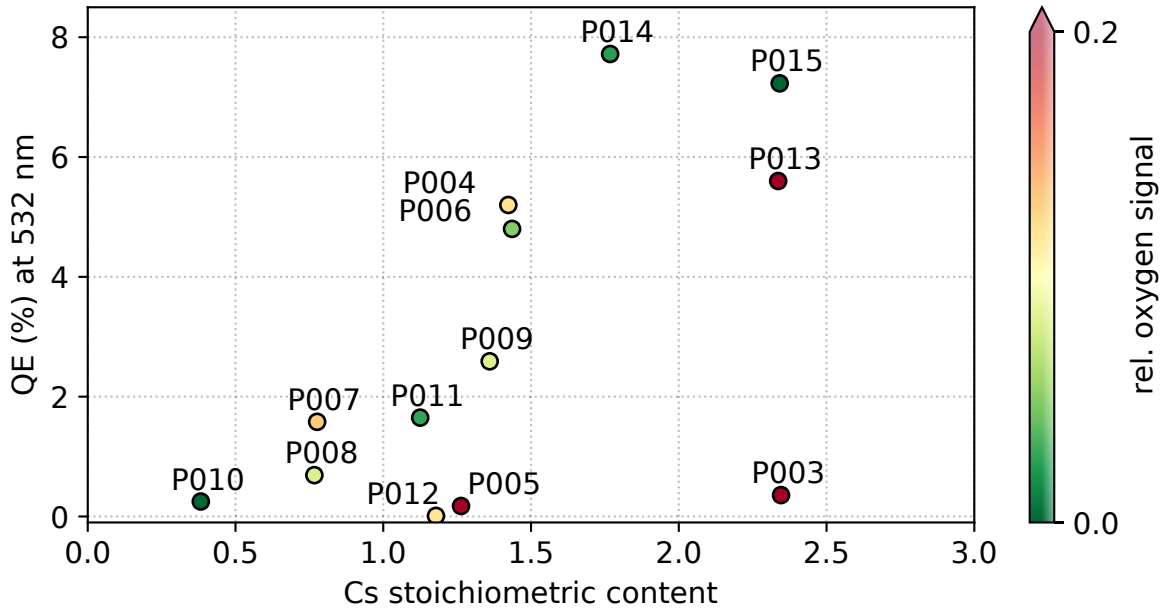

Figure B.1.: Correlation of QE with Cs stoichiometric content.

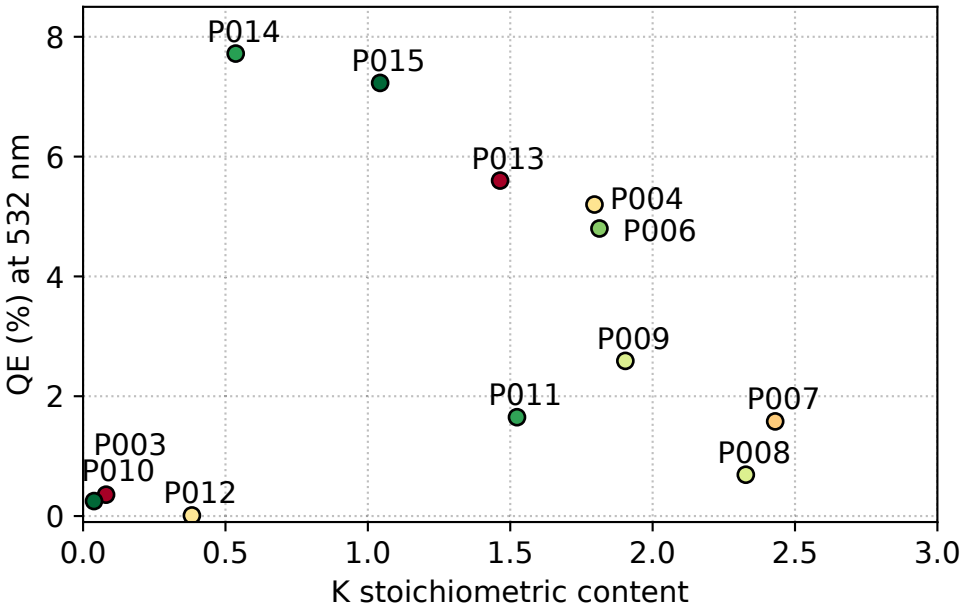

Figure B.2.: Correlation of QE with K stoichiometric content.

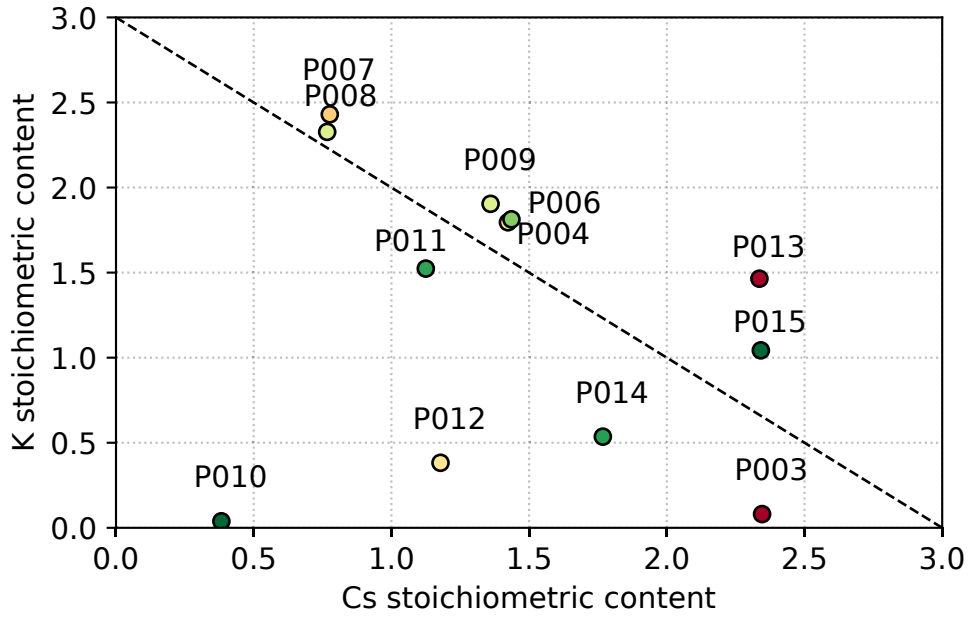

Figure B.3.: Scattering of the stoichiometric content of the individual alkali constituents. The black dashed line represents the $x + y = 3$ case.

C. Photocurrent Obtained from the Cryo-cooled Photocathode Samples

For reference, the phtocurrent data collected during the cooling cycles of the samples P013 and P016 is displayed:

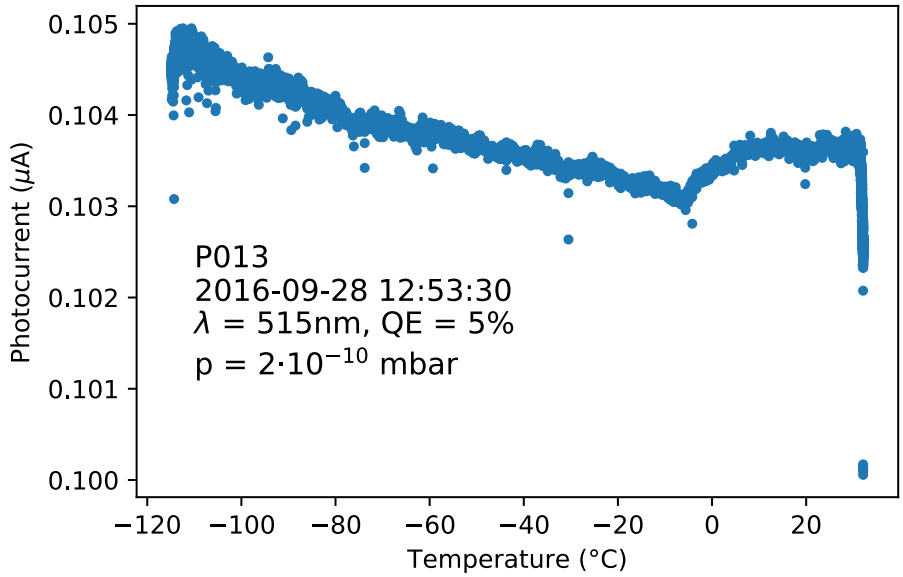

Figure C.1.: Photocurrent measured from sample P013 during cryogenic cooling.

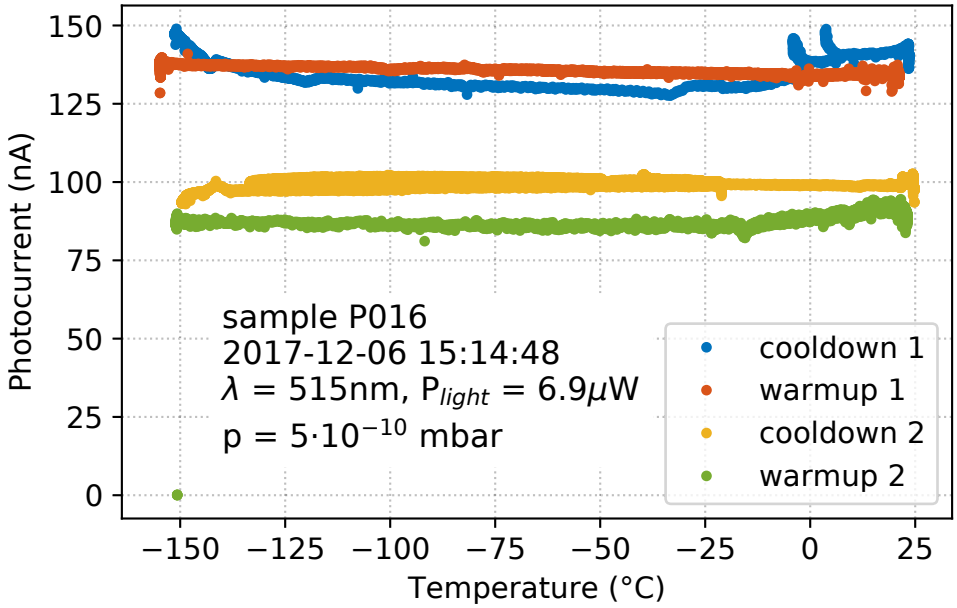

Figure C.2.: Photocurrent measured from sample P016 during cryogenic cooling.

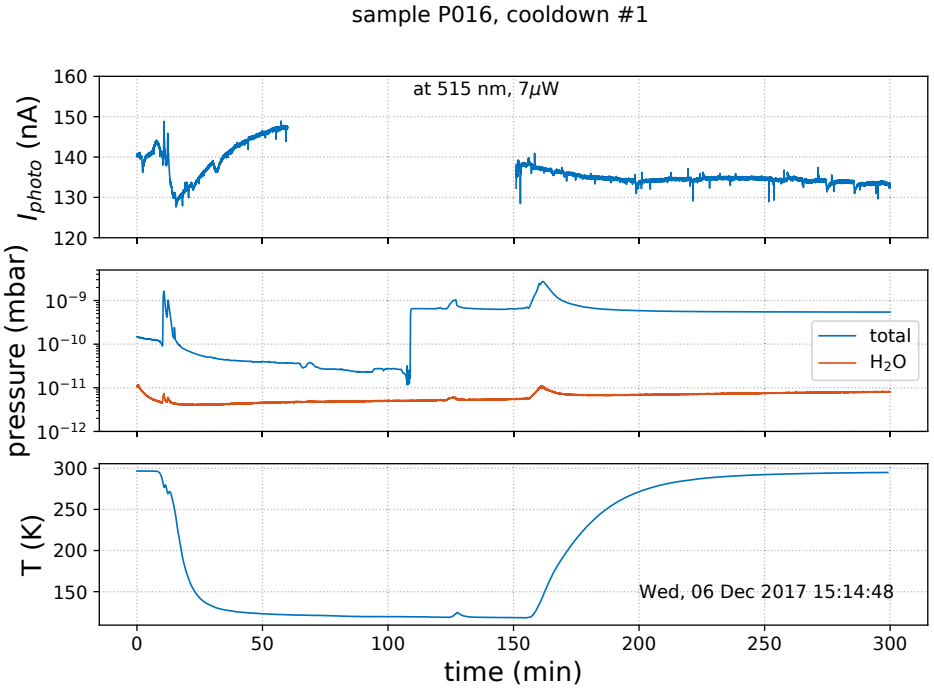

Figure C.3.: Exemplary data for the procedure of a cooling and warm-up cycle at constant illumination intensity and wavelength. The gap in the photocurrent measurement is due to a spectral response measurement at low temperature. Several quick temperature ramps do not correlate with significant changes in the observed photocurrent.

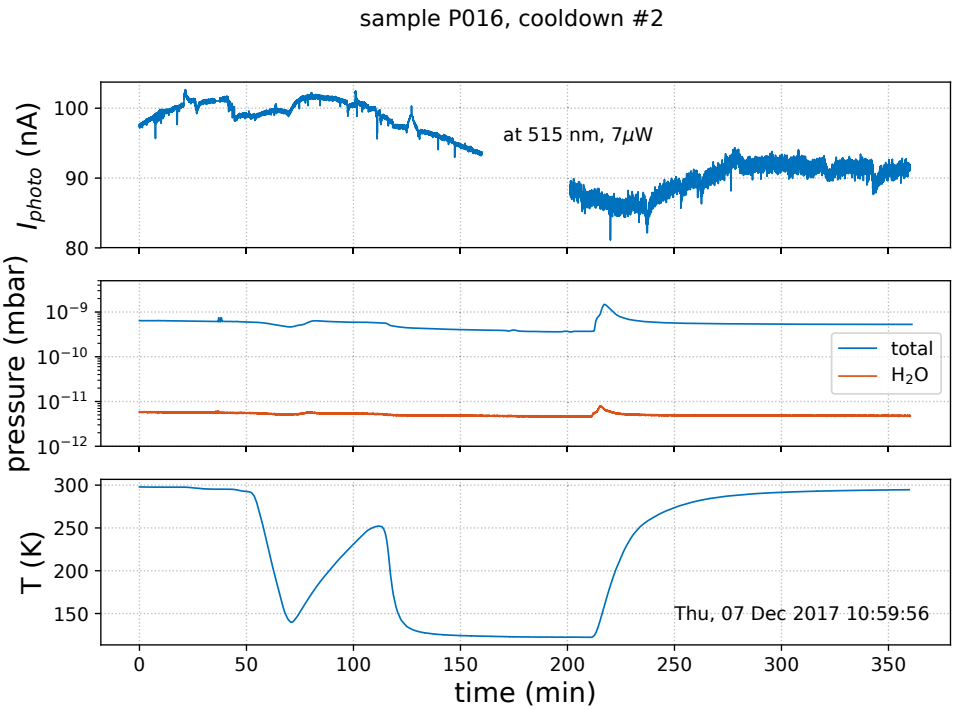

Figure C.4.: Same as above for a second cycle.

Reports from Other Labs

Measurements of a loss of QE from K2CsSb Cathodes have been reported by Erdong Wang, BNL [108] at the ERL Workshop 2015.

Figure C.5 shows the QE behavior during three different cooldown cycles with different cooling speeds.

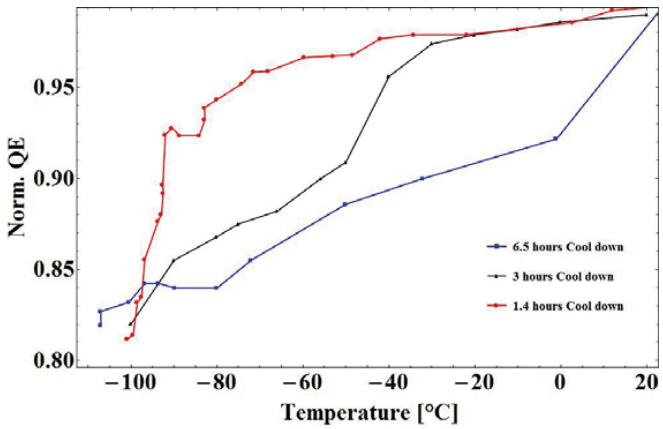

Figure C.5.: Cooling cycles tested at BNL, QE at 532 nm. [108]

All cycles are between room temperature and -100°C, and the QE of the cold cathode is about 82% of the initial value. We assume that these measurements have been performed in the SRF gun but the vacuum pressure or partial pressures of reactive gases are not quoted.

A recovery of the degraded QE up to the initial value is reported when the sample was warmed up to room temperature again.

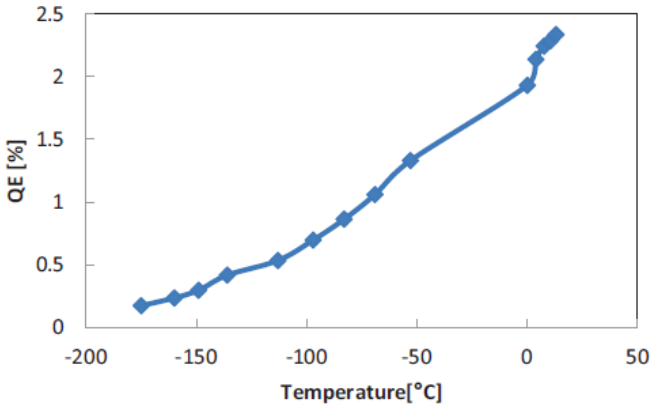

Figure C.6.: Recovery of cathode's QE during warmup at BNL. [108]

Measurements presented by Taro Konomi, KEK [109] in the seminar Beschleunigerphysik indicate a loss of QE of a factor of 5 when the sample is cooled to 100 K. The QE remains stable during further cooling down to 6 K. The authors assume that the degradation is due to residual gas adsorbing on the sample surface, the vacuum pressure during the measurement was 10^{-9} mbar. The wavelength for these measurements is not stated.

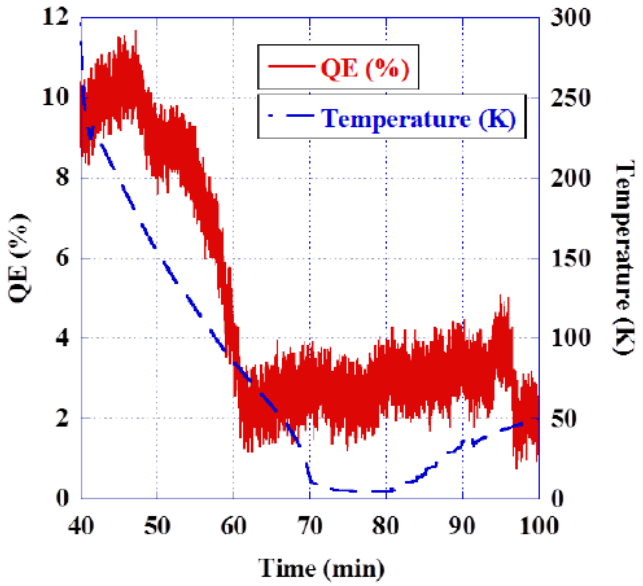

Figure C.7.: Cooldown behaviour at KEK. [109]

D. Fowler's photoemission theory

The central assumption in Fowler's theory [125, 126] is that the current density of photoemitted electrons is directly proportional to the number of available electrons, for which the condition

$$\frac{mu^2}{2} + hv = \mu + \Phi \tag{D.1}$$

is fulfilled, i.e. the kinetic energy in the direction u normal to the surface is higher than the potential step at the surface.

Following the notation of [127], one starts from Fermi-Dirac distribution of electron momenta in Fermi-Sphere (Sommerfeld model of metals)

$$n(u,v,w)\,\mathrm{d}u\mathrm{d}v\mathrm{d}w = 2\left(\frac{m}{h}\right)^3 \frac{\mathrm{d}u\mathrm{d}v\mathrm{d}w}{e^{\left[\frac{\mathrm{m}}{2}\left(\mathrm{u}^2+\mathrm{v}^2+\mathrm{w}^2\right)-\mu\right]/\mathrm{k_B T}+1}}, \tag{D.2}$$

which is then integrated over v and w to obtain the distribution of momenta normal to the surface

$$n(u)\,\mathrm{d}u = \frac{4\pi k_\mathrm{B} T}{m}\left(\frac{m}{h}\right)^3 \log\left[1 + e^{\left(\mu-\mathrm{mu}^2/2\right)/\mathrm{k_B T}}\right]\mathrm{d}u. \tag{D.3}$$

Thus, the total number of available electrons is given by

$$N = \int_{\frac{1}{2}\mathrm{mu}^2=\phi-\mathrm{hv}}^{\infty} n(u)\,\mathrm{d}u \tag{D.4}$$

$$= \frac{2\pi k_\mathrm{B} T}{m}\left(\frac{2kT}{m}\right)^{1/2}\left(\frac{m}{h}\right)^3 \int_0^\infty \frac{\log(1+e^{-\mathrm{y}+(\mathrm{hv}-\phi)/\mathrm{k_B T}})}{(y+(\phi-hv)/k_\mathrm{B}T)^{1/2}}\,\mathrm{d}y, \tag{D.5}$$

and by substituting $y = \frac{1}{2}mu^2$ and making the approximation that y can be neglected in $(y + (\phi - hv)/k_\mathrm{B}T)^{1/2}$ when hv is near the photoemission threshold,

$$N = \frac{\pi(2m)^{3/2}}{h^3}\frac{k^2T^2}{(\phi-hv)^{1/2}}\int_0^\infty \log\left(1+e^{-\mathrm{y}+(\mathrm{hv}+\phi)/\mathrm{k_B T}}\right)\mathrm{d}y \tag{D.6}$$

The integrand in equation D.6 has no simple closed-form solution but can be approximated by an expansion around the small parameter $\eta = (hv - \Phi)/k_\mathrm{B}T$ and then integrated term by term.

One obtains

$$I = C\frac{T^2}{(\mu + \Phi - h\nu)^{1/2}}F(\eta) \tag{D.7}$$

where C is a material-dependent constant that is independent from $h\nu$, T, and Φ and $F(\eta)$ is known as the Fowler function:

$$F(\eta) = \quad e^{\eta} - \frac{e^{2\eta}}{2^2} + \frac{e^{3\eta}}{3^2} - ... \qquad \eta \leq 0 \tag{D.8}$$

$$F(\eta) = \quad \frac{\pi^2}{6} + \frac{\eta^2}{2} - \left(e^{-\eta} - \frac{e^{-2\eta}}{2^2} + ...\right) \qquad \eta > 0 \tag{D.9}$$

In addition to Fowlers theory, a similar treatment was published by DuBridge [126], who obtained the distribution of the total energy of electrons as

$$f_{\mathrm{t}}(E)\mathrm{d}E = A_{\mathrm{t}}\frac{E\mathrm{d}E}{e^{(\mathrm{E}-\mathrm{E_m})/\mathrm{k_B}\mathrm{T}} + 1} \tag{D.10}$$

and the surface normal energy distribution, as observed e.g. in a parallel plate experiment, as

$$f_{\mathrm{n}}(E)\mathrm{d}E = A_{\mathrm{n}}\log\left(e^{(\mathrm{E}-\mathrm{E_m})/\mathrm{k_B}\mathrm{T}} + 1\right)\mathrm{d}E. \tag{D.11}$$

The two distribution curves f_{t} and f_{n} as a function of kinetic energy are shown in Figure D.1 together with the current-voltage curve (yield) in units of the work function.

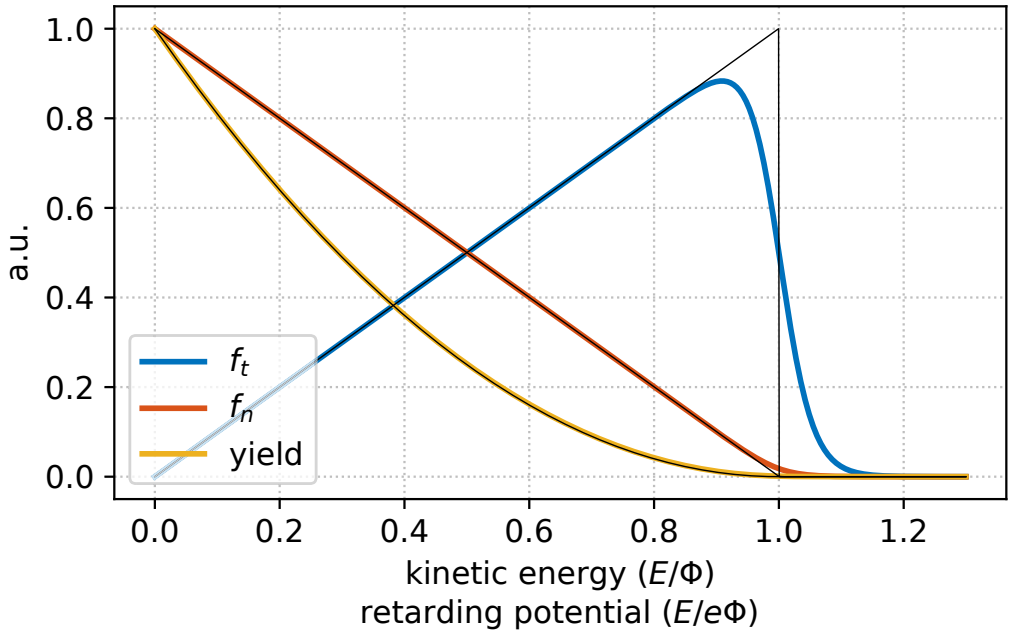

Figure D.1.: Distribution curves of the surface normal and total kinetic energy of photoelectrons as obtained from the DuBridge theory at 300 K. The current-voltage curve as would be observed in a parallel plate experiment is shown with the curves. Both energy and voltage scale are in units of the work function. The thin black lines represent the case at 0 K.

List of Figures

Bibliography

[1] T. Rao and D. H. Dowell, *An Engineering Guide To Photoinjectors*, ed. by T. Rao and D. H. Dowell, 2014, ISBN: 978-1481943222, arXiv: 1403.7539.

[2] P. Musumeci et al., *Advances in bright electron sources*, in: Nuclear Instruments and Methods in Physics Research Section A: Accelerators, Spectrometers, Detectors and Associated Equipment 907 (2018), pp. 209–220, DOI: 10.1016/j.nima.2018.03.019.

[3] M. Vogt et al., *Status of the free-electron laser user facility FLASH*, in: Proceedings of IPAC 2014, pp. 938–940, URL: http://accelconf.web.cern.ch/AccelConf/SRF2009/papers/mooaau01.pdf.

[4] P. G. O'Shea and H. P. Freund, *Free-Electron Lasers: Status and Applications*, in: Science 292 (2001), pp. 1853–1858, DOI: 10.1126/science.1055718.

[5] G. Sciaini and R. J. D. Miller, *Femtosecond electron diffraction: heralding the era of atomically resolved dynamics*, in: Reports on Progress in Physics 74 (2011), p. 096101, DOI: 10.1088/0034-4885/74/9/096101.

[6] K. Pepitone et al., *The electron accelerators for the AWAKE experiment at CERN - Baseline and Future Developments*, in: Nuclear Instruments and Methods in Physics Research Section A: Accelerators, Spectrometers, Detectors and Associated Equipment 909 (2018), pp. 102–106, DOI: 10.1016/J.NIMA.2018.02.044.

[7] N. Brodusch, H. Demers, and R. Gauvin, *Developments in Field Emission Gun Technologies and Advanced Detection Systems*, Springer, Singapore, 2018, ISBN: 978-981-10-4432-8, DOI: 10.1007/978-981-10-4433-5_2.

[8] W. Engelen et al., *Effective temperature of an ultracold electron source based on near-threshold photoionization*, in: Ultramicroscopy 136 (2014), pp. 73–80, DOI: 10.1016/j.ultramic.2013.07.017, arXiv: 1309.3417.

[9] M. Abo-Bakr et al., *Status Report of the Berlin Energy Recovery Linac Project bERLinPro*, in: Proceedings of IPAC 2018 THPMF034 (2018), pp. 1827–1830, DOI: 10.18429/JACoW-IPAC2018-THPMF034.

[10] M. A. H. Schmeißer et al., *Towards the operation of Cs-K-Sb photocathodes in superconducting rf photoinjectors*, in: Physical Review Accelerators and Beams 21 (2018), p. 113401, DOI: 10.1103/PhysRevAccelBeams.21.113401.

[11] M. Reiser, *Theory and Design of Charged Particle Beams*, Wiley Series in Beam Physics and Accelerator Technology, Weinheim, Germany: Wiley-VCH Verlag GmbH & Co. KGaA, 2008, ISBN: 9783527622047, DOI: 10.1002/9783527622047.

[12] I. V. Bazarov, B. M. Dunham, and C. K. Sinclair, *Maximum Achievable Beam Brightness from Photoinjectors*, in: Physical Review Letters 102 (2009), p. 104801, DOI: 10.1103/PhysRevLett.102.104801.

[13] W. Spicer, *Photoemissive, Photoconductive, and Optical Absorption Studies of Alkali-Antimony Compounds*, in: Physical Review 112 (1958), pp. 114–122, DOI: 10.1103/PhysRev.112.114.

[14] M. Schmeißer, *In-situ measurements of the intrinsic emittance of photocathodes for high brightness electron beams*, Master's Thesis, Humboldt-University of Berlin, 2014, DOI: 10.13140/RG.2.1.5113.4481.

[15] W. E. Spicer and A. Herrera-Gómez, *Modern Theory and Applications of Photocathodes*, in: SPIE's 1993 Interantional Symposium on Optics, Imaging and Instrumentation.

[16] D. H. Dowell et al., *In situ cleaning of metal cathodes using a hydrogen ion beam*, in: Physical Review Special Topics - Accelerators and Beams 9 (2006), p. 063502, DOI: 10.1103/PhysRevSTAB.9.063502.

[17] D. H. Dowell et al., *Cathode R&D for future light sources*, in: Nuclear Instruments and Methods in Physics Research, Section A 622 (2010), pp. 685–697, DOI: 10.1016/j.nima.2010.03.104.

[18] I. Bazarov et al., *Thermal emittance measurements of a cesium potassium antimonide photocathode*, in: Applied Physics Letters 98 (2011), p. 224101, DOI: 10.1063/1.3596450.

[19] S. Karkare et al., *Monte Carlo charge transport and photoemission from negative electron affinity GaAs photocathodes*, in: Journal of Applied Physics 113 (2013), p. 104904, DOI: 10.1063/1.4794822.

[20] H. Xie et al., *Experimental measurements and theoretical model of the cryogenic performance of bialkali photocathode and characterization with Monte Carlo simulation*, in: Physical Review Accelerators and Beams 19 (2016), p. 103401, DOI: 10.1103/PhysRevAccelBeams.19.103401.

[21] P. Gupta, L. Cultrera, and I. Bazarov, *Monte Carlo simulations of electron photoemission from cesium antimonide*, in: Journal of Applied Physics 121 (2017), p. 215702, DOI: 10.1063/1.4984263.

[22] R. Nathan and C. H. B. Mee, *Photoelectric and Related Properties of the Potassium—Antimony—Caesium Photocathode*, in: International Journal of Electronics 23 (1967), pp. 349–354, DOI: 10.1080/00207216708961542.

[23] S.-H. Wei and A. Zunger, *Electronic structure of M3Sb-type filled tetrahedral semiconductors*, in: Physical Review B 35 (1987), pp. 3952–3961, DOI: 10.1103/PhysRevB.35.3952.

[24] A. R. H. F. Ettema and R. A. de Groot, *Bandstructure calculations of the hexagonal and cubic phases of K3Sb*, in: Journal of Physics: Condensed Matter 11 (1999), pp. 759–766, DOI: 10.1088/0953-8984/11/3/015.

[25] A. R. H. F. Ettema and R. A. de Groot, *Electronic structure of Cs2KSb and K2CsSb*, in: Physical Review B 66 (2002), p. 115102, DOI: 10.1103/PhysRevB.66.115102.

[26] L. Kalarasse, B. Bennecer, and F. Kalarasse, *Optical properties of the alkali antimonide semiconductors Cs3Sb, CsK2Sb, and K3Sb*, in: Journal of Physics and Chemistry of Solids 71 (2010), pp. 314–322, DOI: 10.1016/j.jpcs.2009.12.083.

[27] G. Murtaza et al., *Structural, elastic, electronic and optical properties of bi-alkali antimonides*, in: Bulletin of Materials Science 39 (2016), pp. 1581–1591, DOI: 10.1007/s12034-016-1300-1.

[28] J. Smedley, T. Rao, and E. Wang, *K2CsSb Cathode Development*, in: AIP Conference Proceedings 1149, 18th International Spin Physics Symposium (2009), pp. 1062–1066.

[29] S. Schreiber et al., *Photocathodes at FLASH*, in: Proceedings of IPAC 2012, New Orleans, Louisiana, USA, pp. 625–627, URL: http://accelconf.web.cern.ch/Accelconf/IPAC2012/papers/moppp029.pdf.

[30] E. D. Palik, *Handbook of Optical Constants of Solids*, 3rd ed., Elsevier, 1985, ISBN: 9780125444200.

[31] M. N. Polyanskiy, *Refractive index database*, URL: http://refractiveindex.info (visited on 09/21/2018).

[32] F. Zhou et al., *High-brightness electron beam evolution following laser-based cleaning of a photocathode*, in: Physical Review Special Topics - Accelerators and Beams 15 (2012), p. 090703, DOI: 10.1103/PhysRevSTAB.15.090703.

[33] J. Teichert et al., *Experiences with the SRF Gun II for User Operation at the ELBE Radiation Source*, in: Proceedings of IPAC 2018, Vancouver, BC, Canada, pp. 4145–4147, DOI: 10.18429/JACoW-IPAC2018-THPMF040.

[34] R. Xiang et al., *Study of Magnesium Photocathodes for Superconducting RF Photoinjectors*, in: Proceedings of IPAC 2018, 13, Vancouver, BC, Canada, pp. 4142–4144, DOI: 10.18429/JACoW-IPAC2018-THPMF039.

[35] M. A. H. Schmeißer et al., *Results from Beam Commissioning of an SRF Plug-gun Cavity Photoinjector*, in: Proceedings of IPAC 2013, pp. 282–284, URL: https://accelconf.web.cern.ch/AccelConf/IPAC2013/papers/mopfi002.pdf.

[36] M. A. H. Schmeißer, *Emittance Measurements of a Superconducting High Frequency Electron Gun*, Forschungsbeleg, 2013, arXiv: 1307.3488.

[37] A. Neumann et al., *Towards a 100mA Superconducting RF Photoinjector for bERLinPro*, in: Proceedings of SRF 2013, pp. 42–49, URL: http://ipnweb.in2p3.fr/srf2013/papers/moiob02.pdf.

[38] D. H. Dowell, *Sources of Emittance in Photocathode RF Guns: Intrinsic emittance, space charge forces, RF and solenoid effects*, tech. rep., 2016, arXiv: 1610.01242.

[39] M. Scholz *et al.*, *FEL Performance Achieved at the European XFEL*, in: Proceedings of IPAC 2018, pp. 29–33, DOI: 10.18429/JACoW-IPAC2018-MOZGBD2.

[40] S. Lederer and S. Schreiber, *Cs2Te Phtocathode Lifetime at FLASH and European XFEL*, in: Proceedings of IPAC 2018, pp. 2496–2498, DOI: 10.18429/JACoW-IPAC2018-WEPMF056.

[41] M. Vogt et al., *Status of the Soft X-Ray Free Electron Laser Flash*, in: Proceedings of IPAC 2017, p. 2628, DOI: 10.18429/JACoW-IPAC2017-WEPAB025.

[42] Klaus Flöttmann, *Note on the thermal emittance of electrons emitted by Cesium Telluride photo cathodes*, tech. rep., DESY, TESLA FEL-Report 1997-1, 1997, URL: http://flash.desy.de/sites2009/site%7B%5C_%7Dvuvfel/content/e403/e1642/e839/e829/infoboxContent830/tesla-fel1997-01.pdf (visited on 11/27/2018).

[43] M. Lay, *Parameterisation of the angular response of the R1408 Hamamatsu eight-inch photomultiplier tube to be used in the Sudbury Neutrino Observatory*, in: Nuclear Instruments and Methods in Physics Research, Section A 383 (1996), pp. 485–494, DOI: 10.1016/S0168-9002(96)00860-1.

[44] A. Menegolli et al., *Measurement of photocathode spectral response at cryogenic temperature*, in: Nuclear Instruments and Methods in Physics Research, Section A 572 (2007), pp. 446–448, DOI: 10.1016/j.nima.2006.10.209.

[45] A. H. Sommer, *Characteristics of Evaporated Antimony Films as a Function of the Antimony Source*, in: Journal of Applied Physics 37 (1966), pp. 2789–2791, DOI: 10.1063/1.1782124.

[46] A. H. Sommer and W. H. McCarroll, *A new modification of the semiconducting compound K3Sb*, in: Journal of Applied Physics 37 (1966), pp. 174–179, DOI: 10.1063/1.1707801.

[47] A. H. Sommer, *Photoemissive Materials*, New York: John Wiley & Sons, Inc., 1968, ISBN: 0471813001.

[48] D. Filippetto et al., *Maximum current density and beam brightness achievable by laser-driven electron sources*, in: Physical Review Special Topics - Accelerators and Beams 17 (2014), p. 024201, DOI: 10.1103/PhysRevSTAB.17.024201.

[49] J. Völker, *Development of a compact test facility for SRF Photoelectron injectors*, PhD thesis, Humboldt-Universität zu Berlin, 2017, DOI: 10.18452/19322.

[50] S. Karkare and I. Bazarov, *Effect of nanoscale surface roughness on transverse energy spread from GaAs photocathodes*, in: Applied Physics Letters 98 (2011), p. 094104, DOI: 10.1063/1.3559895.

[51] G. Gevorkyan et al., *Effects of physical and chemical surface roughness on the brightness of electron beams from photocathodes*, in: Physical Review Accelerators and Beams 21 (2018), p. 93401, DOI: 10.1103/PhysRevAccelBeams.21.093401.

[52] T. Vecchione et al., *Effect of roughness on emittance of potassium cesium antimonide photocathodes*, in: pp. 655–657, URL: http://accelconf.web.cern.ch/accelconf/IPAC2012/papers/moppp041.pdf.

[53] H. J. Qian et al., *Experimental investigation of thermal emittance components of copper photocathode*, in: Physical Review Special Topics - Accelerators and Beams 15 (2012), p. 040102, DOI: 10.1103/PhysRevSTAB.15.040102.

[54] R. R. Mammei et al., *Charge lifetime measurements at high average current using a K2CsSb photocathode inside a dc high voltage photogun*, in: Physical Review Special Topics - Accelerators and Beams 16 (2013), p. 033401, DOI: 10.1103/PhysRevSTAB.16.033401.

[55] J. Kühn et al., *UHV Photocathode Plug Transfer Chain for the bERLinPro SRF-Photoinjector*, in: Proceedings of IPAC 2017, Copenhagen, Denmark, DOI: 10.18429/JACoW-IPAC2017-TUPAB029, URL: http://accelconf.web.cern.ch/AccelConf/ipac2017/papers/tupab029.pdf.

[56] Paolo della Porta and Elio Rabusin, *US Patent 3578834: Generation of alkali metals*, 1969, URL: http://patft.uspto.gov/netacgi/nph-Parser?Sect1=PTO1&Sect2=HITOFF&d=PALL&p=1&u=%2Fnetahtml%2FPTO%2Fsrchnum.htm&r=1&f=G&l=50&s1=3578834.PN.&OS=PN/3578834&RS=PN/3578834 (visited on 10/30/2018).

[57] *Caesium-Verbindungen*, 2017, URL: https://roempp.thieme.de/roempp4.0/do/data/RD-03-00067 (visited on 08/22/2018).

[58] P. della Porta, C. Emili, and S. J. Hellier, *Alkali Metal Generation and Gas Evolution from Alkali Metal Dispensers*, in: IEEE Conference on Tube Techniques, New York.

[59] Alfa Aesar, *Safety Data Sheet, Sodium Chromate*, 2016, URL: https://www.alfa.com/de/content/msds/english/A10547.pdf (visited on 08/28/2017).

[60] Alfa Aesar, *Safety Data Sheet, Potassium Chromate*, 2015, URL: https://www.alfa.com/de/content/msds/english/12610.pdf (visited on 08/28/2017).

[61] Alfa Aesar, *Safety Data Sheet, Cesium Chromate*, 2017, URL: https://www.alfa.com/de/content/msds/english/B23619.pdf (visited on 08/28/2017).

[62] H. Kirschner, *Spectral Quantum Efficiency Measurements on Cs-K-Sb Photocathodes for the Energy-Recovery Linac Test Facility bERLinPro*, Master's Thesis, Humboldt-Universität zu Berlin, 2017, DOI: 10.18452/14294.

[63] D. Briggs and M. P. Seah, eds., *Practical Surface Analysis*, 2nd, vol. 1, Aarau: Salle+Sauerländer, 1990, p. 555, ISBN: 0-471-92081-9, DOI: 10.1016/0165-9936(92)87016-D.

[64] J. F. Watts and J. Wolstenholme, *An introduction to surface analysis by XPS and AES*, Wiley, 2003, ISBN: 0470847123, DOI: 10.1002/0470867930.

[65] J. F. Moulder et al., *Handbook of X-ray Photoelectron Spectroscopy*, Perkin-Elmer Corporation, 1992, ISBN: 9780962702624.

[66] National Institute of Standards and Technology, Gaithersburg MD, *NIST X-ray Photoelectron Spectroscopy Database, NIST Standard Reference Database Number 20*, 2000, DOI: 10.18434/T4T88K, URL: https://srdata.nist.gov/xps (visited on 04/07/2018).

[67] S. Hüfner, *Photoelectron Spectroscopy - principles and applications*, Berlin: Springer-Verlag, 1995, ISBN: 3-540-19108-9.

[68] S. Lagotzky et al., *Prevention of electron field emission from molybdenum substrates for photocathodes by the native oxide layer*, in: The European Physical Journal Applied Physics 70 (2015), p. 21301, DOI: 10.1051/epjap/2015150167.

[69] F. Werfel and E. Minni, *Photoemission study of the electronic structure of Mo and Mo oxides*, in: Journal of Physics C: Solid State Physics 16 (1983), pp. 6091–6100, DOI: 10.1088/0022-3719/16/31/022.

[70] J. Scofield, *Hartree-Slater subshell photoionization cross-sections at 1254 and 1487 eV*, in: Journal of Electron Spectroscopy and Related Phenomena 8 (1976), pp. 129–137, DOI: 10.1016/0368-2048(76)80015-1.

[71] W. Werner, W. Smekal, and C. J. Powell, *NIST Database for the Simulation of Electron Spectra for Surface Analysis (SESSA), Version 1.2*, Gaithersburg, Maryland: National Institute of Standards and Technology, 2010.

[72] S. Tanuma, C. J. Powell, and D. R. Penn, *Calculations of electron inelastic mean free paths. V. Data for 14 organic compounds over the 50-2000 eV range*, in: Surface and Interface Analysis 21 (1994), pp. 165–176, DOI: 10.1002/sia.740210302.

[73] M. Schmeißer, *Python scripts for XPS analysis*, 2018, URL: https://github.com/martinschmeisser/XPSdata (visited on 10/30/2018).

[74] CINF, Technical University of Denmark, *PyExpLabSys*, URL: https://github.com/CINF/PyExpLabSys (visited on 05/12/2018).

[75] H. Lee et al., *Review and demonstration of ultra-low-emittance photocathode measurements*, in: Review of Scientific Instruments 86 (2015), p. 073309, DOI: 10.1063/1.4927381.

[76] T. Vecchione et al., *A low emittance and high efficiency visible light photocathode for high brightness accelerator-based X-ray light sources*, in: Applied Physics Letters 99 (2011), p. 034103, DOI: 10.1063/1.3612916.

[77] M. A. H. Schmeißer et al., *In-situ characterization of K2CsSb Photocathodes*, in: Proceedings of IPAC 2014, Dresden, Germany, pp. 627–629, DOI: 10.18429/JACoW-IPAC2014-MOPRI019.

[78] L. B. Jones et al., *The comissioning of TESS: an experimental facility for measuring the electron energy distribution from photocathodes*, in: Proceedings of FEL2013, New York, NY, USA, URL: http://accelconf.web.cern.ch/Accelconf/FEL2013/papers/tupso33.pdf.

[79] L. J. Devlin et al., *Measurement of the longitudinal energy distribution of electrons in low energy beams using electrostatic elements*, in: Review of Scientific Instruments 89 (2018), p. 83305, DOI: 10.1063/1.5036925.

[80] L. B. Jones et al., *Transverse Energy Distribution Measurements for Polycrystalline and (100) Copper Photocathodes with Known Levels of Surface Roughness; Transverse Energy Distribution Measurements for Polycrystalline and (100) Copper Photocathodes with Known Levels of Surface Roughness*, in: Proceedings of IPAC 2018, Vancouver, BC, Canada, DOI: 10.18429/JACoW-IPAC2018-THPMK062.

[81] H. Lee, *For brighter electron sources : a cryogenically cooled photocathode and DC photogun*, PhD thesis, Cornell University, 2017, DOI: 10.7298/X41R6NP8.

[82] M. G. Minty and F. Zimmermann, *Measurement and Control of Charged Particle Beams*, Berlin Heidelberg New York: Springer-Verlag, 2003, ISBN: 978-3-662-08581-3, DOI: 10.1007/978-3-662-08581-3.

[83] C. Gulliford and I. Bazarov, *New method for generating linear transfer matrices through combined rf and solenoid fields*, in: Physical Review Special Topics - Accelerators and Beams 15 (2012), p. 024002, DOI: 10.1103/PhysRevSTAB.15.024002.

[84] I. V. Bazarov et al., *Thermal emittance and response time measurements of negative electron affinity photocathodes*, in: Journal of Applied Physics 103 (2008), p. 054901, DOI: 10.1063/1.2838209.

[85] K. Halbach and R. F. Holsinger, *SUPERFISH - A Computer Program for Evaluation of RF Cavities with Cylindrical Symmetry*, in: Particle Accelerators 7 (1976), pp. 213–222.

[86] Dr. S.B. van der Geer and Dr. M.J. de Loos, *General Particle Tracer*, URL: http://www.pulsar.nl/gpt/ (visited on 05/12/2018).

[87] *EPICS - Experimental Physics and Industrial Control System*, URL: http://www.aps.anl.gov/epics/index.php (visited on 11/14/2017).

[88] *EPICS Archiver Appliance*, URL: https://slacmshankar.github.io/epicsarchiver%7B%5C_%7Ddocs/index.html (visited on 11/14/2017).

[89] *Control System Studio*, URL: https://github.com/ControlSystemStudio/cs-studio (visited on 11/14/2017).

[90] W. H. McCarroll, *Chemical and structural characteristics of the potassium-cesium-antimony photocathode*, in: Journal of Physics and Chemistry of Solids 26 (1965), pp. 191–195, DOI: 10.1016/0022-3697(65)90087-9.

[91] S. G. Schubert et al., *Influence of Growth Method on K3Sb Phtocathode Structure and Performance*, in: Proceedings of IPAC 2014, DOI: 10.18429/JACoW-IPAC2014-MOPRI018.

[92] M. Ruiz-Osés et al., *Direct observation of bi-alkali antimonide photocathodes growth via in operando x-ray diffraction studies*, in: APL Materials 2 (2014), p. 121101, DOI: 10.1063/1.4902544.

[93] S. Schubert et al., *Bi-alkali antimonide photocathode growth: An X-ray diffraction study*, in: Journal of Applied Physics 120 (2016), p. 035303, DOI: 10.1063/1.4959218.

[94] Z. Ding et al., *Improving the Smoothness of Multi-Alkali Antimonide Photocathodes: An In-Situ X-Ray Reflectivity Study*, in: Proceedings of ERL 2015, pp. 27–29, URL: http://accelconf.web.cern.ch/accelconf/erl2015/papers/tuiclh1030.pdf.

[95] J. Xie et al., *Synchrotron x-ray study of a low roughness and high efficiency K2CsSb photocathode during film growth*, in: Journal of Physics D: Applied Physics 50 (2017), p. 205303, DOI: 10.1088/1361-6463/aa6882.

[96] A. di Bona et al., *Development, operation and analysis of bialkali antimonide photocathodes for high-brightness photo-injectors*, in: Nuclear Instruments and Methods in Physics Research, Section A 385 (1997), pp. 385–390, DOI: 10.1016/S0168-9002(96)00809-1.

[97] I. Martini, *Characterization of Cs-Sb cathodes for high charge RF photoinjectors*, PhD thesis, Politecnico di Milano, 2015, URL: http://cds.cern.ch/record/2228514.

[98] L. Cultrera, H. Lee, and I. Bazarov, *Alkali antimonides photocathodes growth using pure metals evaporation from effusion cells*, in: Journal of Vacuum Science & Technology B 34 (2016), p. 011202, DOI: 10.1116/1.4936845.

[99] J. S. Fraser et al., *High-Brightness Photoemitter Injector for Electron Accelerators*, in: IEEE Transactions on Nuclear Science 32 (1985), pp. 1791–1793, DOI: 10.1109/TNS.1985.4333725.

[100] J. Kühn et al., *A Cu Photocathode for the Superconducting RF Photoinjector of BERLinPro*, in: Proceedings of IPAC 2018, pp. 1247–1250, DOI: 10.18429/JACOW-IPAC2018-TUPMF002.

[101] S. Schubert et al., *Bi-alkali antimonide photocathodes for high brightness accelerators*, in: APL Materials 1 (2013), p. 032119, DOI: 10.1063/1.4821625.

[102] L. Soriano and L. Galan, *Interaction of cesium-potassium antimonide photocathode materials with oxygen: An x-ray photoelectron spectroscopy study*, in: Japanese Journal of Applied Physics 32 (1993), pp. 4737–4744, DOI: 10.1143/JJAP.32.4680.

[103] S. Schubert et al., *CsK2Sb Growth Studies, Towards High Quantum Efficiencies and Smooth Surfaces*, in: Proceedings of IPAC 2015, pp. 2566–2568, DOI: 10.18429/JACoW-IPAC2015-WEPWA032.

[104] M. A. Mamun et al., *Correlation of CsK2Sb photocathode lifetime with antimony thickness*, in: APL Materials 3 (2015), p. 066103, DOI: 10.1063/1.4922319.

[105] Z. Ding et al., *In-situ synchrotron x-ray characterization of K2CsSb photocathode grown by ternary co-evaporation*, in: Journal of Applied Physics 121 (2017), p. 055305, DOI: 10.1063/1.4975113.

[106] M. Newville et al., *LMFIT: Non-Linear Least-Square Minimization and Curve-Fitting for Python*, DOI: 10.5281/zenodo.11813, URL: https://lmfit.github.io/lmfit-py/ (visited on 05/09/2018).

[107] L. Cultrera et al., *Cold electron beams from cryocooled, alkali antimonide photocathodes*, in: Physical Review Special Topics - Accelerators and Beams 18 (2015), p. 113401, DOI: 10.1103/PhysRevSTAB.18.113401.

[108] E. Wang and H.M. Xie, *Characterization of Multi-Alkali antimonide Cathodes at Cryogenic Temperature and their Performance in SRF Gun*, in: Proceedings of ERL 2015, URL: http://accelconf.web.cern.ch/AccelConf/ERL2015/talks/tuiclh1027%7B%5C_%7Dtalk.pdf.

[109] Taro Konomi, *Progress of SRF GUN development at KEK*, in: Beschleunigerphysikseminar, 25.08.2016, URL: http://helmholtz-berlin.de/media/media/grossgeraete/beschleunigerphysik/intern/vortraege-seminar-beschleunigerphysik/2016/kek-srfgun-development-konomi.pdf.

[110] C. Cocchi et al., *First-principles many-body study of the electronic and optical properties of CsK2Sb, a semiconducting material for ultra-bright electron sources*, in: Journal of Physics: Condensed Matter 31 (2018), p. 014002, DOI: 10.1088/1361-648X/aaedee.

[111] C. Ghosh and B. P. Varma, *Preparation and study of properties of a few alkali antimonide photocathodes*, in: Journal of Applied Physics 49 (1978), pp. 4549–4553, DOI: 10.1063/1.325465.

[112] G. Wang et al., *Degradation of Alkali-Based Photocathodes from Exposure to Residual Gases: A First-Principles Study*, in: The Journal of Physical Chemistry C 121 (2017), pp. 8399–8408, DOI: 10.1021/acs.jpcc.6b12796.

[113] J. Kwan Bae et al., *Brightness of nonequilibrium photoemission in metallic photocathodes near threshold*, in: (2018), pp. 1–11, arXiv: 1808.06902v1.

[114] A. Neumann et al., *The bERLinPro SRF Photoinjector System - from first RF Commissioning to first Beam*, in: Proceedings of IPAC 2018, pp. 1660–1663, DOI: 10.18429/JACoW-IPAC2018-TUPML053.

[115] T. Kamps et al., *Setup and Status of an SRF Photoinjector for Energy - Recovery Linac Application* , in: Proceedings of IPAC 2017, pp. 865–868, DOI: 10.18429/JACoW-IPAC2017-MOPVA010.

[116] A. Neumann et al., *First Commissioning of an SRF Photo-Injector Module for bERLinPro*, in: Proceedings of IPAC 2017, pp. 971–974, DOI: 10.18429/JACoW-IPAC2017-MOPVA049.

[117] K. Zapfe and J. Wojtkiewicz, *Particle Free Pump Down and Venting of UHV Vacuum Systems*, in: Proceedings of SRF 2009, p. 681, URL: https://accelconf.web.cern.ch/accelconf/srf2007/PAPERS/WEP74.pdf.

[118] M. D. Lay, *Parameterization of the angular response of 254 cm photo-multiplier tubes*, in: Applied Optics 36 (1997), p. 232, DOI: 10.1364/AO.36.000232.

[119] S. Hallensleben, S. Harmer, and P. Townsend, *Optical constants for the S20 photocathode, and their application to increasing photomultiplier quantum efficiency*, in: Optics Communications 180 (2000), pp. 89–102, DOI: 10.1016/S0030-4018(00)00694-5.

[120] D. Motta and S. Schönert, *Optical properties of bialkali photocathodes*, in: Nuclear Instruments and Methods in Physics Research, Section A 539 (2005), pp. 217–235, DOI: 10.1016/j.nima.2004.10.009.

[121] Z. Ding et al., *Temperature-dependent quantum efficiency degradation of K-Cs-Sb bialkali antimonide photocathodes grown by a triple-element codeposition method*, in: Physical Review Accelerators and Beams 20 (2017), p. 113401, DOI: 10.1103/PhysRevAccelBeams.20.113401.

[122] M. G. Helander et al., *Pitfalls in measuring work function using photoelectron spectroscopy*, in: Applied Surface Science 256 (2010), pp. 2602–2605, DOI: 10.1016/j.apsusc.2009.11.002.

[123] J. C. Rivière and S. Myhra, *Handbook of surface and interface analysis : methods for problem-solving*, CRC Press, 2009, p. 651, ISBN: 9781420007800.

[124] ThermoFischer Application Note 31068, *Energy Resolution in X-ray Photoelectron Spectroscopy (XPS)*, URL: https://assets.thermofisher.com/TFS-Assets/CAD/Application-Notes/D16105%7B~%7D.pdf (visited on 11/27/2017).

[125] R. H. Fowler, *The Analysis of Photoelectric Sensitivity Curves for Clean Metals at Various Temperatures*, in: Physical Review 38 (1931), pp. 45–56, DOI: 10.1103/PhysRev.38.45.

[126] L. A. DuBridge, *Theory of the Energy Distribution of Photoelectrons*, in: Physical Review 43 (1933), pp. 727–741, DOI: 10.1103/PhysRev.43.727.

[127] G. Hechenblaikner et al., *Energy distribution and quantum yield for photoemission from air-contaminated gold surfaces under ultraviolet illumination close to the threshold*, in: Journal of Applied Physics 111 (2012), p. 124914, DOI: 10.1063/1.4730638.

Selbstständigkeitserklärung

Ich erkläre, dass ich die Dissertation selbständig und nur unter Verwendung der von mir gemäß § 7 Abs. 3 der Promotionsordnung der Mathematisch-Naturwissenschaftlichen Fakultät, veröffentlicht im Amtlichen Mitteilungsblatt der Humboldt-Universität zu Berlin Nr. 42/2018 am 11.07.2018 angegebenen Hilfsmittel angefertigt habe.

Martin Schmeißer

Berlin, 5. September 2019

Acknowledgements

It is true for the past four years more than ever before that "if I have seen further it is by standing on the shoulders of giants." At this point I wish to express my deep gratitude to those who have made this project not only possible but a valuable and enjoyable apprenticeship.

Primarily these are my supervisors Prof. Dr. Thorsten Kamps and Prof. Dr. Andreas Jankowiak. I appreciate your full support and trust that allowed me to follow this path with great freedom and own responsibility.

I also want to thank my appraisers Prof. Dr. Simone Raoux and Univ.-Prof. Dr. Kurt Aulenbacher for valuable discussions.

At the same time, none of this would have been possible without Julius Kühn and Sonal Mistry, whom I had the honor and pleasure to work with: daily, in the lab, openly and honest in discussions, and seemingly infinite in their support and willingness to share their experience.

Throughout this work I was allowed to rely on a great academic network, and I would like to extend my thanks to the many colleagues who have all been very welcoming and supportive. Especially during the beamtimes with John Smedley's group at Brookhaven National Lab I was able to learn from John, who seems to know the properties of any material off the top of his head, and Menjia Gaowei, who seems to have infinite energy and can accurately follow the experiment plot at any time of the night, as well as John Sinsheimer and John Walsh. Zihao Ding from BNL followed our invitation to use DAAD's RISE programme to work in our lab for three months - it has been a great pleasure to host you and work together that summer. By support of HZB's programme "PhD reasearch abroad" I was able to travel to Cornell University for three months and work with Luca Cultrera and Prof. Ivan Bazarov's group. I am indebted to both of them for their hospitality, trust and great support during that time. There, I had the pleasure to learn from Hyeri Lee, Alice Galdi, Colwyn Gulliford, and Adam Bartnik.

I would also like to thank the members of the GunLab and bERLinPro teams who were very helpful and supportive, especially Guido Klemz, Axel Neumann, Georgios Kourkafas, Susanne Schubert, and Nina Ohm-Krafft. The development of the transfer systems, suitcase, and the particle free pump cart was supported by Markus Bürger, Kerstin Martin, André Frahm, Michael Schuster, Henry Plötz, Jörg Borninkhof, Andreas Durinke and Jörg Schleuer. Further, I am grateful to Jochen Teichert, Rong

Xiang, and Petr Murcek at HZDR and Sven Lederer at Desy as well as Monika Dehn and Viktor Bechthold at Mainz University for many helpful discussions.

The development of the metallic substrates was supported by the machine shop teams at Adlershof and Wannsee. I would like to thank Frank Siewert, Grzegorz Gwalt and Jana Buchheim for valuable discussions and roughness measurements as well as Carola Klimm for help with the surface polishing. During the setup of the process control software I received a lot of support from Joachim Rahn, Thomas Birke, Bernard Kuner, and Michael Edling at HZB as well as Peter Linardakis at Australian National University.

My fellow students Julia, Eva, Jens, Sebastian have made this job priceless and provided the necessary strong team spirit and encouragement. Especially, Julia, thank you for very quick, accurate, and honest proof reading. I also want to thank our students Hans for help with the commissioning of the QE setup and Nawar for his work on the cathode interface.

Finally, it is the support of my family and friends that have helped me through this endeavor. I want to thank A. and my parents for their continued encouragement, guidance and support.

And it is your love, A. and M., that I live for. I might by far not be a giant in the sense of the first paragraph, but at least I can put you, M., on my shoulders and I know you enjoy nothing more than to see farther.